Doctoral Dissertation
博士論文

Observational signatures from tidal disruption events of white dwarfs

(白色矮星の潮汐破壊現象からの観測兆候)

A Dissertation Submitted for the Degree of Doctor of Philosophy
December 2020
令和2年12月 博士（理学）申請

Department of Physics, Graduate School of Science,
The University of Tokyo
東京大学大学院理学系研究科物理学専攻

Kojiro Kawana
川名　好史朗

Abstract

Recent advances in optical surveys have yielded a large sample of astronomical transients, including classically known novae and supernovae (SNe) and also newly discovered classes of transients. Among them, tidal disruption events (TDEs) have a unique feature that they can probe massive black holes (MBHs). A TDE is an event where a star approaching close to a BH is disrupted by tides of the BH. The disrupted star leaves debris bound to the BH emitting multi-wavelength and multi-messenger signals, which are observed as a transient. The observational signatures of TDEs bring us insights into physical processes around the BH, such as dynamics in the general relativistic gravity, accretion physics, and environmental information around BHs. Event rates of TDEs also inform us of populations of BHs.

A large number of BHs have been detected, but still there are big mysteries. The most mysterious BHs are intermediate mass BHs (IMBHs) because they are a missing link: there is almost no certain evidence of IMBHs, while there are many detections of stellar mass BHs and supermassive BHs (SMBHs). Searches for IMBHs are not only important to reveal mysteries of IMBHs themselves, but also to understand origin(s) of SMBHs. Several scenarios to form SMBHs have been proposed, but it is still unclear which scenario(s) are real in the Universe. A distinguishable point is a mass distribution of IMBHs because the different scenarios would result in different mass distributions. Thus, finding IMBHs would play a crucial role to understand nature of massive BHs.

In this thesis, we study TDEs where a white dwarf (WD) is disrupted by an IMBH to probe IMBHs. This is motivated by the nature of WD TDEs that an SMBH cannot tidally disrupt a WD because the SMBH swallows the WD before the disruption, and thus there is no observable except for gravitational waves. Detection of WD TDEs implies that of the disrupting IMBH, and thus WD TDEs are good probes of IMBHs. WD TDEs have another interesting feature: a WD possibly ignites thermonuclear explosions by tidal compression if the WD-BH encounter is close enough. Once the thermonuclear explosions occur, radioactive nuclei such as ^{56}Ni are synthesized. Then debris of the WD unbound to the IMBH possibly cause emission powered by decays of the radioactive nuclei. It is naively expected that the emission could be similar to that of SNe Ia because of the similarity in the thermonuclear explosions of a WD.

With these motivations, efforts to find WD TDEs have been dedicated. Although a few possible candidates of WD TDEs have been reported, they are not confirmed as WD TDEs and other origins are also proposed. Event rates of WD TDEs are also uncertain because of the unknown nature of IMBHs, but it is still expected that the current or upcoming optical surveys possibly detect WD TDEs. To search for WD TDEs among transients found by those surveys, it is needed to model the observational signatures from WD TDEs in more detail. Especially, a variety of emission from thermonuclear explosions in WD TDEs are unknown, and thus it is difficult to point out distinguishable features of WD TDEs with other transients.

This thesis aims to reveal the variety and characteristics of observational signatures from thermonuclear explosions in WD TDEs, and to constrain properties of IMBHs. To this end, we perform a suite of three different numerical simulations considering 5 parameter sets of WD TDEs. We take the WD mass as the main parameter to be varied over 0.2, 0.4, 0.6, 1.0, and 1.2 solar mass ($\mathrm{M}_\odot$). First, we perform three-dimensional hydrodynamic simulations coupled with simplified nuclear reaction networks, and follow dynamical evolution of the tidal disruption of a WD by a BH and thermonuclear explosions in the disruption phase. Second, we perform detailed nucleosynthesis simulations in a post-process manner, and derive the synthesized nuclear compositions of the unbound ejecta. Finally, we perform radiative transfer simulations, and follow generation of photons by the radioactive decays, interactions of the photons with the unbound ejecta, and escapes of the photons from the ejecta, from which we derive the synthetic observational signatures.

We derive multi-band light curves and spectral evolutions of the 5 models as templates of the thermonuclear emission from the WD TDEs. On photometric properties, the 0.2 $\mathrm{M}_\odot$ model exceptionally shows relatively faint ($L_{\mathrm{peak}} \sim 10^{42}\,\mathrm{erg\,s^{-1}}$) and rapidly evolving light curves (decay timescale $\simeq 5-10$ d), because the ejecta mass and ^{56}Ni mass are low ($0.12\,\mathrm{M}_\odot$ and $0,03\,\mathrm{M}_\odot$, respectively). The 0.4, 0.6, 1.0, and 1.2 $\mathrm{M}_\odot$ models are similar to some classes of thermonuclear transients, or SNe Ia, in photometric properties such as the bolometric peak luminosity, decay timescale, B-band peak magnitudes, and B-band decay timescale. However, they commonly show higher temperature than the observed thermonuclear transients around their B-band peaks. The difference can be used as a signature to distinguish the thermonuclear emission from WD TDEs from the other thermonuclear transients. All the models show a large variety in their light curves dependent on viewing angles because the ejecta is very aspherical due to the tidal disruption.

On spectroscopic properties, our WD TDE models are indeed similar to observed thermonuclear transients in some senses, such as absence of hydrogen lines and appearance of lines of iron group elements and calcium. However, there is a difference in lines of intermediate mass elements (IMEs): the observed thermonuclear transients show strong IME lines, while our models show (very) weak IME lines because of the nucleosynthesis yielding low mass IMEs. This difference might not be conclusive because the synthesized IME masses are sensitive to numerical resolutions, and simulations with higher resolutions might result in larger IME masses and thus in stronger IME lines. Another more robust difference is Doppler shifts of spectra shown in our models. The Doppler shifts are caused by the bulk motion of unbound ejecta escaping from the BH with velocities of $\gtrsim 10^4\,\mathrm{km\,s^{-1}}$. Although the Doppler shifts depend on viewing angles, they can be a crucial signature to distinguish WD TDEs from other transients.

We search for observational counterparts of WD TDEs that show similar observational signatures to our models. For the 0.4, 0.6, 1.0, and 1.2 $\mathrm{M}_\odot$ models, we cannot find any good match in multi-band light curves between our models and observed transients. For the 0.2 $\mathrm{M}_\odot$ model, we find two observational candidates in relatively faint and rapid transients, which show similar multi-band light curves to the model. Because their spectra are not observed, we cannot confirm their origin as a WD TDE by comparing the spectra. However, one of the transients has a distant 10.2 kpc offset from the center of its host galaxy. This may support interpreting its origin as a WD TDE, of which a star cluster containing an IMBH and WD is the plausible environment.

The photometric properties of our models cover a wide phase space. There could be a more variety of them because the intrinsic parameter sets of WD TDEs (M_{WD}, M_{BH}, β) can vary over a wider parameter space than the 5 parameter sets. We discuss the possible range of the variety of observational signatures of WD TDEs by applying the so-called Arnett rule. First, we check the validity of the application of the Arnett rule by comparing the peak time and peak luminosity predicted by the Arnett rule and by our numerical simulations. They show reasonable matches, and thus we next apply the Arnett rule to results of hydrodynamic simulations of WD TDEs considering 180 parameter sets. The results show that there could be more slowly evolving and much fainter WD TDEs ($L_{\mathrm{peak}} \gtrsim 10^{38}\,\mathrm{erg\,s^{-1}}$) than our 5 models ($L_{\mathrm{peak}} \sim 10^{42}$–$10^{43}\,\mathrm{erg\,s^{-1}}$), which arise from WD TDEs with weaker thermonuclear explosions. Such faint transients should also be searched for as WD TDEs.

Emission from WD TDEs is not only caused by thermonuclear explosions, but also by debris falling back on to the BH. If the luminosity of the fallback emission follows the mass fallback rate of the debris, the thermonuclear emission would be fainter than it. However, it is naively expected that the fallback luminosity is limited by the Eddington luminosity unless relativistic jets are viewed on-axis. Additionally, the accretion disk formed by the fallback debris would be bright mainly in X-rays. Thus, we expect that the thermonuclear optical emission is not significantly affected by the fallback emission in most cases.

If the two observational candidates are really WD TDEs, they inform us of the event rate of WD TDEs and the IMBH number density. The sum of their volumetric event rates are estimated as $\simeq 600\,\mathrm{Gpc^{-3}\,yr^{-1}}$. Considering a ratio of WD TDEs with thermonuclear explosions to all the WD TDEs, we obtain the total WD TDE rate as $\sim 3\times10^{3}\,\mathrm{Gpc^{-3}\,yr^{-1}}$. Taking a WD TDE rate per an IMBH as that in centers of dwarf galaxies, we estimate the number density of IMBHs from the total WD TDE rate as $n_{\mathrm{IMBH}} \sim 3\,\mathrm{Mpc^{-3}}$. Although the confidence is not very high, this estimate is valuable because there has been almost no constraint on the number density of IMBHs.

The observational signatures of WD TDEs derived in this thesis are useful to search for WD TDEs with current and upcoming optical surveys. As we find two observed candidates of WD TDEs in the current transient sample, we would be able to find more WD TDE candidates with a much larger transient sample given by those surveys. There might be also WD TDEs detected with high certainties, showing good matches both in photometric and spectroscopic properties to our models. Such findings of WD TDEs would contribute to explore origins of observed transients, to study extreme physical processes around BHs, and to reveal unknown nature of massive BHs.

Contents

Chapter 1

Introduction

1.1 Diverse Transients

In a night sky, we see bright stars and galaxies. Most of them stably shine, while some show time-varying brightness, such as variable stars and quasars. There are a small fraction of astronomical objects which change their brightness dramatically and are visible only in short timescales up to a few 10 years. They are called transients. Classically, there were only two established classes of transients: classical novae and supernovae (SNe) (e.g. Baade & Zwicky, 1934). Classical novae arise from thermonuclear burning on a white dwarf (WD) driven by accretion on to the WD. SNe are much brighter than classical novae: peak luminosity of SNe is $\sim 10^4$ times larger than those of classical novae (see Figure 1.1). SNe are categorized into two types with their origins. One is core-collapse SNe (CC SNe) resulting from a death of a massive star, where a collapse of its iron core triggers a formation of a neutron star and a succeeding explosion of its outer region. The other category is thermonuclear SNe resulting from thermonuclear explosions of WDs. The thermonuclear SNe is also called type Ia SNe (SNe Ia). The name shows their spectroscopic properties: lack of hydrogen lines and appearance of silicon lines. The classical novae and SNe have been studied for a long time and consensuses of their origins are established to some extent, although there are still mysteries (see reviews on classical novae: Chomiuk et al. (2020), on CC SNe: Burrows & Vartanyan (2020), and on SNe Ia: Maoz et al. (2014)).

A big breakthrough in this field was yielded with optical surveys with CCD cameras, which have wider fields of view, deeper limiting magnitudes, and high time cadences. They have been founding a larger number of classical novae and SNe, and rare classes of transients missed by classical observations. Some of them were theoretically predicted before their discovery, such as kilonovae/macronovae from mergers of binary neutron stars (e.g. Abbott et al., 2017), and .Ia explosions (Bildsten et al., 2007; Shen et al., 2010). There are also surprising discoveries, such as diverse CC SNe with a variety of circumstellar medium (Fraser, 2020), and tidal disruption events luminous in optical (van Velzen et al., 2020b, see also Section 2.1).

The increasing discoveries of known and new transients have motivated further observational searches for transients, and also theoretical studies to model known transients in more detail and to predict unknown transients. The time-domain astronomy plays important roles in various fields, to study various explosive phenomena in the Universe, environmental information of progenitor stars, the cosmic expansion, and physical processes in extreme conditions. Now the Zwicky Transient Facility (ZTF) is the most powerful tool to observe transients (Graham et al., 2019). In the near future, the Large Synoptic Survey Telescope (LSST) on the Vera C. Rubin Observatory will join and will be the most powerful telescope to find transients (LSST Science Collaboration et al., 2009; Ivezić et al., 2019). It is needed to develop theoretical models of transients along with increasing observations of transients.

1.2 Massive Black Holes in the Universe

Black holes (BHs) are compact objects whose extreme general relativistic gravity disable light to escape from the gravitational potential. Astronomical BHs in the Universe are categorized into three types by their masses: stellar mass BHs with their masses smaller than $\simeq 100\,\mathrm{M}_\odot$, intermediate mass BHs (IMBHs) with their masses in the range of $100\,\mathrm{M}_\odot \lesssim M_\mathrm{BH} \lesssim 10^6\,\mathrm{M}_\odot$, and supermassive BHs (SMBHs) with their masses larger than $\simeq 10^6\,\mathrm{M}_\odot$, where $\mathrm{M}_\odot$ is the solar mass and M_BH is the BH mass. Most of the stellar mass BHs are formed in deaths of massive stars that fail to explode as an SN, while other formation scenarios such as mergers of neutron stars are also possible (Abbott et al., 2020c). There have been a few tens of discoveries of stellar mass BHs in high mass X-ray binaries (Özel et al., 2010; Farr et al., 2011), and in BH binaries discovered with recent observations of gravitational waves (GWs) by Advanced LIGO and Advanced Virgo (Abbott et al., 2020a). Origin(s) of massive BHs (MBHs), IMBHs and SMBHs, are much poorly known than those of stellar mass BHs. Although many SMBHs have been found in centers of galaxies (e.g. Kormendy & Richstone, 1995), there is not a consensus on their origin(s). We have much fewer observations on IMBHs. There has been no certain evidence of IMBHs, except for the recent discovery of a $142\,\mathrm{M}_\odot$ BH as a remnant of a merger of stellar mass BHs (Abbott et al., 2020b), while there are candidates of IMBHs in ultra-luminous X-ray sources and in centers of globular clusters and of dwarf galaxies (Mezcua, 2017; Greene et al., 2020).

Searches for IMBHs are not only important to reveal mysteries of IMBHs, but also to understand the origin(s) of SMBHs. This is because the origin(s) of SMBHs would be tightly related to IMBHs. Possible origins of MBHs are first summarized in the Rees diagram (Rees, 1978, 1984). They can be categorized into 3 scenarios: gravitational runaway in dense star clusters (Bahcall & Ostriker, 1975; Begelman & Rees, 1978; Quinlan & Shapiro, 1990; Lee, 1993), collapse of Population III stars, or first stars (Bond et al., 1984; Madau & Rees, 2001), and direct collapse of gas into a BH (Haehnelt & Rees, 1993; Loeb & Rasio, 1994; Koushiappas et al., 2004). It is still under discussion which scenario(s) are real in the Universe. A distinguishable point is a mass distribution of IMBHs because the different scenarios would result in different mass distributions (see Greene et al., 2020, and references therein). In the future, the mass distribution would

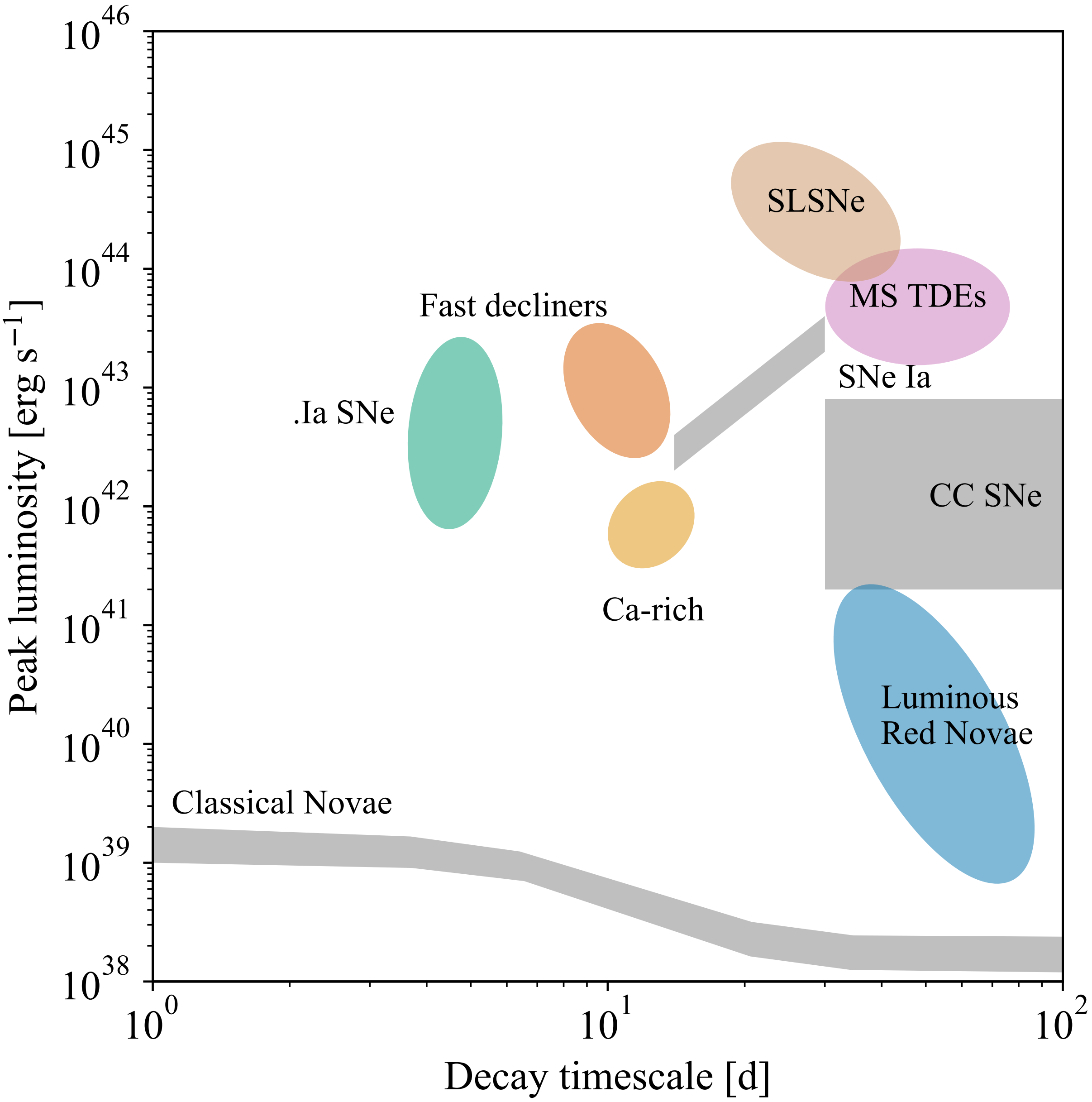

Figure 1.1: Diversities of observed optical transients (see also Section 4.2). The decay timescale is defined as the time in which the bolometric luminosity declines by one magnitude from the peak. The abbreviations are as follows: core-collapse supernovae (CC SNe), type Ia supernovae (SNe Ia), superluminous supernovae (SLSNe), main sequence tidal disruption events (MS TDEs), .Ia supernovae (.Ia SNe), and calcium-rich transients (Ca-rich). The figure is reproduced from Kasliwal (2012); Cenko (2017); García-Berro et al. (2017)

be measured well with GW observations by Laser Interferometer Space Antenna (LISA) (Amaro-Seoane et al., 2017). Independent measurement of it is still important and would bring a good synergy in the multi-messenger astronomy.

1.3 Tidal Disruption Events Probing Massive Black Holes

Tidal disruption events (TDEs) are a class of transients with a unique feature that they can probe properties of MBHs. A TDE is an event where a star approaching close to an MBH is disrupted by the tidal force of the MBH (see Figure 1.2). The disrupted star leaves debris bound to the MBH emitting a bright flare. A few tens of TDEs have been observed in multi-wavelengths ranging from radio to γ-ray, and possibly with a high-energy neutrino. TDEs are unique phenomena in the sense that we can observe MBHs transiently bright otherwise dark and unobservable. By modeling the observational signatures of TDEs, we can study physical processes around the MBH, such as dynamics in the general relativistic gravity, accretion physics, and environmental information around MBHs. We can also study populations of MBHs because event rates of TDEs highly depend on them.

There are a few types of TDEs: we can consider different types for stars disrupted and different BH masses. The TDEs detected plausibly so far are TDEs where a main sequence is disrupted by an SMBH. We can also consider another type of TDEs where a WD is disrupted by an IMBH. This type of TDEs, WD TDEs, have two unique characteristics. One feature is that an SMBH cannot tidally disrupt a WD because the SMBH swallows the WD before the disruption, and thus there is no observable except for GWs. In this sense, WD TDEs are good probes of IMBHs. The second feature is that a WD possibly ignites thermonuclear explosions by tidal compression if the encounter is close enough. Once the thermonuclear explosions occur, radioactive nuclei such as ^{56}Ni are synthesized. Then debris of the WD unbound to the IMBH possibly cause emission powered by decays of the radioactive nuclei. It is naively expected that the emission could be similar to that of SNe Ia because of the similarity in the thermonuclear explosions of a WD.

With the motivations, there have been studies modeling WD TDEs and predicting observational signatures from them. Luminet & Pichon (1989b) first studied the dynamical evolution of WD TDEs with simplified models, and showed that thermonuclear reactions can be ignited. The WD TDEs are so complex that we need detailed numerical simulations to predict concrete observational signatures, such as multi-band light curves and spectral evolution. MacLeod et al. (2016) predicted such signatures arisen from thermonuclear explosions in a carbon-oxygen (CO) WD TDE by means of hydrodynamic simulations and radiative transfer simulations. It was shown that the emission is indeed reminiscent of SNe Ia. However, MacLeod et al. (2016) only considered one particular case of a CO WD TDE. Therefore, it is still not clear if other WD TDEs share the same properties shown in their model once other parameter sets (e.g. different WD/BH masses) are considered. Further studies are needed to clarify a variety of observational

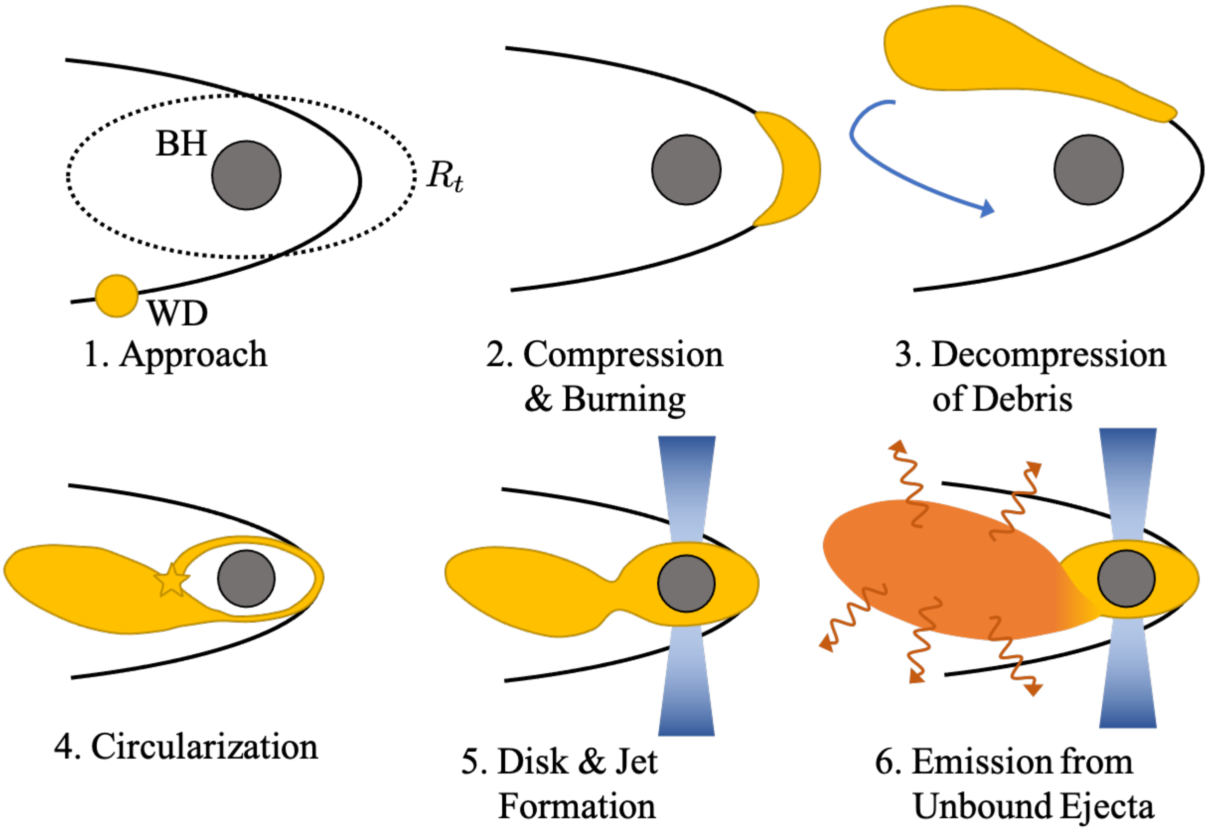

Figure 1.2: Sequence of events in a WD TDE. The WD approaches the BH with the parabolic orbit with its pericenter radius smaller than the tidal radius R_t. The tidal compression perpendicular to the orbital plane can ignite explosive thermonuclear reactions within the WD. Bound debris of the WD falls back on to the BH and forms an accretion disk and possibly relativistic jets later. The unbound debris emits optical radiation powered by decays of radioactive nuclei synthesized in the thermonuclear explosions.

signatures of the emission, and thus to point out distinguishable features of the emission from WD TDEs with other various transients.

1.4 Aims and Structure of the Present Thesis

This thesis aims to reveal the variety and characteristics of observational signatures from thermonuclear explosions in WD TDEs, and to constrain properties of IMBHs by means of detailed numerical simulations. The thesis is organized as follows. In Chapter 2, we review the current knowledge of TDEs from both theoretical and observational aspects. In Chapter 3, we describe our numerical methods and models of WD TDEs. In Chapter 4, we present results of the numerical simulations, and our predictions of the observational signatures from WD TDEs. We also compare our theoretical models with observed transients and search for observed candidates of WD TDEs. In Chapter 5, we discuss implications of our study on a variety of the observational signatures, on emission from debris bound to the BH, and on the properties of IMBHs. In Chapter 6, we give the summary and concluding remarks.

Chapter 2

Review on Tidal Disruption Events

A star passing close to a black hole (BH) can be disrupted when the tidal force on the star exceeds its self-gravity. In the tidal disruption event (TDE), the disrupted star leaves debris bound to the BH, but also disperse unbound materials (e.g. Hills, 1975; Rees, 1988). The debris emits various observational signatures in multi-wavelength and in multi-messengers. The signals have been observed since the 1990's, and thus both observational and theoretical studies of TDEs have been making progress.

In this Chapter, we review the basic properties of TDEs and recent progress. First, we review TDEs where a main sequence (MS) star is disrupted by an SMBH. The MS TDEs are the most common TDEs, and thus there have been many previous studies. Next, we review TDEs where a white dwarf (WD) is disrupted by an IMBH, which is the focus of this thesis.

2.1 Tidal Disruption Events of Main Sequence

2.1.1 Dynamics of TDEs

In this Section, we review dynamical processes in a TDE and its subsequent evolution (see also a recent review Rossi et al., 2020). When a star passes close to a BH, the gravitational force by the BH is expressed as follows in the Newtonian dynamics,

$$\boldsymbol{g}_{\rm BH}(\boldsymbol{r}) = -\frac{GM_{\rm BH}}{r^2}\frac{\boldsymbol{r}}{r}, \tag{2.1}$$

where G is the gravitational constant, $M_{\rm BH}$ is the BH mass, $\boldsymbol{r}$ is the displacement from the BH to the center of the star, and $r = |\boldsymbol{r}|$. Note that Equation (2.1) shows the gravitational force at the center of the star, and it is not uniform on the whole star. Gravitational force on a place of star expressed as $\boldsymbol{r} + \Delta\boldsymbol{r}$, has an additional term to

Equation (2.1) (see Figure 2.1),

$$\boldsymbol{g}_t(\boldsymbol{r},\Delta\boldsymbol{r}) = \boldsymbol{g}_{\rm BH}(\boldsymbol{r}+\Delta\boldsymbol{r}) - \boldsymbol{g}_{\rm BH}(\boldsymbol{r}) \tag{2.2}$$

$$= -GM_{\rm BH}\left(\frac{\boldsymbol{r}+\Delta\boldsymbol{r}}{|\boldsymbol{r}+\Delta\boldsymbol{r}|^3} - \frac{\boldsymbol{r}}{r^3}\right) \tag{2.3}$$

$$\simeq -\frac{GM_{\rm BH}}{r^2}\left(\frac{\Delta\boldsymbol{r}}{r} - \frac{3\boldsymbol{r}\cdot\Delta\boldsymbol{r}}{2r^2}\frac{\boldsymbol{r}}{r}\right) \quad (\Delta r \ll r). \tag{2.4}$$

When $r \gg \Delta r$ is satisfied, this tidal force is expressed as

$$g_t(r,\Delta r) \sim \frac{GM_{\rm BH}\Delta r}{r^3}, \tag{2.5}$$

and is proportional to r^{-3}.

A star in the hydrostatic equilibrium has the balance between the pressure gradient and its self-gravity. When the star passes so close that the tidal force exceeds the self-gravity, the star is disrupted. The TE condition is written as

$$g_t(r,R_\star) \gtrsim \frac{GM_\star}{R_\star^2}, \tag{2.6}$$

where $M_\star$ is the mass of the star, $R_\star$ the radius of the star, and the right-hand side is the self-gravity at the surface of the star. We rewrite the condition with Equation (2.5) as

$$r \lesssim R_t, \tag{2.7}$$

$$R_t := R_\star\left(\frac{M_{\rm BH}}{M_\star}\right)^{1/3}. \tag{2.8}$$

Here we introduce the tidal radius R_t, which is the distance between the BH and star when the disruption occurs. The tidal radius is the same as the Roche radius or Hill radius within an order of magnitude. We can also express Equation (2.7) as

$$\sqrt{\frac{R_t^3}{GM_{\rm BH}}} = \sqrt{\frac{R_\star^3}{GM_\star}} \sim \tau_{{\rm dyn},\star}, \tag{2.9}$$

$$\frac{M_{\rm BH}}{R_t^3} = \frac{M_\star}{R_\star^3} \sim \rho_\star. \tag{2.10}$$

Equation (2.9) shows that the timescale of the disruption is smaller than the dynamical timescale of the star $\tau_{{\rm dyn},\star}$. Equation (2.10) also shows that the tidal radius is the distance r where the density of the star $\rho_\star$ is the same as that of $M_{\rm BH}/r^3$. This means that a less dense object is tidally disrupted by a denser object in general.

The disruption dissipates orbital energy of the debris of the star. Its spread can be estimated as

$$\Delta\epsilon_t \sim \beta^n\frac{GM_{\rm BH}R_\star}{R_t^2} \tag{2.11}$$

$$\simeq 1.9\times10^{17}\,{\rm erg\,g^{-1}}\,\beta^n\left(\frac{R_\star}{\rm R_\odot}\right)^{-1}\left(\frac{M_{\rm BH}}{10^6\,{\rm M_\odot}}\right)^{1/3}\left(\frac{M_\star}{\rm M_\odot}\right)^{2/3}, \tag{2.12}$$

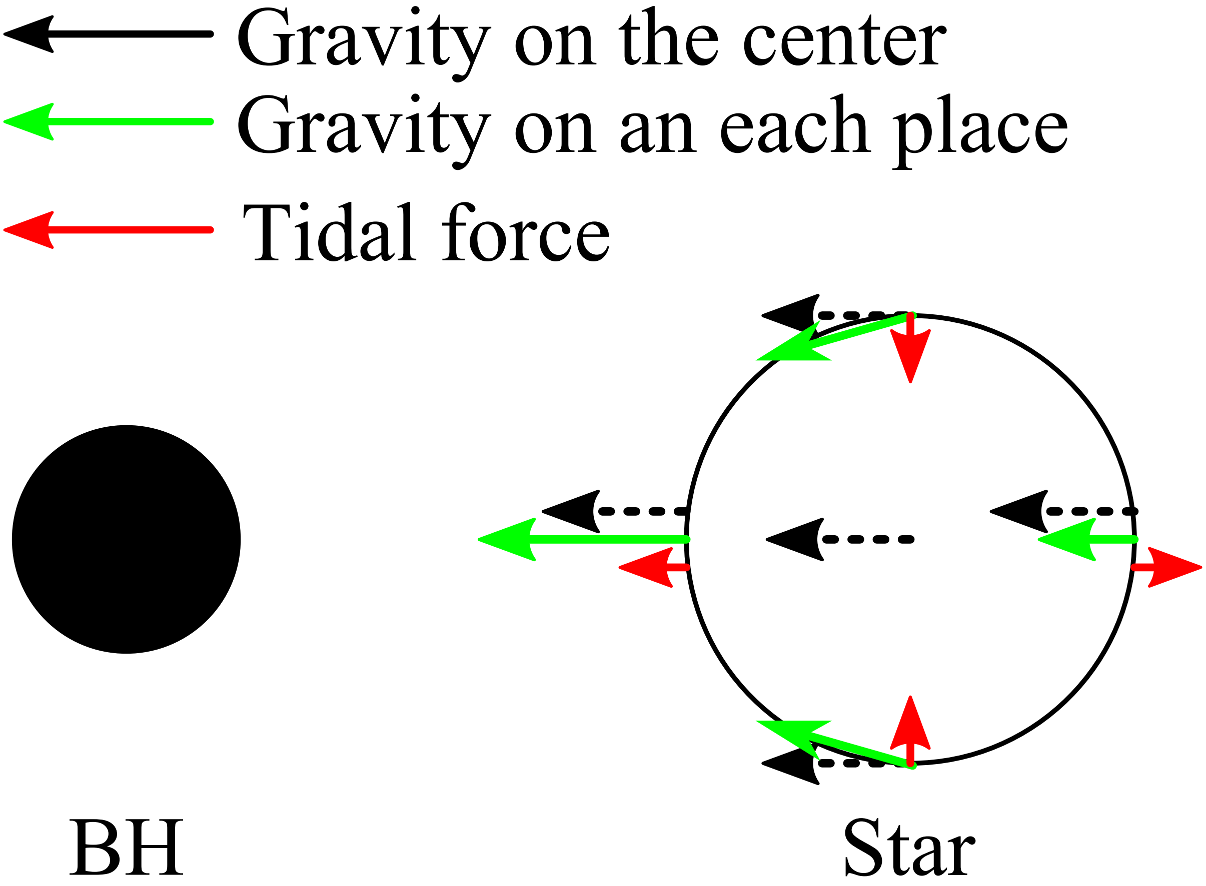

Figure 2.1: A schematic picture showing tidal force. The tidal force is the difference between the gravity on each place of the star and that on the center of the star.

where the penetration parameter β is defined as $\beta := R_t/R_p$. The power law index n is not straightforwardly determined. In early studies (e.g. Rees, 1988) $n = 2$ were applied, where the energy spread is calculated as the difference of the gravitational potential in the star at the pericenter $r = R_p$. However, recent studies (Sari et al., 2010; Guillochon & Ramirez-Ruiz, 2013; Stone et al., 2013) show that the value should be revised as $n \simeq 0$ (see also Steinberg et al., 2019).

In most TDEs, the star approaches the BH on an approximately parabolic orbit (see Section 2.1.3), which results in the much smaller initial specific orbital energy than $\Delta\epsilon_t$. The specific binding energy of the star before the disruption $\epsilon_{\rm self}$ is also much smaller than $\Delta\epsilon_t$:

$$\epsilon_{\rm self} \sim -\frac{GM_\star}{R_\star} \tag{2.13}$$

$$= -6.4\times10^{13}\,{\rm erg\,g^{-1}}\left(\frac{M_\star}{\rm M_\odot}\right)\left(\frac{R_\star}{\rm R_\odot}\right)^{-1}. \tag{2.14}$$

Thus, the orbital energy distribution of the debris of the star is dominantly determined by $\Delta\epsilon_t$. About half of the debris is bound to the BH, and the other is unbound.

The bound debris approaches the BH on eccentric orbits again. The Kepler motion of the debris can be written as

$$\epsilon \sim -\frac{GM_\star}{R_\star} \tag{2.15}$$

$$= -6.4\times10^{13}\,{\rm erg\,g^{-1}}\left(\frac{M_\star}{\rm M_\odot}\right)\left(\frac{R_\star}{\rm R_\odot}\right)^{-1}, \tag{2.16}$$

$$P = 2\pi\sqrt{\frac{a^3}{GM_{\rm BH}}}, \tag{2.17}$$

where ϵ is the orbital energy, P is the orbital period, and a is the semimajor axis. With these equations, we can calculate the mass fallback rate on to the BH as

$$\frac{{\rm d}M}{{\rm d}P} = \left(\frac{{\rm d}M}{{\rm d}\epsilon}\right)\left(\frac{{\rm d}\epsilon}{{\rm d}P}\right) \tag{2.18}$$

$$= \left(\frac{{\rm d}M}{{\rm d}\epsilon}\right)\frac{(2\pi GM_{\rm BH})^{2/3}}{3}P^{-5/3}. \tag{2.19}$$

Here we assume ${\rm d}M/{\rm d}\epsilon = {\rm const.}$, and it is reasonable as a first-order approximation (e.g. Evans & Kochanek, 1989). We also introduce a normalization condition that the half mass of the star is bound to the BH,

$$\frac{M_\star}{2} = \int_{P_{\rm min}}^{\infty}{\rm d}P\frac{{\rm d}M}{{\rm d}P}, \tag{2.20}$$

where $P_{\rm min}$ is the orbital period of the most tightly bound debris. The fallback rate before $P_{\rm min}$ is zero.

Replacing P with t, we rewrite Equation (2.19) as

$$\frac{\mathrm{d}M}{\mathrm{d}t} = \frac{M_\star}{3t_{\rm min}}\left(\frac{t}{t_{\rm min}}\right)^{-5/3} \tag{2.21}$$

$$\simeq 3.0\,\mathrm{M_\odot\,yr^{-1}}\,\beta^{3n/2}\left(\frac{t}{t_{\rm min}}\right)^{-5/3}\left(\frac{M_{\rm BH}}{10^6\,\mathrm{M_\odot}}\right)^{-1/2}\left(\frac{R_\star}{\mathrm{R_\odot}}\right)^{-3/2}\left(\frac{M_\star}{\mathrm{M_\odot}}\right)^{3/2}, \tag{2.22}$$

$$t_{\rm min} = 2\pi G M_{\rm BH}(2\Delta\epsilon_t)^{-3/2} \tag{2.23}$$

$$\simeq 0.11\,\mathrm{yr}\,\beta^{-3n/2}\left(\frac{M_{\rm BH}}{10^6\,\mathrm{M_\odot}}\right)^{1/2}\left(\frac{R_\star}{\mathrm{R_\odot}}\right)^{3/2}\left(\frac{M_\star}{\mathrm{M_\odot}}\right)^{-1}. \tag{2.24}$$

It is expected that the fallback debris form a circular accretion disk around the BH later. Although its detailed processes are still under debate (for a review see Bonnerot & Stone, 2020), we can roughly estimate the typical radius of the accretion disk as $R_c \simeq 2R_t/\beta$ assuming the conservation of the angular momentum of the fallback debris. Then we can roughly estimate the viscous timescale in the accretion disk as

$$t_{\rm visc} \sim \alpha^{-1}\Omega(R_c)^{-1}\left(\frac{H}{R_c}\right)^{-2} \tag{2.25}$$

$$\simeq 0.009\,\mathrm{yr}\,\beta^{-3/2}\left(\frac{\alpha}{0.1}\right)^{-1}\left(\frac{R_\star}{\mathrm{R_\odot}}\right)^{3/2}\left(\frac{M_\star}{\mathrm{M_\odot}}\right)^{-1/2}\left(\frac{H/R_c}{1}\right)^{-2}, \tag{2.26}$$

where α is the Shakura-Sunyaev viscosity parameter (Shakura & Sunyaev, 1973), $\Omega(R)$ is the angular velocity at the disk radius R, and H is the scale height of the disk. We see $t_{\rm visc} \ll t_{\rm min}$ from Equation (2.24) and Equation (2.26). Thus the accretion rate on to the BH is expected to follow the fallback rate of Equation (2.21) to some extent.

We can also naively expect that the bolometric luminosity of the emission from the accretion follows the fallback rate. However, we should take care on the Eddington limit: assuming the spherical accretion on the BH, the luminosity and accretion rate have maximum limits:

$$L_{\rm Edd} = \frac{4\pi G M_{\rm BH} m_p c}{\mu_e \sigma_T} \tag{2.27}$$

$$\simeq 1.3\times10^{44}\,\mathrm{erg\,s^{-1}}\left(\frac{\mu_e}{1}\right)^{-1}\left(\frac{M_{\rm BH}}{10^6\mathrm{M_\odot}}\right), \tag{2.28}$$

$$\dot{M}_{\rm Edd} = \frac{L_{\rm Edd}}{\eta c^2} \tag{2.29}$$

$$\simeq 2.2\times10^{-2}\,\mathrm{M_\odot\,yr^{-1}}\left(\frac{\eta}{0.1}\right)^{-1}\left(\frac{\mu_e}{1}\right)^{-1}\left(\frac{M_{\rm BH}}{10^6\mathrm{M_\odot}}\right) \tag{2.30}$$

where μ_e is the number of nucleons per free electron, σ_T is the Thomson scattering cross section, m_p is the proton mass, and η is the radiation efficiency. Comparing Equation (2.22) and Equation (2.30), we see that the peak fallback rate at $t_{\rm min}$ exceeds the

Eddington accretion rate:

$$\frac{\dot{M}_{\rm peak}}{\dot{M}_{\rm Edd}} \simeq 130 \left(\frac{\eta}{0.1}\right) \left(\frac{M_{\rm BH}}{10^6\,{\rm M}_\odot}\right)^{-3/2} \left(\frac{R_\star}{{\rm R}_\odot}\right)^{-3/2} \left(\frac{M_\star}{{\rm M}_\odot}\right)^{2}. \tag{2.31}$$

With such a high accretion rate, it is expected that relativistic jets are possibly formed although the picture is not so simple. The fallback rate decreases with time, and falls below the Eddington accretion rate at

$$t_{\rm Edd} \simeq 2.1\,{\rm yr} \left(\frac{\eta}{0.1}\right)^{3/5} \left(\frac{M_{\rm BH}}{10^6\,{\rm M}_\odot}\right)^{-2/5} \left(\frac{R_\star}{{\rm R}_\odot}\right)^{1/5} \left(\frac{M_\star}{{\rm M}_\odot}\right)^{3/5}. \tag{2.32}$$

This points out that TDEs are good probes to study the accretion dynamics because observers can monitor the transition of the accretion state from the super-Eddington one to the sub-Eddington one in a few year.

2.1.2 Observables of MS TDEs

In the episode of MS TDEs, a variety of observables are emitted. Here we review possible observational signatures from MS TDEs suggested by theoretical studies, regardless of whether they have been detected in real (see also a recent review Roth et al., 2020). We also review the present observational status in Section 2.1.4.

First, gravitational waves (GWs) are emitted in TDEs because the star and BH encounter in a close distance. The typical amplitude h and frequency f of the GWs are estimated as (Kobayashi et al., 2004),

$$h \sim \frac{GM_\star R_g}{c^2 D R_p} \tag{2.33}$$

$$\simeq 2\times 10^{-22}\beta \left(\frac{D}{10\,{\rm Mpc}}\right)^{-1} \left(\frac{M_{\rm BH}}{10^6\,{\rm M}_\odot}\right)^{2/3} \left(\frac{M_\star}{{\rm M}_\odot}\right)^{4/3} \left(\frac{R_\star}{{\rm R}_\odot}\right)^{-1}, \tag{2.34}$$

$$f \sim \left(\frac{GM_{\rm BH}}{R_p^3}\right)^{1/2} \tag{2.35}$$

$$\simeq 6\times 10^{-4}\,{\rm Hz}\,\beta^{3/2} \left(\frac{M_\star}{{\rm M}_\odot}\right)^{1/2} \left(\frac{R_\star}{{\rm R}_\odot}\right)^{-3/2}, \tag{2.36}$$

where D is the distance from the Earth to the event. Because the orbit is parabolic, the waveform is burst-like rather than inspiral (East, 2014). We cannot expect emission of strong GWs after the disruption because the debris is not compact enough. Although the frequency is accessible to Laser Interferometer Space Antenna (LISA) (Amaro-Seoane et al., 2017), its amplitude is so low that TDEs outside the Local Group cannot be detected with LISA. There is another way to emit GWs in TDEs. Weaker GWs with higher frequency are emitted by time variation of star's quadrupole moment due to the tidal deformation (Guillochon et al., 2009; Stone et al., 2013).

Second, electro-magnetic signatures are naturally emitted in MS TDEs. The tidal compression of the star in the disruption phase can cause a shock breakout, resulting in a flash in X-ray and/or γ-ray (Kobayashi et al., 2004; Brassart & Luminet, 2008; Guillochon et al., 2009; Brassart & Luminet, 2010; Stone et al., 2013; Gafton & Rosswog, 2019; Yalinewich et al., 2019). The unbound debris escaping from the BH could produce emission mainly in radio via interactions with an environmental medium, although it is highly dependent on the profile of the medium (Guillochon et al., 2016; Yalinewich et al., 2019). On the other hand, most previous works have studied emission powered by the bound debris. There are mainly two scenarios to produce emission from bound debris in optical/ultra-violet (UV) wavelength, while the unique $t^{-5/3}$ power-law of the emission shown in Equation (2.22) is commonly expected. A scenario expects that the emission is powered by collisions between a proceeding part of the debris stream and a trailing one (Shiokawa et al., 2015; Piran et al., 2015; Jiang et al., 2016b; Hayasaki et al., 2016; Lu & Bonnerot, 2020). In the scenario, the proceeding stream falling back to the BH experiences the apsidal precession by the general relativistic gravity of the BH, and then collides with the trailing part (for a review see Stone et al., 2019). The collisions produce shock in the stream, and would power the bright emission. The detail of the apsidal precession would affect observables, and thus in principle we could check aspects of the general relativity such as the no-hair theorem (§6.1 in Stone et al., 2019). In the other scenario, the emission is powered by an accretion disk, and is reprocessed by surrounding outflows (Loeb & Ulmer, 1997; Strubbe & Quataert, 2009; Lodato & Rossi, 2011; Metzger & Stone, 2016; Roth et al., 2016; Roth & Kasen, 2018; Dai et al., 2018). Once the accretion disk is rapidly formed, the accretion rate is super-Eddington and thus it is expected that most of the bound debris is expelled as outflows. Seed photons produced in the accretion disk are X-rays and have high temperature. They interact with the surrounding outflows and are reprocessed to optical/UV wavelength. If relativistic jets are formed, they could produce the brightest emission covering broad wavelength from radio to γ-ray (for a review see De Colle & Lu, 2020). As same as in the gamma-ray bursts (GRBs) (e.g. Sari et al., 1998), interactions between the relativistic jets and an environmental medium could produce forward shock, which causes synchrotron emission in radio by accelerations of electrons in the shock (Giannios & Metzger, 2011; Metzger et al., 2012; Mimica et al., 2015; Generozov et al., 2017). High-energy photons in X-ray and γ-ray is originated from inverse Comptonization of high-energy electrons in the relativistic jets (De Colle et al., 2012; Tchekhovskoy et al., 2014; Kelley et al., 2014; Curd & Narayan, 2019). Note that thermal emission from the accretion disk could also be bright in X-ray if it is not reprocessed. This is a classical expectation of emission from TDEs (e.g. Evans & Kochanek, 1989; Rees, 1990; Cannizzo et al., 1990). If environments are rich in dust, infrared emission is expected to emerge via reprocessing (Lu et al., 2016) or via dust echo (Dou et al., 2016).

Third, high-energy neutrinos, cosmic rays, and γ-rays could also be emitted in TDEs. Acceleration processes are expected to take place in relativistic jets (Dai & Fang, 2017; Alves Batista & Silk, 2017; Zhang et al., 2017; Liu et al., 2020a) and/or in an accretion disk (Hayasaki & Yamazaki, 2019; Murase et al., 2020; Winter & Lunardini, 2020).

2.1.3 Rates of MS TDEs

TDEs occur when a star and a BH encounter so close that the pericenter radius is smaller than $\simeq 0.5$ AU if we consider a solar-type star is disrupted by an SMBH with $10^6\,\mathrm{M}_\odot$. Such an extreme orbit is realized in a dense star cluster hosting an MBH, for example, a galactic nucleus and globular cluster. In this Section, we review a canonical model used to calculate event rates of TDEs in those systems, called the loss-cone theory (see also reviews Merritt, 2013; Alexander, 2017; Stone et al., 2020).

The central MBH traps environmental stars in its gravitational potential. The radius of the region where the gravity of the MBH exceeds that of background stars, called as the influence radius, is calculated as

$$\begin{aligned} r_h &= GM_{\mathrm{BH}}/\sigma^2 && (2.37)\\ &\simeq A\,\mathrm{pc}\left(\frac{M_{\mathrm{BH}}}{10^8\,\mathrm{M}_\odot}\right)^B, && (2.38)\end{aligned}$$

where σ is the velocity dispersion. A and B are respectively estimated as 16 and 0.69 in Stone & Metzger (2016), which fit observations of nearby galactic nuclei with Equation (2.38). Total mass of the background stars within the influence radius is $\mathcal{O}(M_{\mathrm{BH}})$. The two-body relaxation timescale is

$$t_{\mathrm{relax}} \sim 0.1\frac{N}{\ln N}t_{\mathrm{orb}}, \tag{2.39}$$

where N is the number of stars in the system and t_{orb} is the orbital timescale, which can be estimated as Equation (2.17). For galactic nuclei and globular clusters considered here, the relaxation timescale is smaller than the Hubble time, and thus the system is collisional. Then stars exchange their orbital energy and angular momentum via two-body scatterings, and by other processes such as the resonant relaxation (Rauch & Tremaine, 1996).

The Kepler motion of a star can be expressed as

$$\begin{aligned} R_p &= a(1-e), && (2.40)\\ \epsilon &= \frac{GM_{\mathrm{BH}}}{2a}, && (2.41)\end{aligned}$$

$$\begin{aligned} 0 = \left(\frac{\mathrm{d}r}{\mathrm{d}t}\right)^2 &= \epsilon - \frac{GM_{\mathrm{BH}}}{R_p} + \frac{j^2}{R_p^2}, && (2.42)\\ j^2 &= 2R_p^2\left(\frac{GM_{\mathrm{BH}}}{R_p} - \epsilon\right), && (2.43)\end{aligned}$$

where e is the eccentricity, $-\epsilon$ is the specific orbital energy, and j is the specific angular momentum. We also use an approximation of $M_{\mathrm{BH}} \gg M_\star$. When $R_p < R_t$, the star is lost by the TDE in the orbital timescale $t_{\rm orb}$, and the orbit is called as the loss-cone orbit. The condition can be rewritten as

$$j^2 < j_{\rm lc}^2(\epsilon) := 2R_t^2\left(\frac{GM_{\rm BH}}{R_t} - \epsilon\right) \simeq 2GM_{\rm BH}R_t, \tag{2.44}$$

where we assume $a \gg R_t$.

The TDE rate $\dot{N}_{\rm TDE}$ is thus determined by the refilling rate of the loss-cone in the phase space (ϵ, j) by relaxations. In the phase space, j takes the maximal value when the orbit is circular,

$$j_c(\epsilon) = GM_{\rm BH}a = \frac{(GM_{\rm BH})^2}{2\epsilon}. \tag{2.45}$$

The relaxation timescale of energy $\epsilon/\dot{\epsilon}$ is given by $t_{\rm relax}$ in Equation (2.39). It is also the same as the timescale for j^2 to change by order j_c^2. Thus the relaxation timescale for the angular momentum j to change by $\mathcal{O}(1)$ is

$$t_{{\rm relax},j}(j) \sim \frac{j^2}{{\rm d}j^2/{\rm d}t} \sim \left(\frac{j}{j_c(\epsilon)}\right)^2 t_{\rm relax}. \tag{2.46}$$

In phase space around loss-cone, $j \sim j_{\rm lc} \ll j_c$, and thus the relaxation timescale of the angular momentum is much shorter than that of energy. We can neglect the diffusion of ϵ in such cases.

Properties of the loss-cone depend on $\Delta j(\epsilon)$, or the root mean square of change of $j(\epsilon)$ over an orbital timescale $t_{\rm orb}$,

$$\Delta j(\epsilon) \sim \sqrt{\frac{t_{\rm orb}}{t_{\rm relax}}}\, j_c(\epsilon) \tag{2.47}$$

The point is the ratio of $\Delta j(\epsilon)$ to $j_{\rm lc}$. If $\Delta j(\epsilon) \ll j_{\rm lc}$, which is realized for larger ϵ or smaller a, a star entering into the loss-cone have $j(\epsilon) \simeq j_{\rm lc}$ or $\beta \simeq 1$, and is lost after $t_{\rm orb}$. The distribution function of stars inside the loss-cone, $j(\epsilon) \ll j_{\rm lc}$, decays exponentially, and thus it is called as the “empty loss-cone”, or “diffusive” regime. In phase space much far from the loss-cone $j \gg j_{\rm lc}$, the distribution function is not affected and thus isotropic. Conversely, if $\Delta j(\epsilon) \gg j_{\rm lc}$, which is realized for smaller ϵ and larger a, a star is often scattered deeply inside the loss-cone and also outside it before the star reaches the tidal radius. Thus this regime is called as the “full loss-cone”, or “pinhole” regime. In this case, the distribution function is almost isotropic at all $j \gtrsim j_{\rm lc}$.

The TDE rate in the empty loss-cone is derived by solving the Fokker-Planck equation with two boundary conditions that the stellar density goes to zero for $j \to j_{\rm lc}$ and to the isotropic distribution $N_{\rm iso}(\epsilon)$ for $j \to j_c$ (Lightman & Shapiro, 1977)

$$\dot{N}_{\rm TDE,empty}(\epsilon) \sim \frac{N_{\rm iso}(\epsilon)}{\ln[j_c(\epsilon)/j_{{\rm lc}(\epsilon)}]t_{\rm relax}(\epsilon)}, \tag{2.48}$$

where $N(\epsilon)\mathrm{d}\epsilon$ is the number of stars with their orbital energy in $[-\epsilon, -\epsilon + \mathrm{d}\epsilon]$. In the full loss-cone case the distribution function is uniform in $1 - e^2 \propto (j/j_{\mathrm{lc}})^2$ because it is isotropic (Frank, 1978), and thus the TDE rate can be calculated as

$$\dot{N}_{\mathrm{TDE,full}}(\epsilon) \sim \frac{j_{\mathrm{lc}}^2}{j_c^2(\epsilon)} \frac{N_{\mathrm{iso}}(\epsilon)}{t_{\mathrm{orb}}(\epsilon)}. \tag{2.49}$$

With Equation (2.43) and $\beta \propto R_p^{-1}$, we also obtain the dependence of the TDE rate on β in this case as

$$\dot{N}_{\mathrm{TDE,full}}(\beta)\mathrm{d}\beta \propto \beta^{-2}\mathrm{d}\beta. \tag{2.50}$$

The total TDE rate can be calculated as

$$\begin{aligned} \dot{N}_{\mathrm{TDE}} &= \int_0^\infty \mathrm{d}\epsilon \dot{N}_{\mathrm{TDE}}(\epsilon) && (2.51) \\ &\sim \int_0^{\epsilon_c} \mathrm{d}\epsilon \dot{N}_{\mathrm{TDE,full}} + \int_{\epsilon_c}^\infty \mathrm{d}\epsilon \dot{N}_{\mathrm{TDE,empty}}, && (2.52) \end{aligned}$$

where ϵ_c is the critical orbital energy where $\Delta j(\epsilon_c) = j_{\mathrm{lc}}$. We also take the critical radius r_c as $r_c \sim GM_{\mathrm{BH}}/\epsilon_c$. If $r_c \ll r_h$, most TDEs arise from $a \sim r_c$. Conversely, if $r_c \gg r_h$, most TDEs arise from $a \sim r_h$, and are dominated by contributions from the empty loss-cone regime.

Based on this framework, more detailed modeling of nearby galactic nuclei have been performed (Syer & Ulmer, 1999; Magorrian & Tremaine, 1999; Wang & Merritt, 2004; Stone & Metzger, 2016). The works considered TDEs where an SMBH disrupts an MS. It is shown that $r_c \sim r_h$ for most galactic nuclei, while heavy SMBHs with $\gtrsim 10^9\,\mathrm{M}_\odot$ have $r_c \gtrsim 10\,r_h$. Note that such a massive SMBH swallows an MS before the tidal disruption, and thus we cannot expect TDEs (see also Section 2.2.1). Then we can roughly estimate the TDE rate with Equation (2.48) as

$$\begin{aligned} \dot{N}_{\mathrm{TDE}} &\sim \frac{N(r < r_h)}{\ln(\sqrt{r_h/R_t})t_{\mathrm{relax}}(r_h)} && (2.53) \\ &\sim 2 \times 10^{-4}\,\mathrm{yr}^{-1} \left(\frac{N(r < r_h)}{10^6}\right) \left(\frac{t_{\mathrm{relax}}(r_h)}{7 \times 10^8\,\mathrm{yr}}\right), && (2.54) \\ & && (2.55) \end{aligned}$$

where we neglect the weak dependence of the logarithmic term, and consider $r_h = 1\,\mathrm{pc}$, $M_{\mathrm{BH}} = 10^6\,\mathrm{M}_\odot$, and a solar type star. It is also clear that we can approximate orbits in most TDEs as parabolic because most stars are injected at r_h or r_c, meaning that $R_t \ll r_h$ and $R_t \ll r_c$, or $1 - e \ll 1$. The rough estimate is still reasonable: Wang & Merritt (2004) gives the following scaling relation

$$\dot{N}_{\mathrm{TDE}} \simeq 7.1 \times 10^{-4}\,\mathrm{yr}^{-1} \left(\frac{\sigma}{70\,\mathrm{km\,s}^{-1}}\right)^{7/2} \left(\frac{M_{\mathrm{BH}}}{10^6\,\mathrm{M}_\odot}\right), \tag{2.56}$$

which gives similar value to Equation (2.54). With the $M_{\rm BH} - \sigma$ relation (e.g. Ferrarese & Merritt, 2000), we see $\dot{N}_{\rm TDE} \propto M_{\rm BH}^{-0.25}$, which implies that TDE rates are higher for lower mass BHs, or in smaller galaxies. Note that the scaling relation is revised in Stone & Metzger (2016) as

$$\dot{N}_{\rm TDE} \simeq 1.9 \times 10^{-4}\,{\rm yr}^{-1} \left(\frac{M_{\rm BH}}{10^6\,{\rm M}_\odot} \right)^{-0.404} . \tag{2.57}$$

The theoretical event rates given by the empirical modeling are consistent with observations. van Velzen (2018) measured mass and luminosity functions of TDEs based on a sample of 17 TDEs detected in optical. They showed that TDE rates per galaxy can be fitted as $10^{-4}\,{\rm yr}^{-1}$, unless the BH mass is so large that TDE rates are suppressed by the swallow of stars. Previously it had been suggested that there was a discrepancy between the theoretical TDE rates and observational ones (Kochanek, 2016), but it could be caused by the missing of fainter TDEs in early surveys.

2.1.4 Observations of MS TDEs

In this Section, we review the observational status of MS TDEs. First, we explain a brief history of MS TDE observations and future prospects. Then we review notable MS TDEs among a large sample of the observations. See also recent review articles on the observations of TDEs in radio (Alexander et al., 2020), in optical/UV (van Velzen et al., 2020b), and in X-ray (Saxton et al., 2020).

In the beginning, the first TDEs were discovered by the X-ray telescope ROSAT. They were identified as TDEs because they were found in centers of quiescent galaxies, which denied their origin as active galactic nuclei (AGN) variability, and also because they showed the $t^{-5/3}$ power-law light curves (e.g. Bade et al., 1996; Grupe et al., 1999; Komossa & Bade, 1999). Later, discoveries of TDEs were contributed by UV/X-ray telescopes, The Galaxy Evolution Explorer (GALEX), XMM-Newton, Chandra, and Swift (Esquej et al. 2007, 2008; Lin et al. 2011; Saxton et al. 2012; for a review see Komossa 2015). From around 2010, optical surveys led to detections of TDEs. They are contributed by the Sloan Digital Sky Survey (SDSS), the Panoramic Survey Telescope and Rapid Response System (Pan-STARRS), Palomar Transient Factory (PTF), intermediate Palomar Transient Factory (iPTF), the All Sky Automated Survey for supernovae (ASAS-SN), the Asteroid Terrestrial-impact Last Alert System (ATLAS), and the Optical Gravitational Lensing Experiment (OGLE) (for a review see van Velzen et al., 2020b). Those projects respectively have found a few TDEs. Recently, the Zwicky Transient Facility (ZTF) joined the optical surveys of TDEs, and is the most powerful tool to find TDEs now. van Velzen et al. (2020a) reported 17 TDEs discovered in the first half of the ZTF survey. Now there are about 50 TDE candidates with good certainties in total (Graham et al., 2019), and more speculative TDE candidates with less certainties (e.g. Auchettl et al., 2017). In near future, the Extended ROentgen Survey with An Imaging Telescope Array (eROSITA), which is already in operations, would efficiently detect TDEs bright in X-rays (Khabibullin et al., 2014). A sample of optically bright TDEs would also dramatically increase by the Large Synoptic Survey Telescope (LSST) on the Vera C. Rubin Observatory (Bricman & Gomboc, 2020). GW background signals of MS TDEs are possibly detected with the Big Bang Observer (Toscani et al., 2020).

First, we focus on the ROSAT TDEs (e.g. Bade et al., 1996; Grupe et al., 1999; Komossa & Bade, 1999). Their locations coincident with galactic nuclei and $t^{-5/3}$ power-law light curves strongly indicate their origins as TDEs. Their peak luminosity up to a few $10^{44}\,\mathrm{erg\,s^{-1}}$ and their blackbody temperature of $\sim 0.1\,\mathrm{keV}$ are also consistent with theoretical predictions at that time (e.g. Evans & Kochanek, 1989; Rees, 1990; Cannizzo et al., 1990).

Second, we review notable TDEs found in the optical surveys. The optical TDEs are usually bright in both optical and UV, and thus are also called optical-UV TDEs (e.g. van Velzen et al., 2020b). PS1-10jh (Gezari et al., 2012) is the first TDE with multiple detections before its peak and multiple spectroscopic observations. The rich observations of the event make it a representative of optical TDEs, and motivate theorists to develop detailed modeling of optical TDEs (e.g. Guillochon et al., 2014). ASASSN-15lh (Leloudas et al., 2016) is the most luminous optical TDE, and also is the most luminous optical transient, with its peak luminosity $\simeq 2 \times 10^{45}\,\mathrm{erg\,s^{-1}}$ and $M_V = -23.5$ mag. Note that different origins for the event, such as a superluminous supernova (SLSN), are also proposed (Dong et al., 2016). The SMBH mass implied from the bulge mass and luminosity of the host galaxy are respectively $\simeq 10^{8.88}\,\mathrm{M_\odot}$ and $\simeq 10^{8.50}\,\mathrm{M_\odot}$, indicating the encounter between a star and the SMBH is general relativistic. A spin of the SMBH is constrained because a slowly spinning SMBH cannot disrupt the star before it enters the horizon radius.

Third, there are historical observations of 3 TDEs with on-axis relativistic jets discovered by Swift as ultra-long GRBs (Levan et al., 2011; Bloom et al., 2011; Burrows et al., 2011; Zauderer et al., 2011; Cenko et al., 2012; Brown et al., 2015). They show high-energy emission in X-ray and γ-ray lasting for more than 10^5 s, which is outstandingly long among observed GRBs (Levan et al., 2014). Such long timescales would be caused by the fallback timescale (see Equation (2.24)). Kara et al. (2016) performed X-ray reverberation observations for one of the events, Swift J1644+57, and thus probed geometry around relativistic jets. ASASSN-14li is another possible TDE with relativistic jets (e.g Miller et al., 2015; Alexander et al., 2016; Holoien et al., 2016; van Velzen et al., 2016a). Unlike the previous 3 TDEs, ASASSN-14li is bright in optical. ASASSN-14li is a rare class of TDEs with detections not only in optical but also in radio and X-ray. Relativistic jets are one of the possible origins to explain such multi-wavelength emission, while other scenarios such as non-relativistic outflow are proposed (Alexander et al., 2016). Quasi periodic oscillations (QPOs) of X-ray flux with 131 s period are also detected for the event (Pasham et al., 2019).

Forth, some TDEs are detected in infra-red. There are detections of dust echo from TDEs (Jiang et al., 2016a; van Velzen et al., 2016b; Dou et al., 2016; Jiang et al., 2017; Wang et al., 2018; Jiang et al., 2019), and reprocessed emission where higher energy emission is obscured by dust (Tadhunter et al., 2017; Dou et al., 2017; Yang et al., 2019; Kool et al., 2020). Mattila et al. (2018) reported a dust-obscured TDE, Arp 299-B AT1, where off-axis relativistic jets are probed by its radio observations.

Other peculiar TDEs have also been reported. While most TDEs have been detected in quiescent galaxies, TDEs in AGN have been detected (Blanchard et al., 2017; Liu et al., 2020b). Possible candidates of TDEs where an IMBH disrupts a star are reported (Lin et al., 2018, 2020). There is a TDE having a plausible association with a high-energy neutrino event (Stein et al., 2020), which is the first possible counterpart of a multi-messenger signal from TDEs.

2.2 Tidal Disruption Events of White Dwarfs

We review MS TDEs in Section 2.1, which are the most common TDEs and thus are a point of reference to study various types of TDEs. Hereafter, we focus on TDEs where a white dwarf (WD) is disrupted. In this Section, we review the current understandings of characteristics of WD TDEs different from MS TDEs, event rates of WD TDEs, the observational status of WD TDEs, and a variety of WD TDEs finally. The last point is tightly related to the motivation of the study of this thesis. See also a recent review article on WD TDEs: Maguire et al. (2020).

2.2.1 Characteristics of WD TDEs

A WD has a typical mass of $\sim 0.6\,\mathrm{M}_\odot$, radius of $\sim 10^9\,\mathrm{cm}$, and density of $\sim 10^7\,\mathrm{g\,cm^{-3}}$, which is much more compact and denser than an MS star (e.g. Shapiro & Teukolsky, 1983). Its self-gravity is dominantly balanced by the degenerate pressure of electron gas.

WD TDEs have two unique features. First, the range of the BH mass is restricted to stellar and intermediate masses. This is because a BH with its mass $M_{\mathrm{BH}} \gtrsim 10^5\,\mathrm{M}_\odot$ swallows a WD inside its horizon radius before tidally disrupting the WD (Luminet & Pichon, 1989b).

Quantitative discussions of the condition is as follows: the horizon radius of a BH R_{BH} is

$$R_{\mathrm{BH}} = \eta \frac{G M_{\mathrm{BH}}}{c^2}, \tag{2.58}$$

where c is the speed of light and η ranges from 1 to 9 depending on the BH spin. A spinless, Schwarzschild BH has $\eta = 2$, and then $R_{\mathrm{BH}} = R_S := 2GM_{\mathrm{BH}}/c^2$. For simplicity, we consider a Schwarzschild BH hereafter. The angular momentum of a star approaching the BH is written as follows in Schwarzschild metric,

$$j = (R_S R_p c^2)^{1/2} \left(1 - \frac{R_S}{R_p}\right)^{-1/2}. \tag{2.59}$$

The star is swallowed by the BH when $j \leq 2R_S c$, $R_p \leq 2R_S$, or

$$\beta \gtrsim 10 \left(\frac{R_\star}{10^9\,\mathrm{cm}}\right) \left(\frac{M_{\mathrm{BH}}}{10^3\,\mathrm{M}_\odot}\right)^{-2/3} \left(\frac{M_\star}{0.6\,\mathrm{M}_\odot}\right)^{-1/3} \tag{2.60}$$

$$= 12 \left(\frac{R_\star}{\mathrm{R}_\odot}\right) \left(\frac{M_{\mathrm{BH}}}{10^6\,\mathrm{M}_\odot}\right)^{-2/3} \left(\frac{M_\star}{\mathrm{M}_\odot}\right)^{-1/3}, \tag{2.61}$$

where we consider a WD in Equation (2.60) and an MS in Equation (2.61). Combined with the condition of the tidal disruption, $\beta > 1$, we obtain the maximum BH mass, or the Hills mass, as

$$M_{\mathrm{Hills}} = 9.0 \times 10^4\,\mathrm{M}_\odot \left(\frac{R_\star}{10^9\,\mathrm{cm}}\right)^{3/2} \left(\frac{M_\star}{0.6\mathrm{M}_\odot}\right)^{-1/2} \tag{2.62}$$

$$= 4.0 \times 10^7\,\mathrm{M}_\odot \left(\frac{R_\star}{\mathrm{R}_\odot}\right)^{3/2} \left(\frac{M_\star}{\mathrm{M}_\odot}\right)^{-1/2} . \tag{2.63}$$

Note that the Hills mass is slightly modified if the stellar structure is considered (Luminet & Pichon, 1989b; Law-Smith et al., 2017; Mainetti et al., 2017). The encounter is a collision between a star and a BH rather than a TDE if $R_p \leq R_\star$, or

$$\beta \geq (M_{\mathrm{BH}}/M_\star)^{1/3} . \tag{2.64}$$

These 3 conditions give a parameter space where TDEs occur, shown in Figure 2.2.

We see that BHs with their masses $\gtrsim 10^5\,\mathrm{M}_\odot$ cannot cause WD TDEs. If a WD is swallowed before disruption, there would be no observable signal except for GWs (East, 2014). In contrast, other types of stars, such as MSs and giant stars, can be disrupted by SMBHs (Kobayashi et al., 2004; Law-Smith et al., 2017). In this sense, WD TDEs can be unique probes of IMBHs.

The second feature is the explosive thermonuclear reactions in a WD. They are caused by strong compression owing to the tides perpendicular to the orbital plane. Such adiabatic compression leads to shock heating during the pericenter passage (Carter & Luminet, 1982, 1983; Bicknell & Gingold, 1983; Luminet & Pichon, 1989a; Kobayashi et al., 2004; Stone et al., 2013). The shock increase the density and temperature, and possibly ignite thermonuclear reactions and detonation, resulting in an explosion of the WD (Luminet & Pichon, 1989b; Wilson & Mathews, 2004). Hydrodynamic simulations of WD TDEs showed that thermonuclear explosions indeed realized if the encounters are deep enough, or β is large enough (Rosswog et al., 2008, 2009; Haas et al., 2012; Holcomb et al., 2013; Tanikawa et al., 2017; Tanikawa, 2018a,b; Kawana et al., 2018; Anninos et al., 2018, 2019), although Tanikawa et al. (2017) pointed out that very high spatial resolution of $< 10^6$ cm is needed to accurately follow the explosion processes. If a substantial amount of radioactive nuclei, such as ^{56}Ni, are synthesized in the unbound debris of the WD, their decays supply nuclear energy into the debris, and the event may appear as a transient similar to SNe Ia (MacLeod et al., 2016). In MS TDEs, such emission powered by radioactive nuclei is not expected because the density and temperature are not high enough to synthesize those radioactive nuclei (Carter & Luminet, 1982, 1983; Luminet & Pichon, 1989a). In this sense, the emission powered by the thermonuclear explosions is a unique feature of WD TDEs. Once heavier nuclei are synthesized and are accelerated to be ultra high-energy cosmic rays (UHECRs) around the IMBH, they might be an origin of UHECRs of heavy nuclei (Zhang et al., 2017).

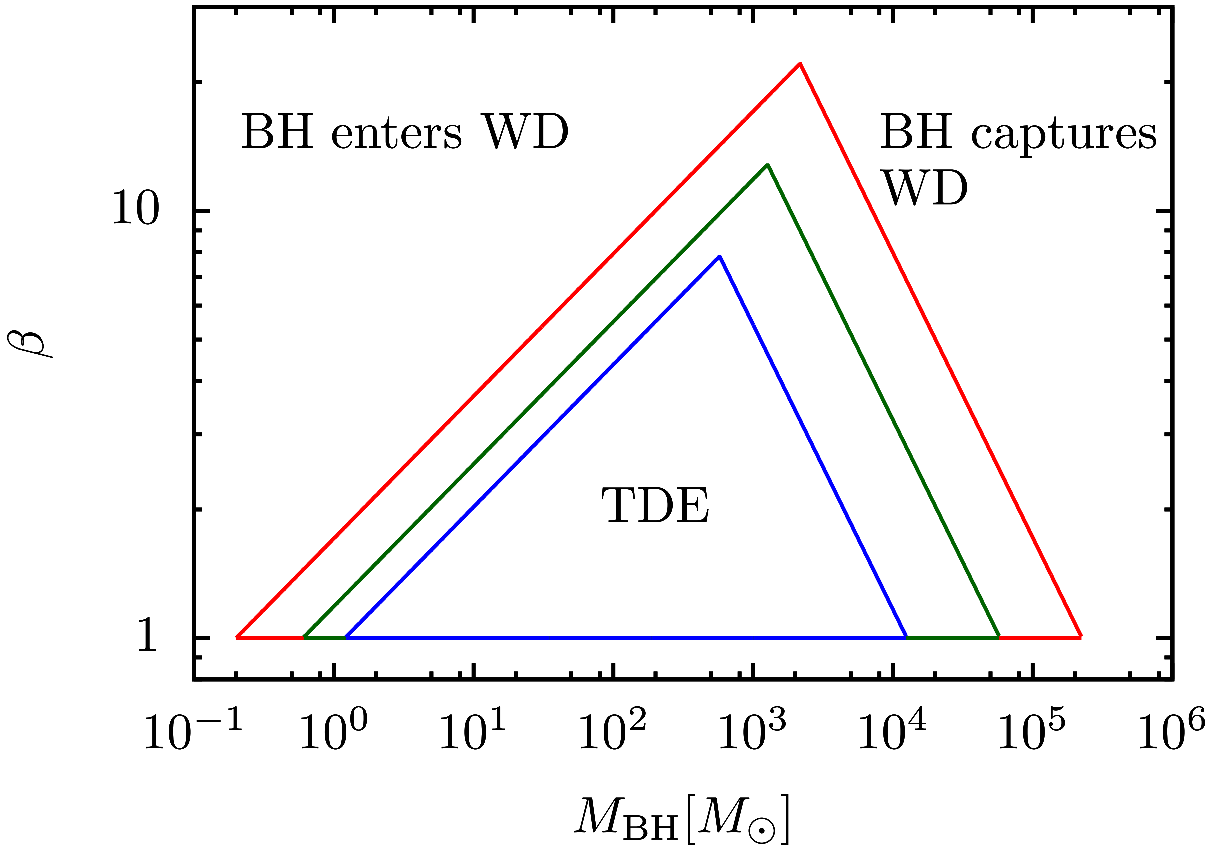

Figure 2.2: Parameter spaces where WD TDEs occur. The red, green, and blue lines are for $M_{\rm WD} = 0.2$, 0.6, and $1.2\,{\rm M}_{\odot}$, respectively. The areas inside the triangles, respectively, correspond to the parameter spaces where TDEs occur. The original figure is given in Luminet & Pichon (1989b)

2.2.2 Rates of WD TDEs

An event rate of WD TDEs is very uncertain, which reflects unknown natures of IMBHs. There is almost no observational constraint on the WD TDE rate because we have no certain detection of WD TDEs, while several candidates have been proposed (see Section 2.2.3). Still, it is possible to theoretically estimate the WD TDE rate with several assumptions, and such studies are important to construct strategies to search for WD TDEs. In this Section, we review previous works estimating WD TDE rates.

To host WD TDEs, their environments are needed to be dense star clusters harboring IMBH(s) and to be old enough that a fraction of stars evolve to WDs. Two possible sites have been considered: centers of dwarf galaxies and globular clusters. The former case was studied in MacLeod et al. (2014). They applied the loss-cone theory and took parameters as those of centers of dwarf galaxies, extrapolating relationships such as the $M_{\rm BH}$–σ relation derived for SMBHs to IMBHs (Kormendy & Ho, 2013). They found that $r_c \ll r_h$ is realized in centers of dwarf galaxies, and thus a contribution from the full loss-cone is dominant. Stellar distributions are relaxed by either two-body scattering or mass-precession resonant relaxation (e.g. Merritt, 2013). They found the WD TDE rate per BH in dwarf galaxies as

$$\dot{N}_{\rm WD\,TDE,\,dg} \sim 10^{-6}\,{\rm yr}^{-1}\,{\rm BH}^{-1}, \tag{2.65}$$

and the MS TDE rate as $\sim 10^{-4}\,{\rm yr}^{-1}\,{\rm BH}^{-1}$. The 1 % ratio of WD TDEs to MS TDEs can be intuitively understood as follows: TDE rate is proportional to the size of the loss-cone $j_{\rm lc}^2$ (see Equation (2.49)). With the equations between $j_{\rm lc}$, R_t, and the stellar profile (Equation (2.8) and Equation (2.44)), we obtain that $\dot{N}_{\rm TDE,full} \propto (M_\star/R_\star^3)^{-1/3}$. Because the density of a WD is $\sim 10^6$ times larger than that of an MS, we see the WD TDE rate is about 1% of the MS TDE rate. The number density of dwarf galaxies and the occupation fraction of IMBHs in dwarf galaxies, or the mass function of IMBHs, has not been accurately measured. MacLeod et al. (2016) parameterized the IMBH mass function with a power-law function, extrapolating that of SMBHs. Assuming a log-flat distribution, we expect a number density of IMBHs as $n_{\rm IMBH} \simeq 0.02\,{\rm Mpc}^{-3}$. Then we obtain volumetric WD TDE rate in dwarf galaxies as

$$\dot{n}_{\rm WD\,TDE,\,dg} \sim 20\,{\rm Gpc}^{-3}\,{\rm yr}^{-1}. \tag{2.66}$$

WD TDE rates in globular clusters are modeled in Baumgardt et al. (2004a,b). They performed N-body simulations of globular clusters harboring a 1000 $\rm M_\odot$ IMBH, and found that the fraction of WD TDEs are $\simeq 9$ % in all types of TDEs, including MS TDEs, WD TDEs, and TDEs where giants are disrupted. The fraction is larger than that in centers of dwarf galaxies, $\sim 1\%$, likely because of stronger mass-segregation effects and shorter relaxation timescales of globular clusters. They also applied their numerical models to observed globular clusters, and showed that the total TDE rate per globular cluster hosting an IMBH is $\sim 10^{-9}$–$10^{-7}\,{\rm yr}^{-1}$, depending on core profiles of the globular clusters. Combined with the $\simeq 9$ % fraction of WD TDE rates, WD TDE rates in globular clusters are estimated to be

$$\dot{N}_{\rm WD\,TDE,\,gc} \sim 10^{-10}\text{–}10^{-8}\,{\rm yr}^{-1}\,{\rm BH}^{-1}. \tag{2.67}$$

Ramirez-Ruiz & Rosswog (2009) also made a simple estimation of the total TDE rate per globular cluster as $\sim 10^{-7}\,\mathrm{yr}^{-1}$ based on the loss-cone theory (Frank & Rees, 1976), which is consistent with the results of Baumgardt et al. (2004a,b). To calculate the volumetric rate of WD TDEs in globular clusters, we still need to know the number density of globular clusters and the occupation fraction of IMBHs, which are very uncertain. Volumetric number density of globular clusters were estimated as $n_{\mathrm{GC}} \simeq 34\,\mathrm{Mpc}^{-3}$ in McLaughlin (1999), and as $n_{\mathrm{GC}} \simeq 4\,\mathrm{Mpc}^{-3}$ in Brodie & Strader (2006). Haas et al. (2012) and Shcherbakov et al. (2013) respectively took those values, and assumed optimistic occupation fraction of unity. The resultant volumetric rates of WD TDEs in globular clusters are

$$\dot{n}_{\mathrm{WD\,TDE,\,gc}} \sim 500\,\mathrm{Gpc}^{-3}\,\mathrm{yr}^{-1}\left(\frac{n_{\mathrm{gc}}}{40\,\mathrm{Mpc}^{-3}}\right). \tag{2.68}$$

Instead of using the volumetric number density of globular clusters, it is also possible to use number density of globular clusters per galaxy with mass/luminosity functions of galaxies (Toscani et al., 2020). Because of the large uncertainties in the number densities of globular clusters and occupation fraction of IMBHs, different assumptions for them can result in event rates different by a few orders of magnitude (Fragione et al., 2018).

As we have discussed, there is large uncertainty in a WD TDE rate. Even it is still not clear which contribution from centers of dwarf galaxies or globular clusters is dominant. Other exotic scenarios would subdominantly contribute to the WD TDE rate. Another site of WD TDEs was considered in Fragione et al. (2020), which studied rates of WD TDEs where a WD approaches a stellar mass BH with the help of Lidov-Kozai oscillations by a tertiary star. They estimated the volumetric event rate as 1.2×10^{-4}–$1.4\,\mathrm{Gpc}^{-3}\,\mathrm{yr}^{-1}$ for $z \leq 0.1$, and thus the contribution from this scenario would be likely subdominant.

Despite the large uncertainty, it is still useful to derive a scaling relation of a volumetric WD TDE rate as (MacLeod et al., 2016)

$$\dot{n}_{\mathrm{WD\,TDE}} \sim 10\,\mathrm{Gpc}^{-3}\mathrm{yr}^{-1}\left(\frac{\dot{N}_{\mathrm{WD\,TDE}}}{10^{-6}\,\mathrm{yr}^{-1}\,\mathrm{BH}^{-1}}\right)\left(\frac{n_{\mathrm{IMBH}}}{0.01\,\mathrm{Mpc}^{-3}}\right). \tag{2.69}$$

The event rate of WD TDEs with thermonuclear explosions is also of interest. A deep penetration of a WD, $\beta > \beta_{\mathrm{thermo}} \simeq 4$, is needed to ignite thermonuclear explosions (Kawana et al., 2018). Then a fraction of WD TDEs with thermonuclear explosions is $\beta_{\mathrm{thermo}}^{-1}$ (see Equation (2.50)), if we assume that the full loss-cone contribution is dominant as same as in dwarf galaxies. Finally we obtain

$$\dot{n}_{\mathrm{WD\,TDE,\,thermo}} \sim 2.5\,\mathrm{Gpc}^{-3}\,\mathrm{yr}^{-1}\left(\frac{\dot{N}_{\mathrm{WD\,TDE}}}{10^{-6}\,\mathrm{yr}^{-1}\,\mathrm{BH}^{-1}}\right)\left(\frac{n_{\mathrm{IMBH}}}{0.01\,\mathrm{Mpc}^{-3}}\right)\left(\frac{\beta_{\mathrm{thermo}}}{4}\right)^{-1}. \tag{2.70}$$

We emphasize that the estimated event rate is very uncertain. The theoretically estimated value of $\dot{N}_{\mathrm{WD\,TDE}}$ ranges 10^{-10}–$10^{-6}\,\mathrm{BH}^{-1}\,\mathrm{yr}^{-1}$, depending on a profile of a star cluster containing an IMBH. There is almost no observational constraint on the number density of IMBHs n_{IMBH}, where we take a fiducial value of $0.01\,\mathrm{Mpc}^{-3}$ here by extrapolating the mass function of SMBHs to that of IMBHs with a log-flat distribution (we will discuss this issue in Section 5.3 in detail). The ratio of WD TDEs with thermonuclear explosions to all the WD TDEs, corresponding to $\beta_{\mathrm{thermo}}^{-1}$ in the full loss-cone case, is less uncertain than the former two factors. It ranges within a factor of a few depending on numerical simulations (Rosswog et al., 2009; Kawana et al., 2018; Anninos et al., 2018, 2019), although it is not observationally constrained.

2.2.3 Observations of WD TDEs

Observationally, there are a few possible candidates of WD TDEs, but they are not confirmed as WD TDEs and other origins are possible. A class of WD TDE candidates is ultra-long GRBs. Krolik & Piran (2011) proposed a WD TDE origin for a TDE with relativistic jets, Swift J1644+57, although an MS TDE origin is more natural (for a review see Komossa, 2015). Two ultra-long GRBs associated with SNe are also proposed as WD TDE candidates (Shcherbakov et al., 2013; Ioka et al., 2016). Other origins for those transients are possible such as a collapse model and a magnetar model (Dainotti et al., 2007; Nakar, 2015; Bersten et al., 2016; Gao et al., 2016).

Other WD TDE candidates are X-ray transients with their timescales consistent with the fallback timescale of WD TDEs (see Equation (2.24)). They are modeled to be powered by an accretion disk or relativistic jets formed in WD TDEs, and thus their light curves would reflect the fallback timescale (Jonker et al., 2013; Bauer et al., 2017; Peng et al., 2019). Shen (2019) proposed that so-called fast ultraluminous X-ray transients can be explained with partial disruptions of a WD by an IMBH. However, origin(s) of these events have not been conclusively determined (Irwin et al., 2016; Bauer et al., 2017).

Some optical transients recently found are also WD TDE candidates. Kuin et al. (2019) proposed a WD TDE origin for AT2018cow, one of fast blue optical transients (FBOTs). However, appearance of hydrogen lines probably disfavors the WD TDE origin (e.g. Margutti et al., 2019). Calcium-rich transients (Ca-rich) transients are also possible candidates of WD TDEs (Sell et al., 2015). Sell et al. (2018) performed X-ray follow-up observations of a Ca-rich transient, SN2016hnk, expecting detection of X-ray emission from an accretion disk formed in a WD TDE, but it was not detected. SN2019bkc, a Ca-rich transient showing the most rapidly declining light curve among type I SNe (Chen et al., 2020), is also considered as a WD TDE candidate in Prentice et al. (2020). A caveat in the WD TDE scenario is again non-detection in X-ray, and there are other possible scenarios.

Despite the little observations of plausible WD TDEs in the current era, it is expected that WD TDEs would be possibly detected in a near future. Although there is a large uncertainty in expected detection rates (see Section 2.2.2), MacLeod et al. (2016) estimated the detection rate of thermonuclear emission of WD TDEs by LSST as $\sim 14\,\mathrm{yr}^{-1}$ if the mass function of IMBHs is log-flat and is extrapolated from that of SMBHs. Malyali et al. (2019) estimated the detection rate of X-ray emission from WD TDEs by eROSITA as 3 events in its 4-year survey. Toscani et al. (2020) estimated GW background signal emitted from WD TDEs, and showed that it would be detectable with ALIA, DECI-hertz interferometer Gravitational wave Observatory (DECIGO), and the Big Bang Observer (BBO).

2.2.4 Variety of WD TDEs

WD TDEs intrinsically have a large variety in their parameters, the WD/BH masses and penetration parameter β, which can result in a variety of observational signatures. Thermonuclear explosions in WD TDEs would also be diverse, while it is difficult to analytically estimate the variety or dependence on the parameters because WD TDEs show complex dynamical evolutions. Hydrodynamic simulations of WD TDEs have been performed for a variety of parameter sets of ($M_{\rm BH}$, $M_{\rm WD}$, β) (Rosswog et al., 2008, 2009; Haas et al., 2012; Holcomb et al., 2013; Tanikawa et al., 2017; Tanikawa, 2018a,b; Kawana et al., 2018; Anninos et al., 2018, 2019) , showing that hydrodynamic and nucleosynthetic results range widely depending on the parameters. Kawana et al. (2018) performed the largest parameter study considering 180 parameter sets, and showed that there is indeed a large variety in quantities tightly related to the thermonuclear emission, such as the ejecta mass, ^{56}Ni mass, and explosion energy (see Figure 2.3).

MacLeod et al. (2016) was a unique study in the sense that they derived concrete observational signatures of a WD TDE, such as multi-band light curves and spectral evolutions. They considered a carbon-oxygen (CO) WD TDE model of Rosswog et al. (2009), where thermonuclear explosions are ignited. They applied a radiative transfer simulation to the model in a post-process manner, and showed that the emission from thermonuclear explosions is indeed similar to SNe Ia. The CO WD TDE model does not exactly match with SNe Ia and there are some different points, such as relatively faint B-band magnitude than normal SNe Ia, different color evolutions, and the Doppler shift of spectral lines reflecting escape velocity of unbound debris from the IMBH. However, the variety of the observational signatures is still mysterious because they considered only one particular case of the CO WD TDE. It is not clear if other WD TDEs share the same properties shown in their model once other parameter sets are considered. As pointed out in Kawana et al. (2018), we can naively expect a large variety of observational signatures, and thus it is important to reveal the variety.

In this thesis, we study the variety and characteristics of observational signatures from thermonuclear explosions in WD TDEs. We consider 5 WD TDEs with different parameter sets. We perform hydrodynamic simulations, detailed nucleosynthesis simulations, and radiative transfer simulations for the models and thus derive synthetic observational signatures. We compare our models with observed transients, and search for WD TDE candidates. We also constrain properties of IMBHs by discussing possible WD TDE candidates found by the comparisons.

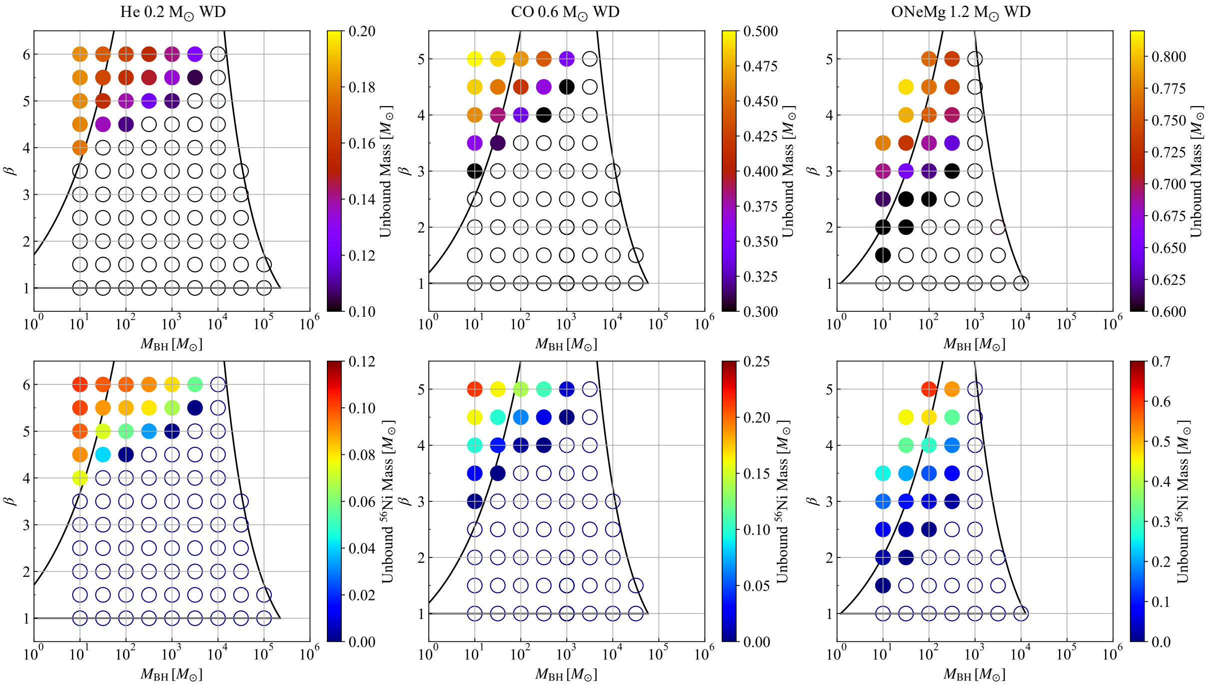

Figure 2.3: Masses of unbound debris and those of ^{56}Ni in the unbound debris. The figure is reproduced from Kawana et al. (2018). The solid curves show the boundaries where WD TDEs occur, which are also shown Figure 2.2. Note that the vertical axes are in linear scale here while are in logarithmic scale in Figure 2.2. From left to right, each column respectively shows the results for $M_{\rm WD} = 0.2$, 0.6, or $1.2\,{\rm M}_\odot$. The open circles show TDEs without explosive nuclear reactions. The filled circles show TDEs with explosive nuclear reactions.

Chapter 3

Methods

In this Chapter, we explain our numerical methods used to model observational signatures from thermonuclear explosions in WD TDEs. First, we show an overview of the methods and models of WD TDEs considered here. We combine three numerical simulations composed of hydrodynamic simulations, post-process detailed nucleosynthesis simulations, and radiative transfer simulations. Later, we describe each method in detail.

3.1 Overview

We consider 5 parameter sets of WD TDEs in order to study a variety of emission from thermonuclear explosions in WD TDEs, considering the WD mass as the main parameter to be varied. Table 3.1 shows the model parameters of our 5 models.

We combine three numerical simulations to derive synthetic observational signatures. First, we perform three-dimensional smoothed particle hydrodynamic (SPH) simulations coupled with simplified nuclear reaction networks. We follow dynamical evolution of the tidal disruption of a WD by a BH and thermonuclear explosions in the disruption phase, corresponding to the phases 1 to 4 in Figure 1.2 and to a timescale of $\sim$ 1000 s. We terminate the hydrodynamic simulations when homologous expansion of the unbound ejecta of the WD debris is approximately realized.

Second, we perform detailed nucleosynthesis simulations to derive detailed nuclear compositions of the unbound ejecta. This process is needed because the nuclear compositions derived by the simplified nuclear reaction networks adopted in the hydrodynamic simulations consider 13 isotopes from ^{4}He to ^{56}Ni, and are not enough for the following radiative transfer simulations. We record histories of density and temperature for all the SPH particles in the hydrodynamic simulations when explosive nuclear reactions occur, corresponding to a timescale of $\sim$ 1 s and to the phase 2 in Figure 1.2. Then we perform the nucleosynthesis simulations for all the SPH particles in a post-process manner with the density-temperature histories and with the initial nuclear compositions adopted in the hydrodynamic simulations, considering nuclear reaction networks among 640 isotopes.

Third, we perform three-dimensional, multi-frequency, and time-dependent Monte Carlo (MC) radiative transfer simulations to make synthetic observations of the emission from the unbound debris. In the simulations, we follow the generation of photons by the radioactive decays, interactions of the photons with the unbound debris, and escapes of the photons from the ejecta with the assumptions of the local thermal equilibrium (LTE) and the radiative equilibrium. The resultant optical radiation appears with a timescale of ~ 10 d, and thus it is computationally expensive to follow dynamical evolutions with the hydrodynamic simulations until that time. Thus we adopt distributions of the density and velocity of the unbound debris as those given by the hydrodynamic simulations at their ends, and use an approximation that the velocity of the unbound ejecta is constant after the ends, while its temperature evolution and the radioactive decays are followed. The approximation is valid because we followed the hydrodynamic simulations until the homologous expansion of the unbound ejecta is approximately realized, and the pressure gradient is too low to affect the kinetic profiles of the unbound ejecta in the timescale of concern in the radiative transfer simulations. We also adopt the nuclear compositions as those given by the detailed nucleosynthesis simulations. The computational domain is set such that its origin is at the center of mass (COM) of the ejecta, while we ignore the bound fallback debris. As the results of the radiative transfer simulations, we obtain a distribution of photons escaping from the system as a function of time, frequency, and a viewing angle.

3.2 Hydrodynamic Simulations

First, we perform SPH simulations coupled with simplified nuclear reactions to follow dynamical evolution of the tidal disruption and thermonuclear explosions in the disruption phase. We largely follow numerical methods adopted in Tanikawa et al. (2017) and Kawana et al. (2018). Basic equations solved in our SPH simulations are

$$\frac{\mathrm{d}\boldsymbol{v}}{\mathrm{d}t} = -\frac{\nabla P}{\rho} + \boldsymbol{g}_{\mathrm{BH}} + \boldsymbol{g}_{\mathrm{WD}}, \tag{3.1}$$

$$\frac{\mathrm{d}u}{\mathrm{d}t} = -\frac{P}{\rho}\nabla\cdot\boldsymbol{v} + \dot{\epsilon}_{\mathrm{nuc}}, \tag{3.2}$$

$$\frac{\mathrm{d}X_i}{\mathrm{d}t} = \dot{X}_i(\rho, u, \boldsymbol{X}), \tag{3.3}$$

where the equations respectively show the equation of motion, energy equation, and thermonuclear reactions. Table 3.2 shows the meanings of the physical values in the equations.

The SPH is the Lagrangian mesh-free particle method first developed in Lucy (1977). We model a WD as a collection of SPH particles and a BH as a single gravity source. We adopt a simple and basic SPH method (for a review see Rosswog, 2015). We use the Wendland C^2 kernel (Wendland, 1995; Dehnen & Aly, 2012) for the interpolation of SPH kernels. We introduce the artificial viscosity in order to capture discontinuities like shocks with the formulation of Monaghan (1997) and Morris & Monaghan (1997). We adopt the Balsara switch (Balsara, 1995) in order to suppress the artificial viscosity from shear motion. We use FDPS (Iwasawa et al., 2016a,b) and explicit AVX instructions

Table 3.1: Model parameters. The WD compositions are shown as mass fractions of elements. $t_{\mathrm{end,hydro}}$ is the termination time of a hydrodynamic simulation. $R_{\mathrm{max,rad}}$ is the radius of the outer edge of the radial grid used in a radiative transfer simulation at $t_{\mathrm{end,hydro}}$. $v_{\mathrm{r,max,rad}}$ is the corresponding radial velocity to $R_{\mathrm{max,rad}}$. $t_{\mathrm{init,rad}}$ is the initial time of a radiative transfer simulation since the tidal disruption.

M_{WD} [$\mathrm{M}_\odot$]	R_{WD} [10^8 cm]	WD composition	M_{BH} [$\mathrm{M}_\odot$]	β	$t_{\mathrm{end,hydro}}$ [s]	$R_{\mathrm{max,rad}}$ [10^{12} cm]	$v_{\mathrm{r,max,rad}}$ [$10^9\,\mathrm{cm\,s^{-1}}$]	$t_{\mathrm{init,rad}}$ [d]
0.2	12.8	^{4}He 100 %	$10^{2.5}$	5.0	2000	4.0	2.05	3.16
0.4	9.7	^{4}He 100 %	$10^{2.5}$	5.0	2000	5.0	2.52	3.16
0.6	7.5	^{12}C 50 %, ^{16}O 50 %	$10^{2.5}$	5.0	1000	1.7	1.77	1.58
1.0	5.0	^{12}C 50 %, ^{16}O 50 %	$10^{2.5}$	5.0	1000	4.0	3.97	1.58
1.2	3.4	^{12}C 50 %, ^{16}O 50 %	10^{2}	3.5	1000	3.6	3.61	1.58

Table 3.2: Meaning of physical values.

$\mathrm{d}/\mathrm{d}t$	Lagrangian time derivative. $\mathrm{d}/\mathrm{d}t = \partial/\partial t + \boldsymbol{v} \cdot \nabla$.
$\boldsymbol{v}$	Velocity vector.
ρ	Density.
P	Pressure.
$\boldsymbol{g}$	Gravity vector. Subscripts of 'BH' and 'WD' respectively mean the gravity by a BH and the self-gravity by a WD.
u	Specific internal energy density.
$\dot{\epsilon}_{\mathrm{nuc}}$	Specific energy generation rate given by nuclear reactions.
X_i	Mass fraction of an isotope specified with the subscript 'i'.
Y_i	Number fraction of an isotope specified with the subscript 'i'.

(Tanikawa et al., 2012, 2013) to perform efficient calculations on distributed-memory parallel supercomputers.

We use `Helmholtz` equation of state (EoS) for the WD (Timmes & Swesty, 2000). The EoS considers degenerate electron/positron gas as ideal Fermi gas, ion gas as an ideal gas with the adiabatic index $\gamma = 5/3$, thermal radiation, and Coulomb corrections. The SPH simulations are coupled with α-chain nuclear reaction networks (Timmes 1999; Timmes et al. 2000, see also Fryxell et al. 2000). The numerical methods to calculate the nuclear reactions are almost the same as those we describe in Section 3.3. A difference is that here we consider a smaller nuclear reaction networks among the 13 isotopes of ^{4}He, ^{12}C, ^{16}O, ^{20}Ne, ^{24}Mg, ^{28}Si, ^{32}S, ^{36}Ar, ^{40}Ca, ^{44}Ti, ^{48}Cr, ^{52}Fe, and ^{56}Ni. We integrate the nuclear reactions over time implicitly when $\rho > 5 \times 10^{7}$ g cm^{-3} and $T > 3 \times 10^{9}$ K, and otherwise explicitly. This is because an integration timestep in the explicit method should be very small ($\lesssim 10^{-12}$ s) in order to avoid the overcooling of photo-dissociation (Raskin et al., 2010). Adopting such a very small timestep would be computationally expensive, and thus we employ the implicit method in the phase space. Once the nuclear reactions are calculated, the energy generation rate is calculated as

$$\dot{\epsilon}_{\mathrm{nuc}} = N_{\mathrm{A}} \sum_{i} B_i \frac{\mathrm{d}Y_i}{\mathrm{d}t} - \dot{\epsilon}_{\nu} \tag{3.4}$$

where N_{A} is the Avogadro constant, B_i is the specific binding energy, and $\dot{\epsilon}_{\nu}$ is the energy loss rate due to free escapes of neutrinos given by Itoh et al. (1996). In order to calculate the `Helmholtz` EoS and nuclear reactions, we use the routines developed by the Center for Astrophysical Thermonuclear Flashes at the University of Chicago (Fryxell et al., 2000).

We use the gravitational potential of Tejeda & Rosswog (2013) to include an approximate general relativistic correction for the non-rotating, Schwarzschild BH. The potential uses the approximation that the specific orbital energy of a point mass particle ϵ is close to c^2, or $|\epsilon - c^2| \ll c^2$. The approximation is valid for parabolic orbits on which most TDEs are (see Section 2.1.3), and then the potential gives the BH gravity in the spherical coordinate $(r,\, \theta,\, \phi)$ as

$$\ddot{r} = -\frac{GM_{\mathrm{BH}}}{r^2}\left(1-\frac{R_S}{r}\right)^2 + \left(1-\frac{R_S}{r}\right)^{-1}\frac{\dot{r}^2}{r} + \left(r-\frac{3}{2}R_S\right)(\dot{\theta}^2+\sin^2\dot{\phi}^2), \tag{3.5}$$

$$\ddot{\theta} = -\frac{2\dot{r}\dot{\phi}}{r}\left(\frac{r-3R_S/2}{r-R_S}\right) + \sin\theta\cos\theta\dot{\phi}^2, \tag{3.6}$$

$$\ddot{\phi} = -\frac{2\dot{r}\dot{\phi}}{r}\left(\frac{r-3R_S/2}{r-R_S}\right) - 2\cot\theta\dot{\phi}\dot{\theta}, \tag{3.7}$$

where R_S is the Schwarzschild radius. We eliminate SPH particles when a distance between an SPH particle and the center of the BH is shorter than the sum of the kernel support radius of the SPH particle and the Schwarzschild radius. We calculate the self-gravity of the WD with adaptive gravitational softening (Monaghan, 1997).

The initial conditions are set as follows. First, we distribute and relax SPH particles to represent a WD with a uniform temperature of $T = 10^5$ K and uniform nuclear composition shown in Table 3.1, in the same manner as in Tanikawa et al. (2015) and Sato et al. (2015, 2016). Second, to simulate a TDE, we uniformly add displacement and velocity to the WD such that the orbit is parabolic in the Schwarzschild metric. The initial separation between the BH and WD is $5R_t$. We assume that the WD has no spin. We terminate the simulations at the time $t_{\mathrm{end,hydro}}$ shown in Table 3.1.

We employ 786,432 SPH particles to represent the WD. The resolution is not enough to resolve shock structure during the tidal compression, and thus the nucleosynthetic results are resolution-dependent (Tanikawa et al., 2017). Tanikawa et al. (2017) shows that synthesized masses of intermediate mass elements (IMEs) and iron group elements (IGEs) vary up to a factor of several if the number of SPH particles are changed by a factor of about 1000. Thus, the resultant thermonuclear emission of our models, such as the luminosity and timescale, would quantitatively change by the numerical resolution. However, we expect that the results do not change qualitatively. A reason is that detonations in WD TDEs are also reproduced in Tanikawa (2018b) and Anninos et al. (2018), who adopt independent numerical methods with ours. Another reason is that we also see rough matches in nucleosynthetic yields between our hydrodynamic simulations (see Kawana et al. 2018) and Anninos et al. (2018). Furthermore, we expect a large variety of thermonuclear emission from WD TDEs for other parameter cases. Even if our nucleosynthetic results are not exactly correct, similar nucleosynthesis and succeeding thermonuclear emission would be given for other parameter cases.

3.3 Detailed Nucleosynthesis Simulations

In order to derive detailed nuclear compositions, we perform detailed nucleosynthesis simulations with the `torch` code[1] (Timmes, 1999). We record histories of density and temperature for all the SPH particles in the hydrodynamic simulations during phases when explosive nuclear reactions occur. Then we perform the nucleosynthesis simulations

---

[1] `http://cococubed.asu.edu/`

for all the particles in a post-process manner with the density-temperature histories, considering networks among 640 isotopes. For the simulations, we take the same initial nuclear compositions as those used in the SPH simulations.

The basic equations solved in the nucleosynthesis simulations are the following set of the ordinary differential equations (ODEs)

$$\dot{\boldsymbol{Y}} = J(\rho, u)\boldsymbol{Y}, \tag{3.8}$$

where $\boldsymbol{Y} = \{Y_i\}$ is the nuclear composition of isotopes, and $J(\rho, u)$ is the Jacobian matrix describing reaction rates between two isotopes. The entries of the Jacobian matrix are determined as follows. If we consider an example of the $^{12}\mathrm{C}(\alpha,\gamma)^{16}\mathrm{O}$ reaction, the reaction contributes to change the abundance of each elements as

$$\dot{Y}(^4\mathrm{He}) = -Y(^4\mathrm{He})Y(^{12}\mathrm{C})\lambda + \cdots\,, \tag{3.9}$$

$$\dot{Y}(^{12}\mathrm{C}) = -Y(^4\mathrm{He})Y(^{12}\mathrm{C})\lambda + \cdots\,, \tag{3.10}$$

$$\dot{Y}(^{16}\mathrm{O}) = +Y(^4\mathrm{He})Y(^{12}\mathrm{C})\lambda + \cdots\,, \tag{3.11}$$

where $\lambda = \lambda(\rho, u)$ is the reaction rate. The ellipses show contributions from other reactions. The negative signs shown in the first term of the right hand side mean the decrease of ^{4}He and ^{12}C with the reaction , while the positive sign means the increase of ^{16}O. These equations contribute to the Jacobian matrix J as

$$J(^4\mathrm{He},^4\mathrm{He}) = -Y(^{12}\mathrm{C})\lambda + \cdots\,, \qquad J(^4\mathrm{He},^{12}\mathrm{C}) = -Y(^4\mathrm{He})\lambda + \cdots\,, \tag{3.12}$$

$$J(^{12}\mathrm{C},^4\mathrm{He}) = -Y(^{12}\mathrm{C})\lambda + \cdots\,, \qquad J(^{12}\mathrm{C},^{12}\mathrm{C}) = -Y(^4\mathrm{He})\lambda + \cdots\,, \tag{3.13}$$

$$J(^{16}\mathrm{O},^4\mathrm{He}) = -Y(^{12}\mathrm{C})\lambda + \cdots\,, \qquad J(^{16}\mathrm{O},^{12}\mathrm{C}) = -Y(^4\mathrm{He})\lambda + \cdots\,, \tag{3.14}$$

Repeating the same procedure for all the reactions considered, we can compose the Jacobian matrix.

In principle, every isotope can react with any other isotope, and thus the Jacobian matrix has non-zero values for its all entries. However, it is computationally less expensive to ignore reactions with sufficiently low reaction rates. For the reactions among 640 isotopes, most reactions considered are the types of (n,p), (n,γ), (α,p), (α,γ), (α,n), (p,γ), and their inverses (p,n), (γ,n), (p,α), (γ,α), (n,α), (γ,p). Some other special reactions such as the triple-α reaction and $^{12}\mathrm{C}+^{12}\mathrm{C}$ reaction are also considered. The reaction rates are based on Woosley & Hoffman (1992) and Woosley & Weaver (1995).

For the reactions among 13 isotopes, adopted in the hydrodynamic simulations, the following reactions are considered:

- The (α,γ) and (γ,α) reactions from ^{12}C to ^{56}Ni
- The triple-α reaction: $^4\mathrm{He}(\alpha\alpha,\gamma)^{12}\mathrm{C}$
- $^{12}\mathrm{C}(^{12}\mathrm{C},\gamma)^{24}\mathrm{Mg}$
- $^{12}\mathrm{C}(^{16}\mathrm{O},\gamma)^{28}\mathrm{Si}$

- ^{16}O(^{16}O$, \gamma)^{24}$S
- The $(\alpha, p)(p, \gamma)$ and $(\gamma, p)(p, \alpha)$ reactions with the intermediate isotopes of ^{27}Al, ^{31}P, ^{35}Cl, ^{39}K, ^{43}Sc, ^{47}V, ^{51}Mn, and ^{55}Co. The intermediate isotopes are assumed to be consumed immediately and thus are not followed.

The reaction rates are set by hand to obtain an accurate energy generation rate with such a small reaction network (Timmes 1999; Timmes et al. 2000, which are also based on Caughlan & Fowler 1988). Note that the derived nuclear compositions are also accurate to some extent (for example see Figure 4.7).

Because of the way to compose the Jacobian matrices, they are sparse, or most entries of the matrices are zero. Focusing on this nature, the `torch` code uses the MA28 sparse matrix package (Duff et al., 1986) to solve linear algebra, which enables to obtain a good balance between the accuracy and computational costs such as the execution speed and storage amount.

Then the `torch` code integrates Equation (3.8) for a given timestep. When we integrate the equations in the hydrodynamic simulations, we consider hydrostatic evolution, i.e. the density and temperature do not change for a given timestep of the hydrodynamic simulations. When we calculate the post-process nuclear reactions, we extract density and temperature at a given time from their histories recorded in the hydrodynamic simulations and integrate the equations for the time when explosive thermonuclear occur. However, it is not straightforward to accurately integrate the ODEs if the given timesteps are not sufficiently small compared with the timescale for abundance, density, or temperature to change significantly.

The `torch` code handles the problem by adopting the variable-order Bader-Deuflhard method (e.g. Bader & Deuflhard, 1983; Press et al., 1996), a semi-implicit integration method. The method is described as follows. For a given large timestep H where the abundance evolves from $\boldsymbol{Y}_n$ to $\boldsymbol{Y}_{n+1}$, we divide the large timestep into m small timesteps H/m, and first solve the following matrix equations:

$$h = H/m, \tag{3.15}$$

$$(1/h - J) \cdot \boldsymbol{\Delta}_0 = J \cdot \boldsymbol{Y}_n, \tag{3.16}$$

$$\boldsymbol{Y}_1 = \boldsymbol{Y}_n + \boldsymbol{\Delta}_0. \tag{3.17}$$

Then, we solve the following equations from $k = 1, 2, \cdots, m-1$,

$$(1/h - J) \cdot \boldsymbol{x} = J \cdot \boldsymbol{Y}_k - \boldsymbol{\Delta}_{k-1}, \tag{3.18}$$

$$\boldsymbol{\Delta}_k = \boldsymbol{\Delta}_{k-1} + 2\boldsymbol{x}, \tag{3.19}$$

$$\boldsymbol{Y}_{k+1} = \boldsymbol{Y}_k + \boldsymbol{\Delta}_k. \tag{3.20}$$

In the last step, we obtain the following closure for $\boldsymbol{Y}_{n+1}$ as

$$(1/h - J) \cdot \boldsymbol{\Delta}_m = J \cdot \boldsymbol{Y}_m - \boldsymbol{\Delta}_{m-1}, \tag{3.21}$$

$$\boldsymbol{Y}_{n+1} = \boldsymbol{Y}_m + \boldsymbol{\Delta}_m. \tag{3.22}$$

These procedures are executed at least twice with $m = 2$ and $m = 6$, yielding a 5th-order method at least, and may be executed at a maximum of 7 times, yielding a 15th-order method. The times of the executions of the procedures are determined by the required accuracy of 10^{-6} and the smoothness of the solution. The accuracy of an integration step is estimated by comparing the solutions derived with different orders.

3.4 Radiative Transfer Simulations

Finally, we perform three-dimensional, multi-frequency, and time-dependent MC radiative transfer simulation simulations using `HEIMDALL` (Maeda, 2006; Maeda et al., 2014). In the simulations, the unbound ejecta is approximated as its velocity is constant, while we follow time evolution of its temperature, ionization, and opacity, and the radioactive decays of ^{48}Cr/V/Ti, ^{52}Fe/Mn/Cr, and ^{56}Ni/Co/Fe as the power sources. For stable elements, we consider them with atomic numbers Z from 1 to 30, and their abundance is extracted from the detailed nucleosynthesis simulations. The computational domain is set such that its origin is at the center of mass (COM) of the ejecta with the three-dimensional spherical grid of $(v_r, \cos\theta, \phi)$, while we ignore the bound fallback debris. The three-dimensional spherical grid is equally sampled with bins of $(100, 50, 50)$, where the outer edge of the radial grid and the corresponding radius are taken as shown in Table 3.1. As a preparation for the radiative transfer simulations, we map the distribution of the density and velocity given by the hydrodynamic simulations, and the nuclear compositions given by the detailed nucleosynthesis simulations to the spherical grid following the prescription given by Röttgers & Arth (2018). With the method of Röttgers & Arth (2018), we can well conserve integral fluid properties and can maintain the resolution of the SPH data. We take time bins logarithmically sampled with the width of 0.02 dex, and with the initial times shown in Table 3.1. The frequency bins range from 100 Å to 20,000 Å and are logarithmically sampled with 3,000 bins.

The methods of our radiative transfer simulations largely follow the MC methods formalized in Lucy (2005), Kasen et al. (2006) and Kromer & Sim (2009). The input variables for the simulations are the distribution of the kinetic and nuclear compositions $[\boldsymbol{v}(\boldsymbol{r},t), \rho(\boldsymbol{r},t), \boldsymbol{X}(\boldsymbol{r},t)]$. With the inputs, we iteratively calculate the thermal and ionization structure with the assumptions of the LTE and radiative equilibrium, and accordingly the opacity distribution, or $\left[T(\boldsymbol{r},t), n_i^j(\boldsymbol{r},t), \alpha(\boldsymbol{r},\lambda,t)\right]$. Here n_i^j is the number density of an ion j at i-th level. We simultaneously simulate the generation and propagation of photons consistently with the above calculations, and thus obtain the radiation field $[f(\boldsymbol{r},\lambda,\boldsymbol{l},t)]$, where $\boldsymbol{l}$ is the photon direction vector. The calculations performed can be categorized into 5 steps. We describe each step in the following Sections.

3.4.1 Distribution of Initial Photon Packets

In our MC radiative transfer simulations, we simulate the generation and propagation of a collection of photon packets. Each photon packet is described by $[\boldsymbol{r}(t), \lambda(t), \boldsymbol{l}(t), \epsilon(t)]$, where ϵ is the total energy within the packet. The photon packet has a unique frequency

ν, and thus the total energy can be expressed as $\epsilon = n_{\rm ph} h\nu$ with the photon number $n_{\rm ph}$.

We first specify the generation of the photon packets rather than reprocessing of already existing thermal photons. We consider the radioactive decays of ^{48}Cr/V/Ti, ^{52}Fe/Mn/Cr, and ^{56}Ni/Co/Fe as the photon generation processes. We ignore the internal energy given by the hydrodynamic simulations because the adiabatic expansion makes it much smaller than the radioactive energy at the timescale of our interest here. The photon packets are randomly generated with probabilities determined by the spatial distribution of the radioactive nuclei and the properties of the radioactive decays, where we take into account the branching ratios and decay time of them. The radioactive decays produce positrons and $\gamma-$ray. We assume that the positrons deposit their energy in situ due to their short mean free path. $\gamma-$ray packets generated before the initial time of the relative transfer simulations, shown in Table 3.1, are also assumed to be absorbed in situ due to high optical depth in the early phase. The deposited energy is converted to thermal photons at the initial time of the radiative transfer simulations. We consider the loss of the thermal energy due to the adiabatic expansion between the deposition time and the initial time. For $\gamma-$ray packets generated after the initial time, transfer of them are solved with the MC scheme identical to thermal photons but without temperature iteration, explained in the following Sections. This is because the cross sections of the interactions of $\gamma-$rays with matters, as described below, are insensitive to the thermal condition (Maeda, 2006). We take into account Compton scattering, pair creation, and photoelectric absorption as interactions of the $\gamma-$rays with matters. We use the Klein-Nishina cross section for the cross sections of the Compton scattering. the cross sections for the pair creation and photoelectric absorption are adopted from Hubbell (1969) (see also Ambwani & Sutherland, 1988) and are compiled by Hoeflich et al. (1992) from Veigele (1973), respectively.

By solving the MC transfer of $\gamma-$rays, we obtain the spatial distribution of the energy deposition in a timestep by $\gamma-$rays and positrons $\Gamma_\gamma(\boldsymbol{r}, t)$. We randomly generate thermal photon packets with their distribution consistent with $\Gamma_\gamma(\boldsymbol{r}, t)$. We set the energy content of each photon packet to be the same at its creation, and its direction vector is randomly determined with the isotropic distribution in the comoving frame. To determine the probability distribution of the wavelength of the thermal photon packet, we need to know the matter temperature. As a first step, we use a given temperature $T_0(\boldsymbol{r}, t)$ to determine the wavelength, but later we iterate the MC radiative transfer and the temperature determination to obtain their consistency, as described in the following Sections.

3.4.2 Thermal and Ionization Structure and Opacity Distributions

In order to simulate interactions of the photon packets with matters, we need to know the spatial distribution of opacities of the interactions for a given timestep. We take into account the interactions of thermal photons with matters including bound-bound, bound-free, free-free, and electron scattering. At a given time and for a given temperature $T(\boldsymbol{r}, t)$, we compute the ionization and level populations of ions with the Saha equation, and the Boltzmann distribution for electrons under the LTE assumption.

The electron scattering opacity is

$$\alpha_{\mathrm{e}}(\boldsymbol{r},t) = \sigma_{\mathrm{T}} n_{\mathrm{e}}(\boldsymbol{r},t), \tag{3.23}$$

where σ_{T} is the Thomson cross section, and $n_{\mathrm{e}}(\boldsymbol{r},t)$ is the electron number density given by the ionization condition. The free-free absorption opacity is

$$\alpha_{\mathrm{ff}}(\boldsymbol{r},\nu,t) = \frac{4e^6}{3m_{\mathrm{e}}hc}\left(\frac{2\pi}{3km_{\mathrm{e}}}\right)^{1/2} T(\boldsymbol{r},t)^{-1/2}\sum_j Z_j^2 n_{\mathrm{e}} n^j \nu^{-3}\left[1-\exp\left(\frac{h\nu}{kT}\right)\right] g_{\mathrm{ff}}, \tag{3.24}$$

where e is the elementary charge, m_{e} is the electron mass, h is the Planck constant, k is the Boltzmann constant, ν is the photon frequency, Z_j is the number of free electrons associated with the ion j , and n^j is the number density of the ion j. We take the Gaunt factor g_{ff} as unity. We take the cross sections of the bound-free transitions $[\alpha_{\mathrm{bf}}(\boldsymbol{r},\lambda,t)]$ from Verner & Yakovlev (1995) and Verner et al. (1996). For a given λ, we take the sum of the bound-free cross sections over different ions with the ionization states calculated with the Saha equation.

We adopt the Sobolev approximation for the bound-bound transitions, where the line optical depth is given as

$$\tau_{lu}(\boldsymbol{r},t) = \frac{\pi e^2}{m_{\mathrm{e}}c} f_{lu}\lambda_{lu} t n_l(\boldsymbol{r},t)\left[1-\frac{g_l n_u(\boldsymbol{r},t)}{g_u n_l(\boldsymbol{r},t)}\right], \tag{3.25}$$

where the subscripts l and u are the lower and upper levels of a transition, respectively. We omit the superscript j to denote the ion here. f_{lu} is the oscillator strength of the transition, and λ_{lu} is the wavelength of it. g_l and g_u are respectively statistical weights of the lower and upper levels. We use a set of $\simeq 5\times10^5$ bound-bound transitions from Kurucz & Bell (1995).

The probability for the photon to escape out of the resonance region is calculated with the Sobolev optical depth as

$$\beta_{lu}(\boldsymbol{r},t) = \frac{1-e^{-\tau_{lu}(\boldsymbol{r},t)}}{\tau_{lu}(\boldsymbol{r},t)} . \tag{3.26}$$

We use the expansion opacity formalism to treat the bound-bound transitions, where the transitions with similar wavelengths are combined into a discrete frequency grid (Karp et al., 1977; Eastman & Pinto, 1993). Then the total cross section of the bound-bound interaction is

$$\alpha_{\mathrm{bb}}(\boldsymbol{r},\lambda,t) = \frac{1}{ct}\sum_{l,u}\frac{\lambda_{lu}}{\Delta\lambda}(1-e^{-\tau_{lu}}) , \tag{3.27}$$

where the sum runs over the transitions whose energy difference is within the wavelength bin considered $(\Delta\lambda)$. The absorptive component in the opacity is defined within the two-level atom approximation, or,

$$S_\lambda = (1-\epsilon_{lu})J_\lambda + \epsilon_{lu}B_\lambda(T) , \tag{3.28}$$

where S_λ is the source function. The first term on the right hand side of the equation means the scattering component, while the second term means the absorptive component. ϵ_{lu} is the parameter meaning fraction of absorptive component, and we take the same value of ϵ_{lu} for all the transitions, or $\epsilon \equiv \epsilon_{lu} = 0.3$, following Kasen et al. (2006). Then, the absorptive opacity of the bound-bound transitions is

$$\alpha_{\mathrm{bb,abs}}(\boldsymbol{r}, \lambda, t) = \frac{1}{ct} \sum_{l,u} \frac{\lambda_{lu}}{\Delta\lambda} \frac{\epsilon_{lu}}{\beta_{lu} + \epsilon_{lu}(1-\beta_{lu})} (1 - e^{-\tau_{lu}}) \ . \tag{3.29}$$

Finally, the total opacity is given as

$$\alpha(\boldsymbol{r}, \lambda, t) = \alpha_{\mathrm{e}}(\boldsymbol{r}, t) + \alpha_{\mathrm{ff}}(\boldsymbol{r}, \lambda, t) + \alpha_{\mathrm{bf}}(\boldsymbol{r}, \lambda, t) + \alpha_{\mathrm{bb}}(\boldsymbol{r}, \lambda, t) \ , \tag{3.30}$$

while the absorptive component is defined as

$$\alpha_{\mathrm{abs}}(\boldsymbol{r}, \lambda, t) = \alpha_{\mathrm{ff}}(\boldsymbol{r}, \lambda, t) + \alpha_{\mathrm{bf}}(\boldsymbol{r}, \lambda, t) + \alpha_{\mathrm{bb,abs}}(\boldsymbol{r}, \lambda, t) \ . \tag{3.31}$$

Note that we ignore excitations and ionization of atoms by non-thermal photons because of the LTE assumption. The point results in failing to excite neutral helium, and thus helium lines are always missed in our radiative transfer simulations (Harkness et al., 1987; Lucy, 1991; Hachinger et al., 2012).

3.4.3 Propagation of Photon Packets

With the interaction opacities derived in Section 3.4.2, we simulate propagation of the photon packets in the MC manner. When we consider a time bin from t_n to t_{n+1}, we simulate the photon packets generated in the time bin by the $\gamma-$ray and positron energy deposition and those which already exist at t_n from the previous timestep. The photon packets are followed until t_{n+1} or until they escape out the computational domain.

During the timestep between t_n and t_{n+1}, propagation paths of photon packets are divided into step(s). At each step, we calculate photon path lengths for some numerical and physical events, and then the event with the minimal length is adopted to occur. These events are composed of the following 4 events: (1) A photon packet reaches a boundary of the current spatial mesh, (2) The time reaches to the next timestep t_{n+1}, (3) The frequency of the photon packet in the comoving frame is shifted into a different frequency bin due to the Doppler shift $\Delta\lambda = \lambda v/c$, and (4) A photon packet experiences either scattering or absorption.

We evaluate the item (4) with the following MC formula as

$$\alpha'(\boldsymbol{r}, \lambda, t)\rho(\boldsymbol{r}, t)\delta s' = -\ln z \ , \tag{3.32}$$

where z is the random number with a uniform probability distribution between 0 and 1, and δs is the path length. The prime means that the quantities are those in the rest-frame. Whether the packet interacting with matters experiences absorption or scattering is randomly determined, while their probability ratio is determined by the ratio of $\alpha_{\mathrm{abs}}(\boldsymbol{r}, \lambda, t)$ and $\alpha_{\mathrm{scat}} \equiv \alpha(\boldsymbol{r}, \lambda, t) - \alpha_{\mathrm{abs}}(\boldsymbol{r}, \lambda, t)$.

We treat a scattering event as isotropic and elastic in the comoving frame. A new photon direction is randomly chosen in the comoving frame and is converted to the rest frame. We treat an absorption and re-emission event with the LTE assumption, and thus we determine a new wavelength at its re-emission by the local thermal emissivity as

$$j_\lambda(\boldsymbol{r}, t) = B_\lambda(T)\alpha_{\mathrm{abs}}(\boldsymbol{r}, \lambda, t) \ . \tag{3.33}$$

We also treat the re-emission as isotropic in the comoving frame.

3.4.4 Determination of New Temperature and Iteration until Temperature Converges

By simulating the photon propagation, we obtain the heating rate between t_n to t_{n+1} by the thermal photons as

$$\Gamma_{\mathrm{opt}}(\boldsymbol{r}, t) = \frac{1}{\Delta t V}\sum_k \alpha_{\mathrm{abs}}(\boldsymbol{r}, \lambda, t)\varepsilon_k \delta s_k \ , \tag{3.34}$$

where $\Delta t \equiv t_{n+1} - t_n$, and V is the volume of the spatial mesh. The quantities are those in the comoving frame. The sum runs over all the photon packets, denoted by k, which pass through a given mesh between t_n and t_{n+1}.

We also obtain the heating rate by γ-rays and positrons Γ_γ in the same manner. Then the radiative equilibrium gives the new temperature by the following balance between heating and cooling:

$$\Lambda(\boldsymbol{r}, T) = \Gamma_{\mathrm{opt}}(\boldsymbol{r}, t) + \Gamma_\gamma(\boldsymbol{r}, t) \ , \tag{3.35}$$

where the cooling rate at each spatial mesh $\Lambda(\boldsymbol{r}, T)$ is

$$\Lambda(\boldsymbol{r}, T) = 4\pi \int \alpha_{\mathrm{abs}}(\boldsymbol{r}, \lambda, T) B_\lambda(T) \mathrm{d}\lambda \ . \tag{3.36}$$

Here we adopt the absorptive opacity $\alpha_{\mathrm{abs}}(\boldsymbol{r}, \lambda, T)$ estimated with the previous temperature.

Generally, the new and previous temperature does not exactly match. Thus we iterate the 3 steps described in Section 3.4.2 to Section 3.4.4 for a given timestep between t_n and t_{n+1} until the temperature simultaneously converges at all the meshes. Once the convergence is realized, we end the calculations for the timestep. The converged temperature is then used as the initial guess for the temperature in the next timestep. The photon packets remaining in the system at t_{n+1} are also used as the initial condition of the next timestep. Repeating the procedures for the timesteps $\{t_n\}$, we obtain the time evolving radiation field and thermal structure of matters self-consistently.

3.4.5 Synthetic Observations

Simulating the procedures described in Section 3.4.1 to Section 3.4.4, we obtain photon packets escaping the computational domain. Such photon packets are recorded with their profiles $[f(\boldsymbol{l}, \lambda, t)]$, or the flux as a function of the viewing angle, wavelength, and time. We can make synthetic observations of the system with the accumulated photon packets. We can directly extract spectra as a function of time and the viewing angle by binning them. To calculate band magnitudes, we convolve the spectra to filter response functions. Because the computational domains in the radiative transfer simulations are the comoving frames with respect to the unbound ejecta, we finally correct the photon packets for the Doppler shift for each viewing angle when we are interested in the observer frame, or the BH rest frame.

Chapter 4

Results

In this Chapter, we show results of our numerical simulations. First, we show an overview of the results of all of our models. We summarize the results of the hydrodynamic simulations and detailed nucleosynthesis simulations. Second, we describe photometric characteristics of our models comparing them with observed transients. We select observed transients that show similar photometric characteristics as possible observed candidates of our models, and summarize comparisons between the selected transients and our models. Later, we explain each model. Taking the 0.2 $M_\odot$ model as a representative of our models, we explain important features of observational signatures of our WD TDE models in detail. We briefly describe the other models focusing on their differences and their effects on the observational signatures.

4.1 Overview of All the Models

Table 4.1 shows the result summary of the hydrodynamic and detailed nucleosynthetic simulations of all the models. All the models show thermonuclear explosions of a WD, which affect hydrodynamic profiles of WD debris, and a certain amount of heavier nuclei are synthesized. Figure 4.1 shows snapshots of the hydrodynamic simulation of the 0.2 $M_\odot$ model, as an example of a sequence of the tidal disruption, thermonuclear explosions, fallback of the bound debris, and escape of the unbound debris. The sequence corresponds to the phases 2 to 4 in Figure 1.2.

The unbound masses are larger than half of the initial WD masses because a part of released nuclear energy is converted into orbital energy of the debris. The unbound ejecta has a bulk motion escaping from the IMBH with the bulk velocity, and also expands with its kinetic energy $E_{\rm kin}$ (see also the spatial distribution of the debris shown in Figure 4.6, for example). The thermonuclear reactions synthesize a large amount of unbound ^{56}Ni, ranging from 15% to 60% of the initial WD masses. A part of a WD is not burnt by the thermonuclear reactions, and thus a good fraction of the element(s) composing the initial WD remain even after the tidal disruption. This point results in the large masses of He in the 0.2 and 0.4 $M_\odot$ models and of C and O in the 0.6, 1.0, and 1.2 $M_\odot$ models.

Figure 4.2 shows photometric properties of our models in a phase space of decay

Table 4.1: Result summary of hydrodynamic simulations and nucleosynthesis simulations. M_{unbound} is the mass of the unbound ejecta. E_{kin} is the kinetic energy of the unbound ejecta with respect to its center of mass (COM). The bulk velocity is the velocity of the COM with respect to the BH. M_{He}, M_{C}, M_{O}, M_{Si}, M_{Ca}, M_{56Ni} are respectively the masses of He, C, O, Si, Ca and ^{56}Ni in the unbound ejecta.

M_{WD} [$\mathrm{M}_\odot$]	M_{unbound} [$\mathrm{M}_\odot$]	E_{kin} [10^{50} erg]	bulk velocity [10^9 cm s^{-1}]	M_{He} [$\mathrm{M}_\odot$]	M_{C} [$\mathrm{M}_\odot$]	M_{O} [$\mathrm{M}_\odot$]	M_{Si} [$\mathrm{M}_\odot$]	M_{Ca} [$\mathrm{M}_\odot$]	M_{56Ni} [$\mathrm{M}_\odot$]
0.2	0.120	0.88	1.17	0.076	9.8×10^{-4}	4.0×10^{-6}	7.0×10^{-4}	0.0014	0.030
0.4	0.314	2.90	1.71	0.059	4.0×10^{-4}	5.2×10^{-6}	4.1×10^{-4}	0.0011	0.23
0.6	0.440	1.14	1.09	0.0020	0.11	0.13	0.038	0.0046	0.12
1.0	0.652	5.81	1.64	0.017	0.040	0.044	0.013	0.0020	0.49
1.2	0.775	4.14	1.34	0.0088	0.23	0.23	0.0040	6.2×10^{-4}	0.27

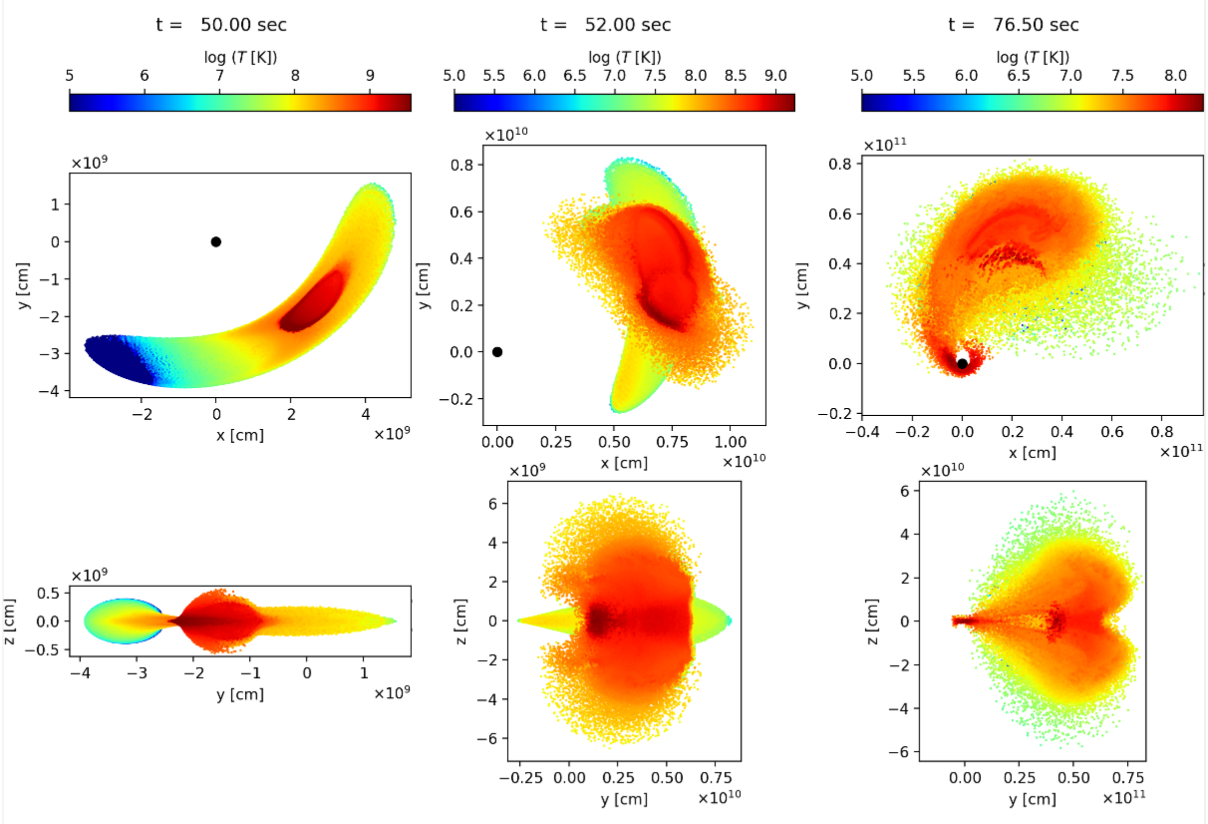

Figure 4.1: Snapshots of the hydrodynamic simulation of the 0.2 $M_\odot$ model. From left to right, we respectively show temperature distributions at 50, 52, and 76.5 s after the beginning of the hydrodynamic simulation. The orbit is in the xy-plane, and the top panels show face-on views, where the black points show the locations of the BH. The bottom panels show edge-on views, where the tidal compression along the z-axis and thermonuclear explosions are clearly seen at $t = 50$ s. $t = 50$, 52, and 76.5 s correspond to the phases 2, 3, and 4 in Figure 1.2, respectively.

timescale and peak bolometric luminosity. The 0.2 $M_\odot$ model exceptionally locates in the phase space where its peak luminosity is relatively faint ($\simeq 10^{42}\,\mathrm{erg\,s^{-1}}$) and the light curve rapidly decays (decay timescale of $\simeq$ 5-10 d). In these senses, the 0.2 $M_\odot$ model is similar to calcium-rich transients and .Ia SNe. The other models are in the phase spaces close to SNe Ia and fast decliners. Figure 4.3 shows other photometric properties of our models in a phase space of decay timescale in B-band $\Delta m_{15}(B)$ and the absolute peak B-band magnitude $M_{\rm peak}(B)$. The phase space is conventionally used to discuss the universality in SNe Ia (e.g. the Phillips relation: Phillips, 1993). Figure 4.3 also shows the phase spaces of observed thermonuclear transients, including normal SNe Ia and peculiar subclasses of them. The 0.2 $M_\odot$ model does not match with any observed thermonuclear transients in the phase space: the model shows faster decay in B-band than all the classes of observed thermonuclear transients. The other models show similar $\Delta m_{15}(B)$ and $M_{\rm peak}(B)$ to some classes of observed thermonuclear transients. In the phase space, the 0.4 $M_\odot$ model is close to fast decliners, while the 0.6, 1.0, and 1.2 $M_\odot$ models are close to normal SNe Ia, 02es-like SNe, 91bg-like SNe, 91T-like SNe, and SNe Iax (or 2002cx-like SNe Ia).

4.2 Comparisons of Our Models with Observed Transients Compared

The comparisons of photometric properties between our models and observed transients shown in Figure 4.2 and Figure 4.3 motivate us to select observed transients close to our models in the phase spaces as possible observed candidates of WD TDEs. For the 0.2 $M_\odot$ model, we select calcium-rich transients (Perets et al., 2010; Kasliwal et al., 2012; Valenti et al., 2014; Lunnan et al., 2017; Milisavljevic et al., 2017; De et al., 2018b), observed candidates of .Ia SNe (Kasliwal et al., 2010), and other transients showing rapid evolutions in their light curves (Drout et al., 2013, 2014; De et al., 2018a; Pursiainen et al., 2018). We compare the 0.2 $M_\odot$ model with the observed transients in detail in Section 4.3.

To compare with the other 0.4, 0.6, 1.0, and 1.2 $M_\odot$ models, we select representatives of the subclasses of the observed thermonuclear transients as shown in Table 4.2. We list photometric characteristics of the subclasses of thermonuclear transients as differences from normal SNe Ia as follows (see reviews Jha, 2017; Taubenberger, 2017, and references therein):

- 02es-like SNe show faint but slowly declining light curves.
- SN2006bt is the only exception in the 02es-like SNe. It is almost as luminous as normal SNe Ia with $M_{\rm peak}(B) \simeq 19$ mag with a similar $\Delta m_{15}(B) \simeq 1.1$ to the other 02es-like SNe.
- 91bg-like SNe show fainter, faster, and cooler light curves than normal SNe Ia.
- 91T-like SNe show higher peak luminosity and broader light curves than normal SNe Ia.

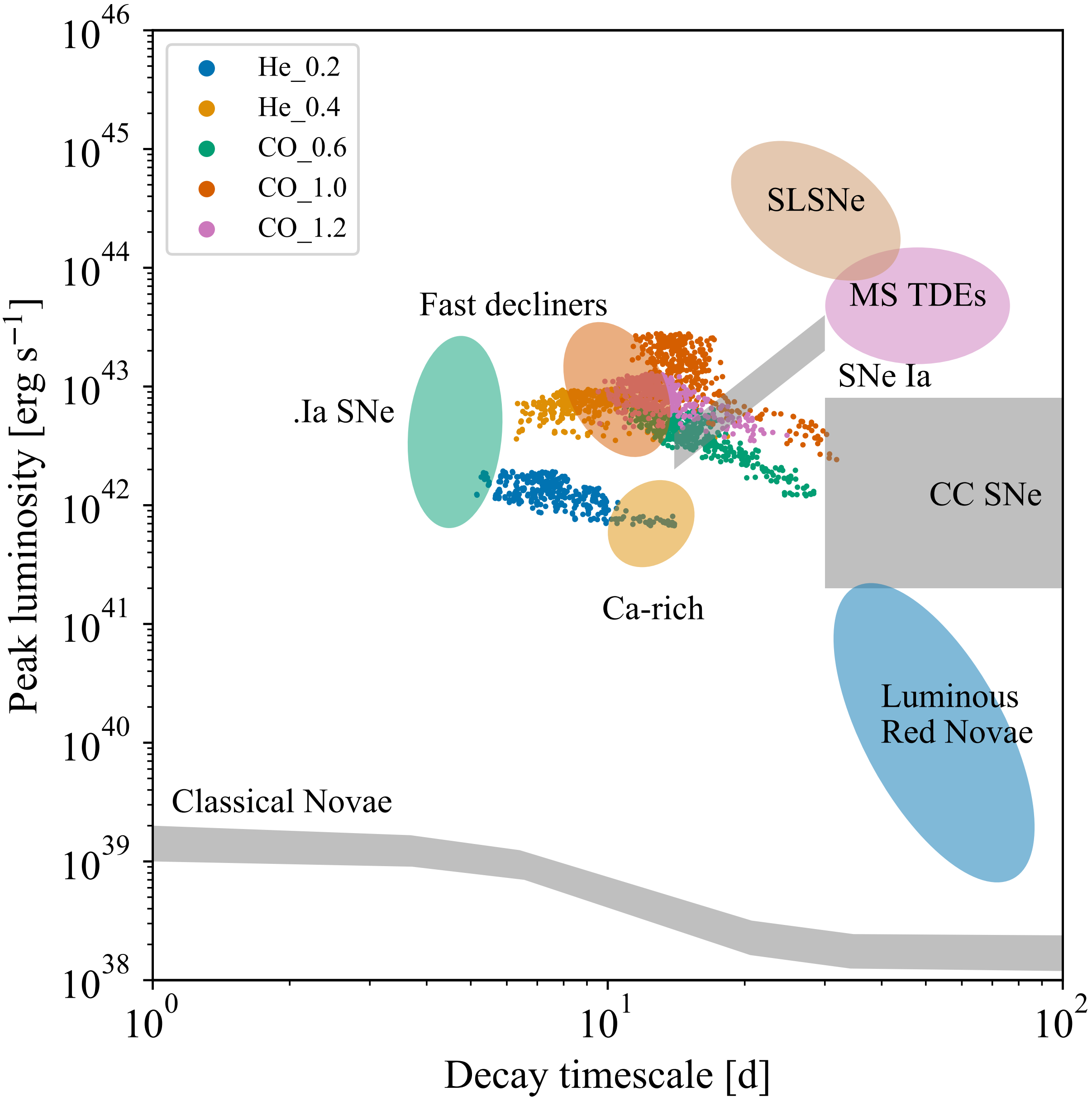

Figure 4.2: Same as Figure 1.1, except for that our models are plotted with the points. For our models, we consider various viewing angles $(\cos\theta, \phi)$ equally sampled with $(20, 20)$ bins.

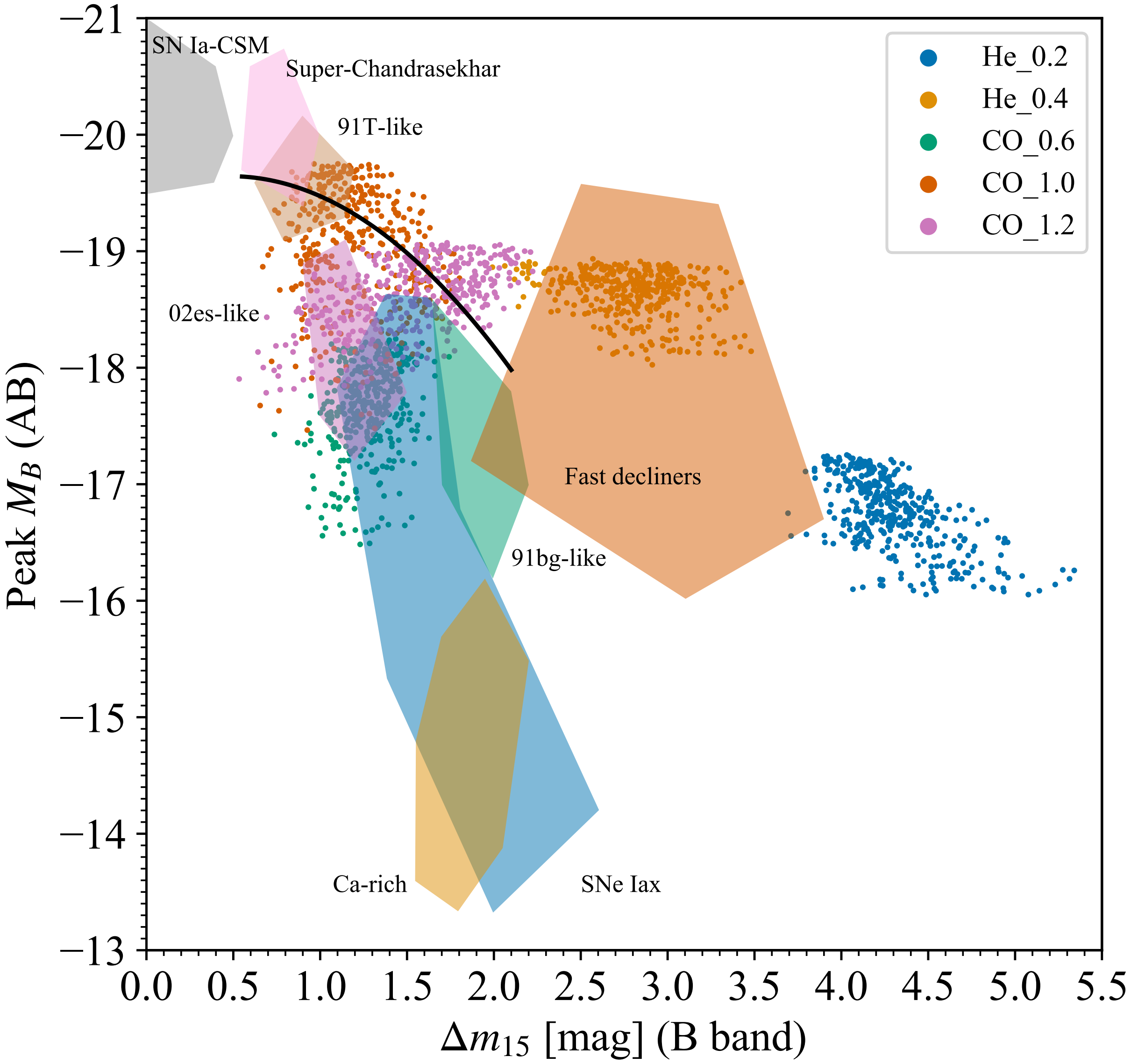

Figure 4.3: Phase spaces of observed thermonuclear transients and our models. The absolute peak B-band magnitude is plotted against the decline rate of the B-band, $\Delta m_{15}(B)$ defined as the difference between the B-band magnitude at peak and that of 15 d after the peak (Phillips, 1993). The black solid curve shows the Phillips relation (Phillips et al., 1999). Normal SNe Ia are in line with the curve, while phase spaces of peculiar classes of transients are shown with the areas filled with the colors (reproduced from Taubenberger, 2017). The points show our models, where we take different viewing angles $(\cos\theta, \phi)$ equally sampled with $(20, 20)$ bins.

Table 4.2: Properties of observed thermonuclear transients compared with our models. The peak B-band magnitude is not corrected for dust extinction or the K-correction. The luminosity distance and redshifts are taken from Tully et al. (2016) as those of host galaxies of the transients if available. Only the one exception is the luminosity distance of SN2002bj, where we take 50 Mpc from Poznanski et al. (2010). $E(B-V)$ is taken from the Open Supernova Catalog (Guillochon et al., 2017), which is also based on Schlafly & Finkbeiner (2011).

name	type	$M_{\rm peak}(B)$	luminosity distance [Mpc]	redshift	$E(B-V)$
SN2011fe	normal	-19.3	6.95	0.00079	0.0077
SN2002es	02es-like	-17.2	79.8	0.018	0.1552
SN2006bt	02es-like	-18.4	133.1	0.032	0.0424
SN1999by	91bg-like	-17.2	14.6	0.0021	0.0134
SN1991T	91T-like	-19.0	13.4	0.0058	0.0189
SN2000cx	91T-like	-18.5	23.4	0.0081	0.0698
SN2002bj	Fast decliner	-18.7	50.0	0.012	0.0787
SN2012Z	Iax	-17.7	31.2	0.0071	0.0344

- SN2000cx composes 00cx-like SNe as a rare subclass of 91T-like SNe. Its rise in the B-band and its rise and decline in all other bands redward of B, are relatively fast.

- SN2002bj, one of fast decliners, shows fast rise (< 7 d) and fast decline ($\Delta m_{15}(B) = 3.2$).

- SNe Iax are relatively fainter than normal SNe Ia. They show a wide range of $\Delta m_{15}(B)$ and $M_{\rm peak}(B)$. We select SN2012Z as a representative of SNe Iax because it has rich observations and is close to our models in the phases space of $\Delta m_{15}(B)$ and $M_{\rm peak}(B)$.

Figure 4.4 shows comparisons of multi-band light curves of our models with those of the observed thermonuclear transients. In summary, the multi-band light curves of our models do not exactly match with the observed thermonuclear transients. If we look at the B-band light curves, there are some pairs of our model and an observed transient showing similar light curves, for example, the 0.4 $M_\odot$ model and the fast decliner SN2002bj, and the 1.0 $M_\odot$ model and the 91T-like SN1991T. However, if we look at redder bands such as R/I bands, our models are generally fainter than the observed thermonuclear transients, which means our models show higher temperature than the observed transients. Figure 4.5 clearly shows the difference in the color evolution. Around the B-band peaks, the differential colors of $V-R$, $B-R$, and $R-I$ of our models are significantly smaller than those of the observed thermonuclear transients. This result is common for all the viewing angles. The relatively blue color is a key signature to distinguish the thermonuclear emission from WD TDEs from the other thermonuclear transients. Thus, transient surveys with multi-band filters would be important to search for the thermonuclear emission from WD TDEs.

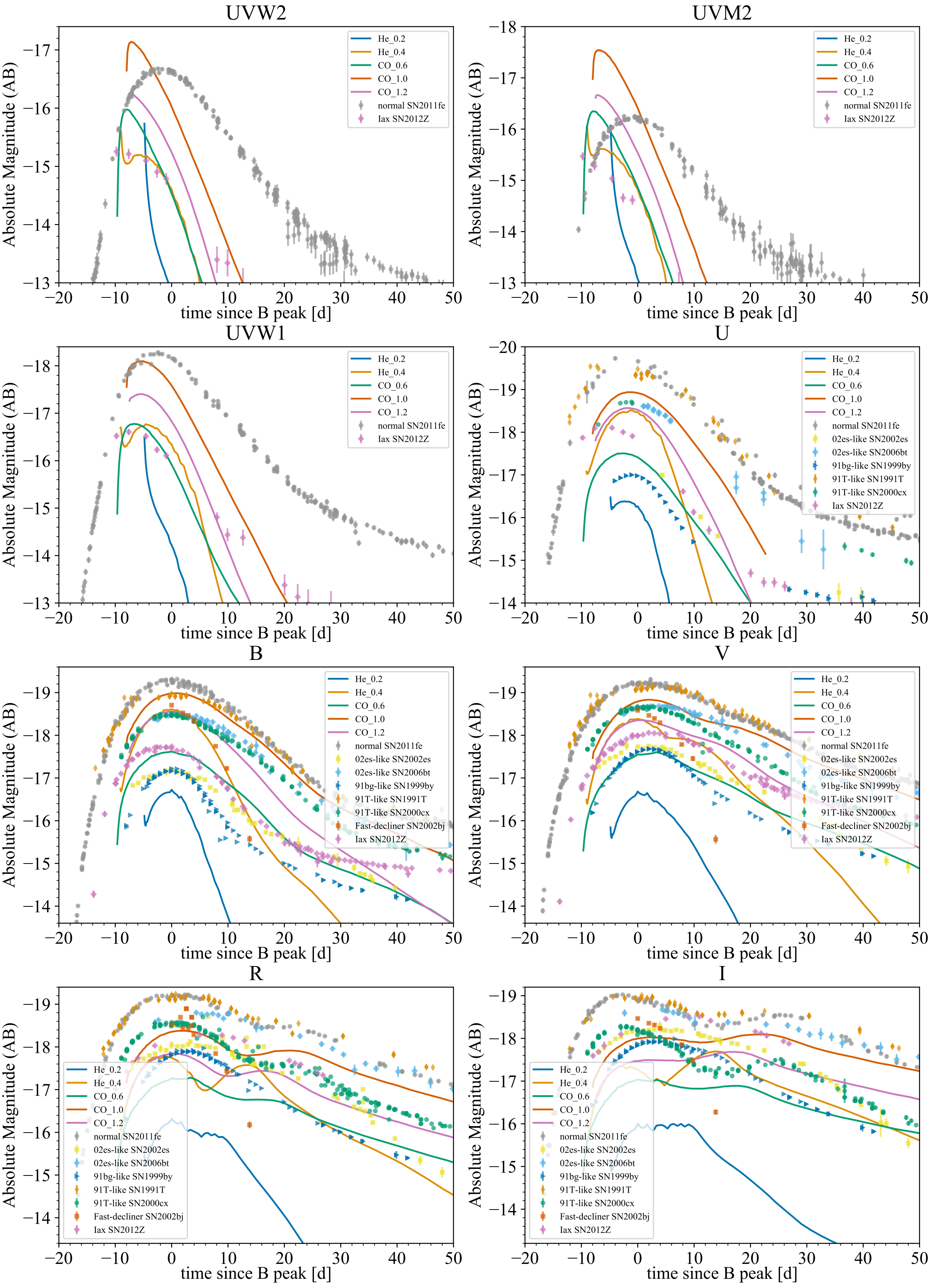

Figure 4.4: Comparisons of multi-band light curves between our models and observed thermonuclear transients. We consider band filters of Swift UVW2, UVM2, and UVW1 and those of Johnson/Bessel $UBVRI$. The solid curves show our model light curves where we take the mean over all the viewing angles. The points show the absolute magnitude of thermonuclear transients and its 1σ error. We do not make corrections for dust extinction or the K-correction for the light curves of the observed transients here.

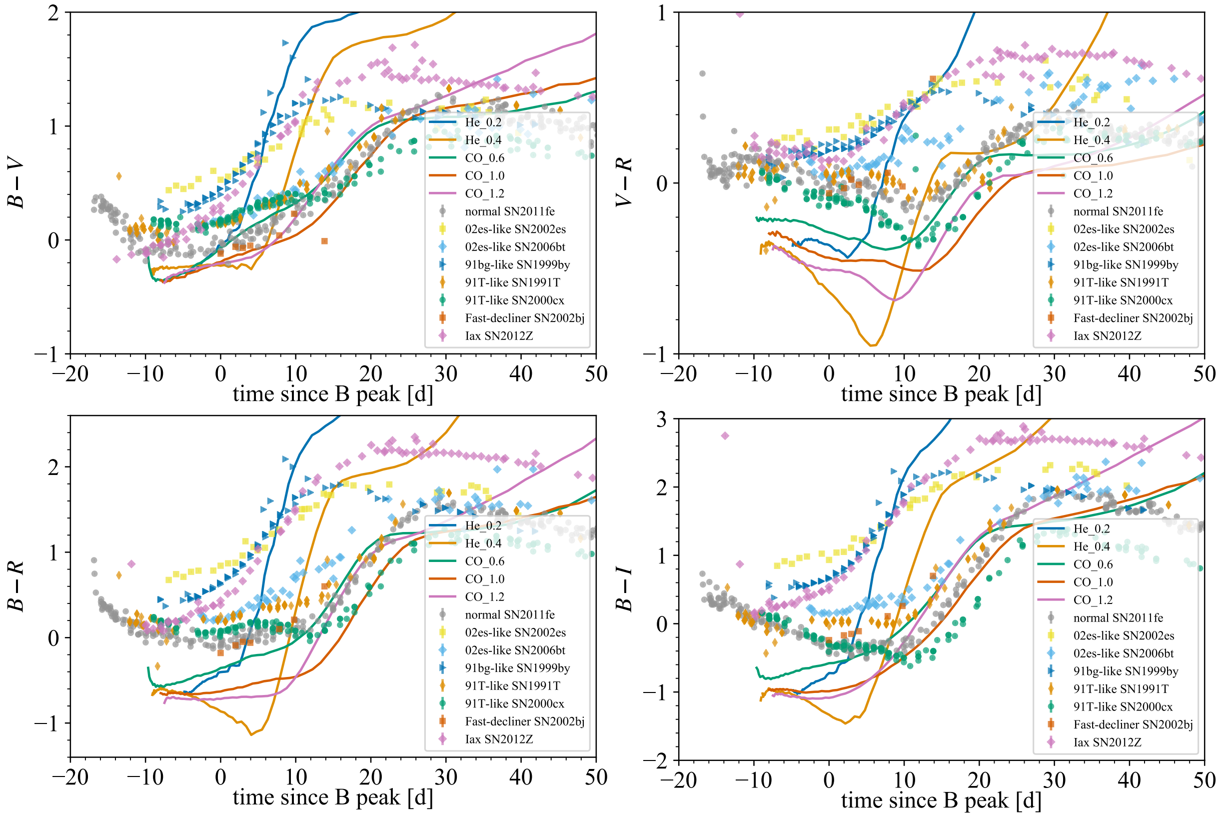

Figure 4.5: Comparisons of color evolution between our models and observed thermonuclear transients. We consider band filters of Johnson/Bessel $BVRI$. The solid curves show color evolution of our models where we take the mean over all the viewing angles. The points show that of thermonuclear transients. We do not make corrections for dust extinction or the K-correction for the light curves of the observed transients here.

We also list spectroscopic characteristics of the subclasses of thermonuclear transients as differences from normal SNe Ia as follows:

- Spectroscopic properties common among the thermonuclear transients are the absence of H lines and appearance of the following lines: C II, O I, O II, Mg II, Ti II, Ca II, and intermediate mass elements (IMEs) such as Si II, S II. Except for a fast decliner SN2002bj, the other thermonuclear transients show lines of iron group elements (IGEs) such as Fe III, Fe II, and Co II.
- 02es-like SNe are not really extreme in any spectroscopic property. A difference from normal SNe Ia is diversity in ejecta velocities: the absorption velocities of Si II 6355 Å ranges from 6,000 $\mathrm{km\,s^{-1}}$ to 10,000 $\mathrm{km\,s^{-1}}$.
- 91bg-like SNe show stronger lines of O I 7774 Å and Ti II between 4000 Å and 4400 Å than normal SNe Ia in their early-time spectra. Si II lines are also stronger, while 'W' feature of S II lines around 5300 Å is weaker.
- 91T-like SNe including 00cx-like SNe show prominent Fe III 4404 Å and 5129 Å lines in their pre-peak spectra.
- SN2002bj, a fast decliner, shows lines of He I, C II, O I, and IMEs. Ca II lines are very weak, and there is no evidence of IGEs. The line velocity is extraordinarily low.
- SNe Iax share some spectroscopic features with 91T-like SNe, such as the prominent Fe III lines in the early phase and the weak Si II and S II lines. Unique spectroscopic features of SNe Iax are low Si II velocity with a wide range of 2,000-7,000 $\mathrm{km\,s^{-1}}$. Some SNe Iax, such as SN2004cs and SN2007J, show He I lines.

Table 4.3 summarizes these spectroscopic properties of the thermonuclear transients and our models. In summary, there is no exact match between our models and the observed thermonuclear transients. Our models commonly show (very) weak IME lines, as a result of nucleosynthesis yielding low mass IMEs (see Table 4.1). This point is one of the main differences in the spectra between our models and the observed thermonuclear transients. However, we expect that the difference is not conclusive because the synthesized IME masses are sensitive to numerical resolutions (Tanikawa et al., 2017; Kawana et al., 2018). The IMEs are synthesized in regions with relatively low density, which are relatively difficult to be resolved by our simulations. There might be more IMEs if higher numerical resolutions are considered (Tanikawa, 2018b; Anninos et al., 2019). Another important difference is Doppler shifts of spectra seen in our models (see Figure 4.12). The Doppler shifts are caused by the bulk motion of the unbound ejecta with the bulk velocities shown in Table 4.1. Unless the viewing angle is perpendicular to the bulk motion, the spectra are redshifted or blueshifted with a velocity up to the bulk velocity. The Doppler shifts are thus the principal signature to distinguish the thermonuclear emission of WD TDEs with other transients with spectroscopic observations. Note that the resolution-dependent nature of the hydrodynamic simulations does not qualitatively change the characteristic Doppler shifts, although it quantitatively affects the velocity of the unbound debris.

Table 4.3: Summary of comparisons of spectral properties between observed thermonuclear transients and our models. The check and cross symbols respectively mean appearance and absence of the lines. For our models, the line velocities are calculated in the ejecta-comoving frames.

type	H	IGEs	IMEs	Si II	Si II velocity	early strong O I, Ti II	'W' of S II	early Fe III	He	Ca II
normal	×	✓	✓	normal	$\simeq 10,000\,\mathrm{km\,s^{-1}}$	×	normal	×	×	✓
02es-like	×	✓	✓	normal	6,000-10,000 $\mathrm{km\,s^{-1}}$	×	normal	×	×	✓
91bg-like	×	✓	✓	strong	$\simeq 10,000\,\mathrm{km\,s^{-1}}$	✓	weak	×	×	✓
91T-like	×	✓	✓	weak	$\simeq 10,000\,\mathrm{km\,s^{-1}}$	×	weak	✓	×	✓
Fast decliner (SN2002bj)	×	×	✓	normal	$\simeq 4,000\,\mathrm{km\,s^{-1}}$	×	normal	×	✓	very weak
Iax	×	✓	✓	weak	2,000-7,000 $\mathrm{km\,s^{-1}}$	×	weak	✓	some ✓	✓
He 0.2 $M_\odot$	×	✓	very weak*	very weak*	-*	×	×*	×	✓?†	✓
He 0.4 $M_\odot$	×	✓	very weak*	very weak*	-*	×	×*	×	✓?†	✓
CO 0.6 $M_\odot$	×	✓	weak*	weak*	$\simeq 6,000\,\mathrm{km\,s^{-1*}}$	×	weak*	×	×?†	✓
CO 1.0 $M_\odot$	×	✓	very weak*	very weak*	-*	×	×*	×	×?†	✓
CO 1.2 $M_\odot$	×	✓	very weak*	very weak*	-*	×	×*	×	×?†	✓

[*] There might be stronger IME lines than our models because numerical simulations with higher resolutions produce more IMEs (Tanikawa, 2018b; Anninos et al., 2019)

[†] Our radiative transfer simulations fail to predict profiles of He lines (see Section 4.3). Here we naively expect that He-rich ejecta would lead to the appearance of He lines.

4.3 0.2 $\mathrm{M}_\odot$ Model

In this Section, we explain important features of observational signatures of the 0.2 $Msun$ model in detail, as a representative of our 5 models. The other models are described in the following Sections, where we focus on their differences and their effects on the observational signatures.

Figure 4.6 shows the distribution of the fallback/ejecta debris and ^{56}Ni at the end of the hydrodynamic simulation of the 0.2 $\mathrm{M}_\odot$ model. The ejecta shape is very aspherical due to the tidal disruption. The properties of the unbound ejecta are as follows. The ejecta mass is $0.12\,\mathrm{M}_\odot$. Its COM escapes from the BH with the velocity of $11,700\,\mathrm{km\,s^{-1}}$. The kinetic energy with respect to the COM is 8.8×10^{49} erg.

Figure 4.7 shows the synthesized nuclear compositions of the ejecta in the 0.2 $\mathrm{M}_\odot$ model. For comparison, we also show abundance derived from the simplified nuclear reaction networks adopted in the hydrodynamic simulation. The radioactive nuclei are dominated by ^{56}Ni with its mass of $0.030\,\mathrm{M}_\odot$. There is more Ca with its mass of $0.0014\,\mathrm{M}_\odot$ than Si with its mass of $7.0 \times 10^{-4}\,\mathrm{M}_\odot$. Interestingly, this nuclear composition differs from SNe Ia and from the models of CO WD TDEs, while it is qualitatively consistent with previous studies on helium WD detonations (Holcomb et al., 2013).

Figure 4.8 shows the synthetic multi-band light curves of the 0.2 $\mathrm{M}_\odot$ model. The model shows more rapid evolution than the other models and the observed thermonuclear transients. It is also the faintest among all the models. Depending on the viewing angle, the isotropic equivalent peak luminosity varies over $L_{\mathrm{peak}} \simeq 0.7$–$2.0 \times 10^{42}\,\mathrm{erg\,s^{-1}}$ (see Figure 4.9). The decay timescale defined as the time in which the bolometric luminosity declines by one magnitude from the peak also varies over $\Delta t_{1\mathrm{mag}} \simeq 5$–10 days. These features are caused by a less-massive ejecta mass and ^{56}Ni mass ($0.12\,\mathrm{M}_\odot$ and $0.030\,\mathrm{M}_\odot$, respectively). The luminosities and timescales resemble those of calcium-rich transients, .Ia SNe, and rapid transients (see Figure 4.2). The color of the light curves also rapidly evolves: $g-r \simeq -0.4$ mag and $r-i \simeq -0.5$ mag around the peak, while $g-r \simeq +0.9$ mag and $r-i \simeq -0.2$ mag at 10 days after the peak. There are second humps in the near-infrared (NIR) izy bands at $t \simeq 12$–18 days, which are commonly seen in SNe Ia (see Figure 4.4), and originate from the recombination of Fe/Co III to Fe/Co II. The second humps are produced when the NIR emissivity of Fe/Co dramatically increases at a temperature of $\simeq 7000$ K due to the recombination (Kasen, 2006).

Figure 4.9 shows a strong dependence of the peak luminosity on the viewing angle. Figure 4.10 also shows how the multi-band light curves vary by the viewing angle. The strong dependence on the viewing angle shown in Figure 4.9 reflects the very aspherical shape of the ejecta (see Figure 4.6), which is a characteristic of the tidal disruption. The brightest emission appears for a viewing angle $\phi \simeq 0.8\pi$, where a projected surface area of the ejecta is maximized and also photons escape from the ejecta more quickly than at other angles. The rapid photon diffusion results in a fast decline ($\Delta t_{1\mathrm{mag}} \simeq 5$ days) and bluer color ($g-r \simeq -0.5$ around the peak) for this brightest viewing angle. In contrast, the faintest emission is realized when $\phi \simeq 0.2\pi$, which shows a slow decline ($\Delta t_{1\mathrm{mag}} \simeq 10$ days) and redder color ($g-r \simeq -0.1$ around the peak). Because of the aspherical shape of the ejecta, we also expect that thermonuclear emission from WD

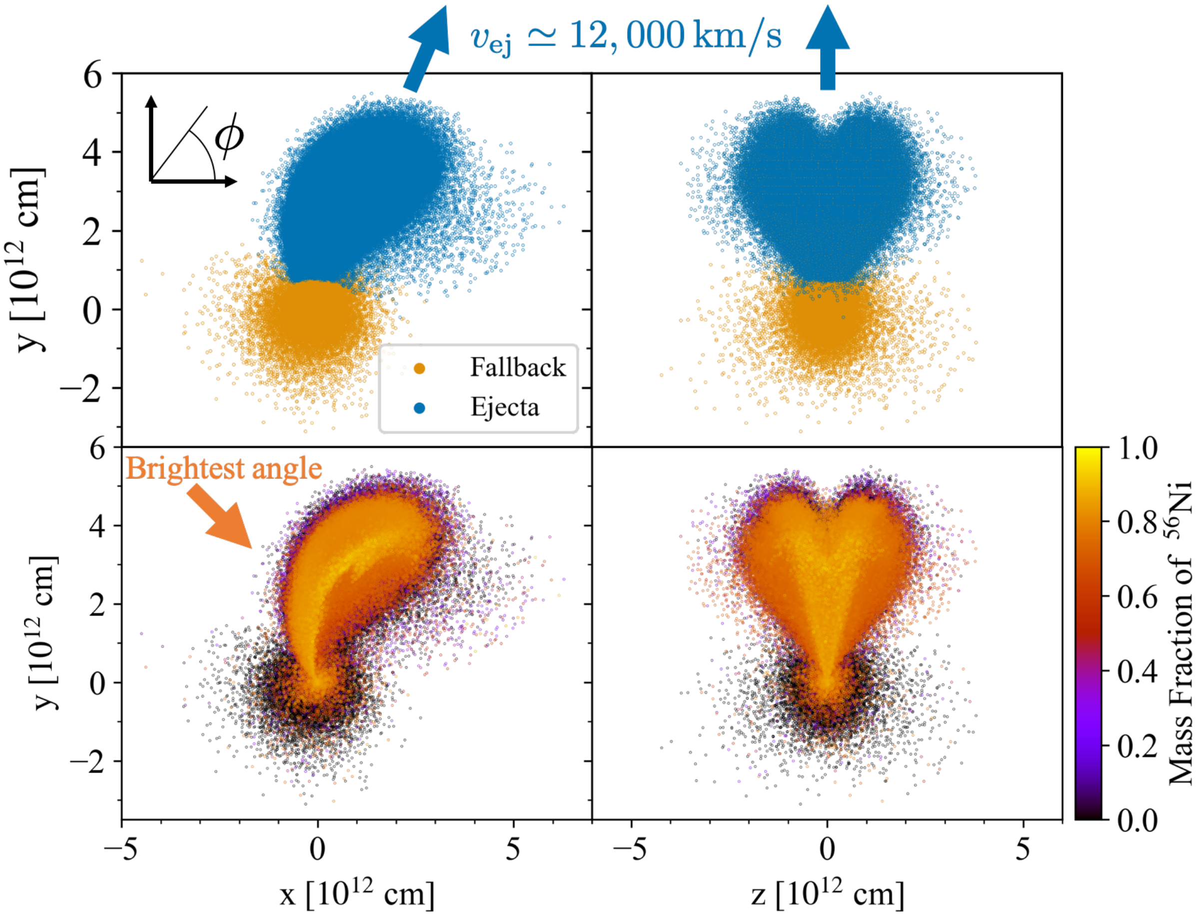

Figure 4.6: Distribution of the debris at the end of the hydrodynamic simulation in the 0.2 $M_\odot$ model. The upper panels show the distribution of fallback and ejecta debris, and the lower panels show the ^{56}Ni distribution. We also show the azimuthal angle ϕ of the spherical coordinates used in the radiative transfer simulation.

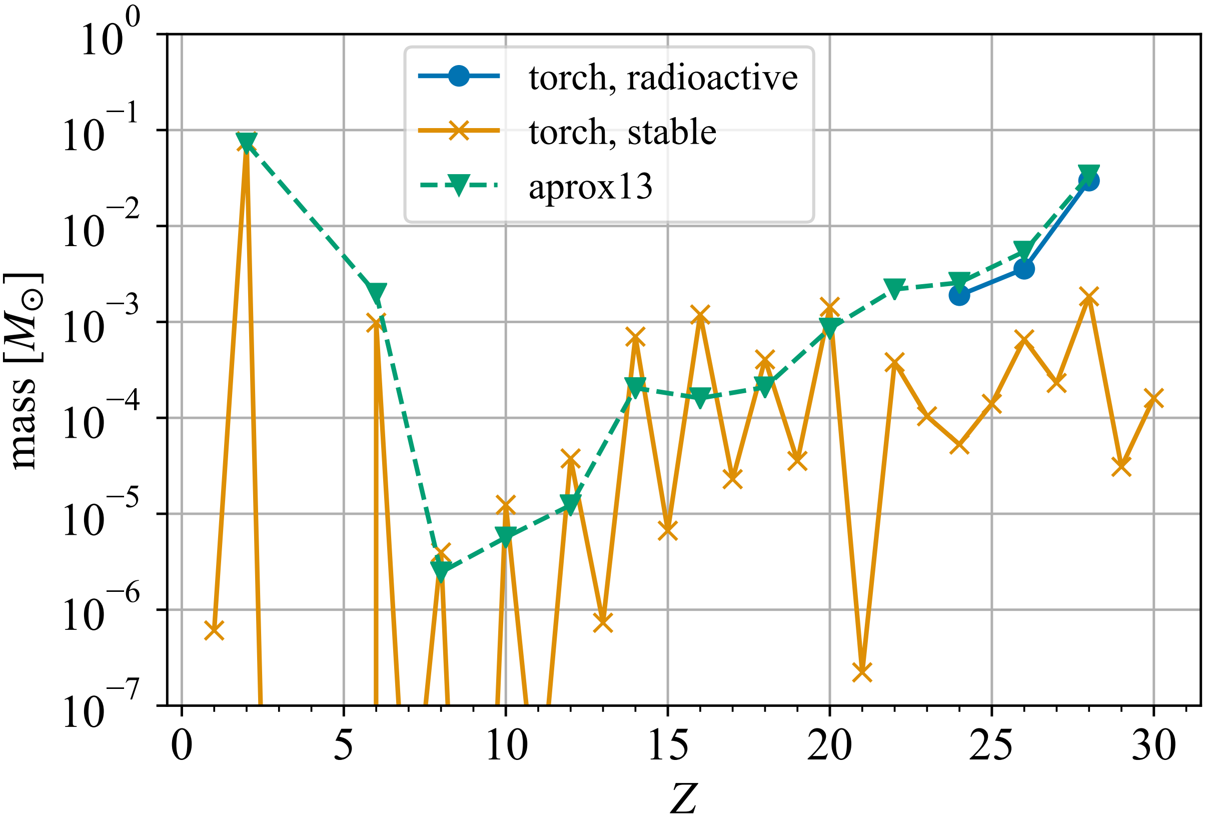

Figure 4.7: Nucleosynthesis in the 0.2 M$_\odot$ model. The blue and orange lines respectively show the masses of radioactive and stable elements in the unbound ejecta derived from the detailed nucleosynthesis simulation. The green line shows those derived from the simple nuclear reaction networks adopted in the hydrodynamic simulation.

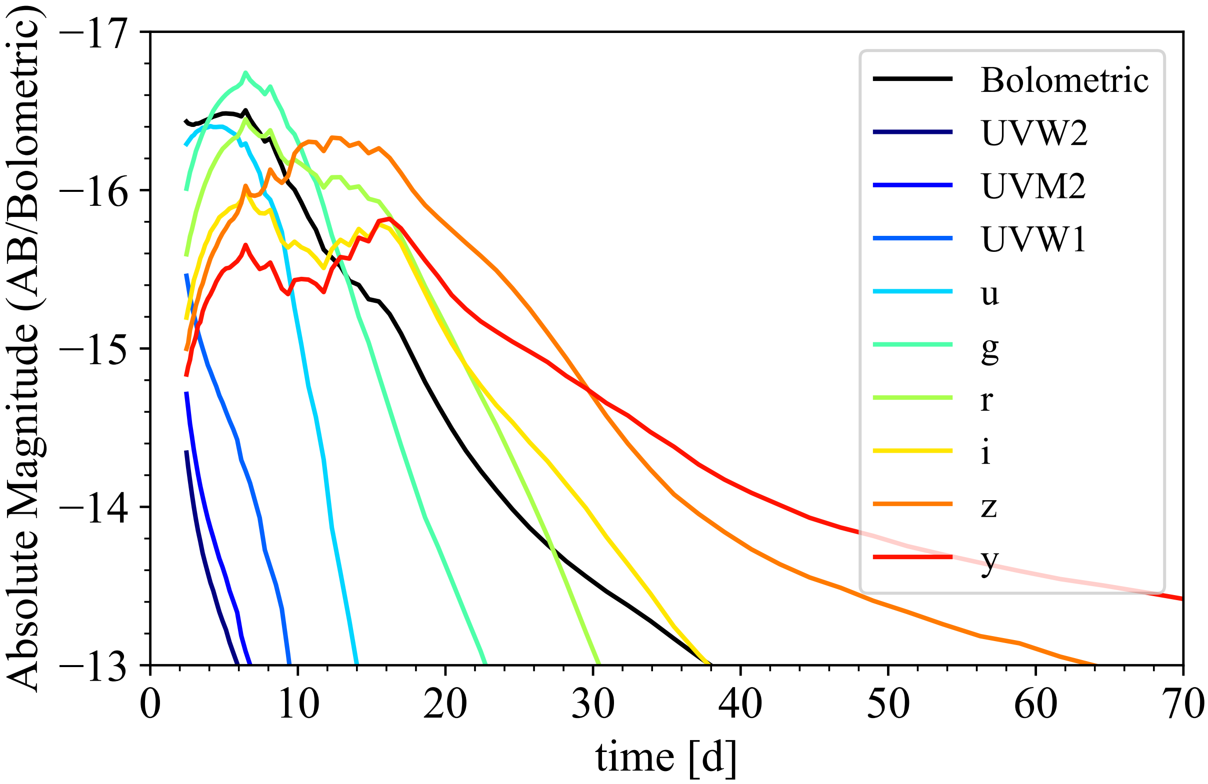

Figure 4.8: Multi-band light curves of the 0.2 $M_\odot$ model. We consider filters of the Swift and LSST here. The origin of the time is when the first WD-BH pericenter passage occurs.

TDEs may show polarization (Shapiro & Sutherland, 1982; Hoflich, 1991).

Figure 4.11 shows the time evolution of the synthetic spectra of the 0.2 $M_\odot$ model and a spectrum of SN Iax 2012Z, which shows similar features to the 0.2 $M_\odot$ model. They share some features with SNe Ia: the absence of hydrogen lines, the appearance of strong Fe II lines from 4000 to 5000 Å, and P Cygni profiles (see also Table 4.3). Because of the abundance in the 0.2 $M_\odot$ model, Ca II H/K and infrared (IR) triplet emission lines clearly appear, while silicon emission/absorption lines around 6150 Å are absent or very weak, interestingly. The appearance/absence of these lines does not differ by the viewing angle. It is interesting whether helium lines appear or not because the ejecta are helium-rich with 0.076 $M_\odot$ (see Figure 4.7) and some SNe Iax show the helium lines (Foley et al., 2013). However, our radiative transfer simulation is not able to investigate this issue, because the local thermal equilibrium assumption results in failure of excitation of neutral helium (Harkness et al., 1987; Lucy, 1991; Hachinger et al., 2012).

Figure 4.12 shows the Ca II IR triplet profile dependent on the viewing angle. The spectra are redshifted or blueshifted, depending on the viewing angle, with velocities up to $\simeq 11,700\,\mathrm{km\,s^{-1}}$. This spectral shift is commonly seen in the CO WD TDE model of MacLeod et al. (2016) with its velocity up to $\simeq \pm 10,000\,\mathrm{km\,s^{-1}}$. This is one of the distinguishable features of the WD TDEs from the other transients such as SNe Ia. The

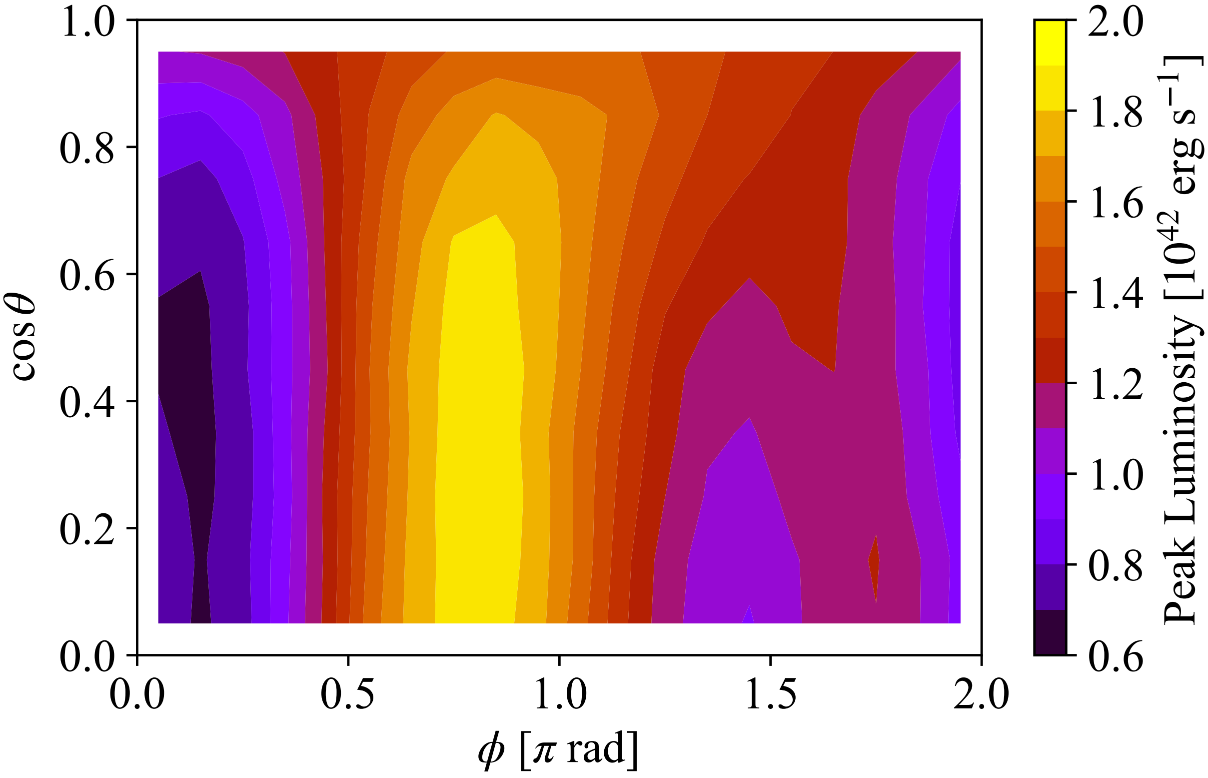

Figure 4.9: Isotropic equivalent peak luminosity of the $0.2\,\mathrm{M}_\odot$ model as a function of viewing angle.

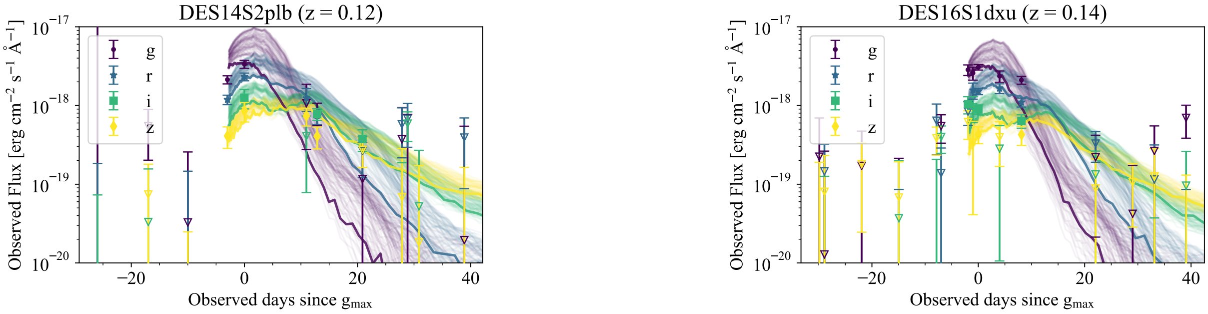

(a) DES14S2plb (rapid and faint)

(b) DES16S1dxu (rapid and faint)

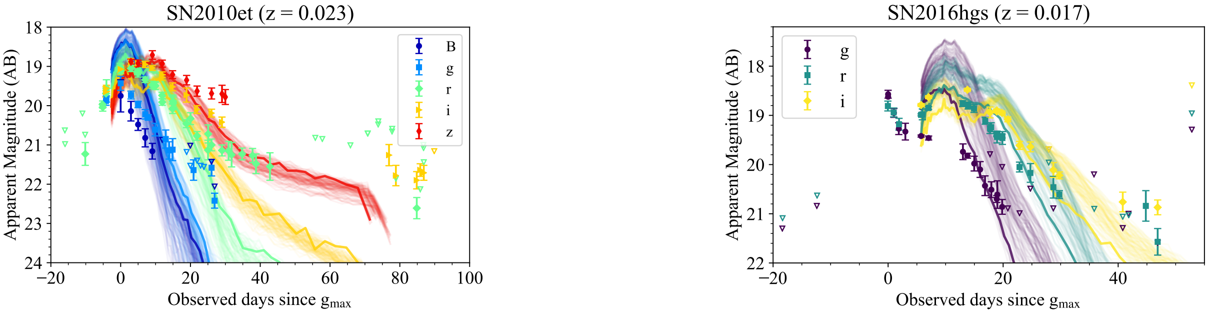

(c) SN2010et (calcium-rich)

(d) SN2016hgs (calcium-rich)

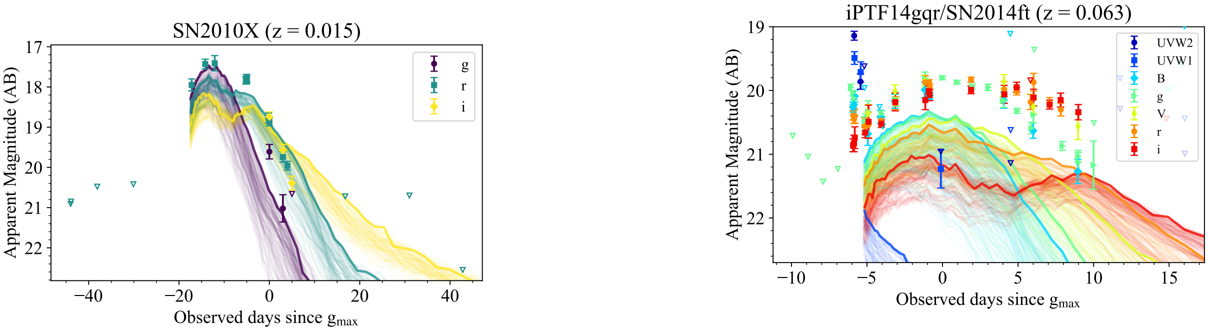

(e) SN2010X (candidate of .Ia SNe)

(f) iPTF14gqr/SN2014ft (rapid type Ic)

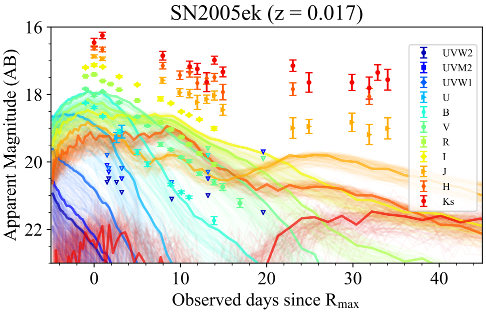

(g) SN2005ek (rapid type Ic)

Figure 4.10: Comparisons between the 0.2 $M_\odot$ model and some rapid transients reported so far. We compare them with rapid and faint transients reported in Pursiainen et al. (2018), calcium-rich transients SN2010et (Kasliwal et al., 2012) and SN2016hgs (De et al., 2018b), a candidate of .Ia SNe SN2010X (Kasliwal et al., 2010), and rapid type Ic transients iPTF14gqr/SN2014ft (De et al., 2018a) and SN2005ek (Drout et al., 2013). The points show the observed flux/magnitude and its 1σ error. The open triangles in the panels (a, b) are the cases where the detection significance is less than 3σ, while those in the other panels show upper limits. The thin solid curves show the 0.2 $M_\odot$ model light curves with different viewing angles $(\cos\theta, \phi)$ equally sampled with $(10, 10)$ bins. The thick solid curves show those with the angle where the model can best fit the observations.

spectral shift is caused by the intrinsic bulk motion of the unbound ejecta. An orbital energy distribution of the tidal debris of the WD is spread due to the tidal disruption by the BH. The unbound ejecta gains positive orbital energy in this process, corresponding to the velocity of

$$\begin{aligned} v_t &\sim (2\Delta\epsilon_t)^{1/2} && (4.1)\\ &\sim \left(2\beta^n \frac{GM_{\rm BH}R_{\rm WD}}{R_t^2}\right)^{1/2} && (4.2)\\ &\simeq 7.9\times 10^3\,{\rm km\,s^{-1}}\beta^{n/2}\left(\frac{R_{\rm WD}}{10^9\,{\rm cm}}\right)^{-1/2}\left(\frac{M_{\rm BH}}{10^{2.5}\,{\rm M}_\odot}\right)^{1/6}\left(\frac{M_{\rm WD}}{0.2\,{\rm M}_\odot}\right)^{1/3}, && (4.3)\end{aligned}$$

where we use the expression of $\Delta\epsilon_t$ shown in Equation (2.12). The velocity is a little smaller than the velocity of the bulk motion, $\simeq 11,700\,{\rm km\,s^{-1}}$. In addition to the tidal dissipation, the released nuclear energy increases the orbital energy of the ejecta. Both the contributions by the tidal disruption and release of the nuclear energy result in the red/blueshift of spectra.

Not only does the Doppler shift depend on the viewing angle, but also absorption velocities do as well. Figure 4.12 also shows the absorption velocities of the Ca II IR triplet line at $t \simeq 16$ days for different viewing angles in the observer frame. In the ejecta-comoving frame, the corresponding absorption velocity is relatively smaller ($-11,000\,{\rm km\,s^{-1}}$) from the brightest angle ($\phi \simeq 0.8\pi$) than from the faintest angle ($\phi \simeq 0.2\pi$), where it is $-15,000\,{\rm km\,s^{-1}}$. This is because the radial velocity with respect to the COM of the ejecta is smaller for the brightest angle than the faintest angle (see Figure 4.6).

The synthetic spectra of the 0.2 $M_\odot$ model are remarkably similar to the spectra of SNe Iax. For example, Figure 4.11 shows that the day 12 spectrum of the 0.2 $M_\odot$ model (in the declining phase in the V-band) resembles that of SN Iax 2012Z around its V-band maximum (Stritzinger et al., 2015; Yamanaka et al., 2015). Both the spectra show strong lines of Fe II, Fe III, Ca II, and other Fe-peak elements (Branch et al., 2004; Stritzinger et al., 2014). The similarity may indeed be reasonable; the 0.2 $M_\odot$ model produces a mixture of Fe, Fe-peaks, and Ca, which is qualitatively similar to the weak/failed SN Ia model that explains the spectra of SNe Iax (Kromer et al., 2013), except that the 0.2 $M_\odot$ model shows the higher expansion velocity. The main differences are the nearly complete lack of Si II and S II in the TDE spectra, and the broader, more blue-shifted lines in the TDE. Another difference appears in their their declining timescales: the 0.2 $M_\odot$ model has a more rapid decline (Δm_{15}(B) $\simeq 4$ mag) than those of SNe Iax (Δm_{15}(B) $\simeq 0.5$–2.5 mag). However, it is still an interesting possibility that a sub-population of SNe Iax may be explained by the 0.2 $M_\odot$ model, because the properties of SNe Iax have a large variety (Stritzinger et al., 2015; Jha, 2017).

The light curves of the 0.2 $M_\odot$ model are similar in timescales and luminosities to the calcium-rich transients (Perets et al., 2010; Kasliwal et al., 2012; Valenti et al., 2014; Lunnan et al., 2017; Milisavljevic et al., 2017; De et al., 2018b), observed candidates of .Ia SNe (Kasliwal et al., 2010), and other rapid transients (Drout et al., 2013, 2014; De

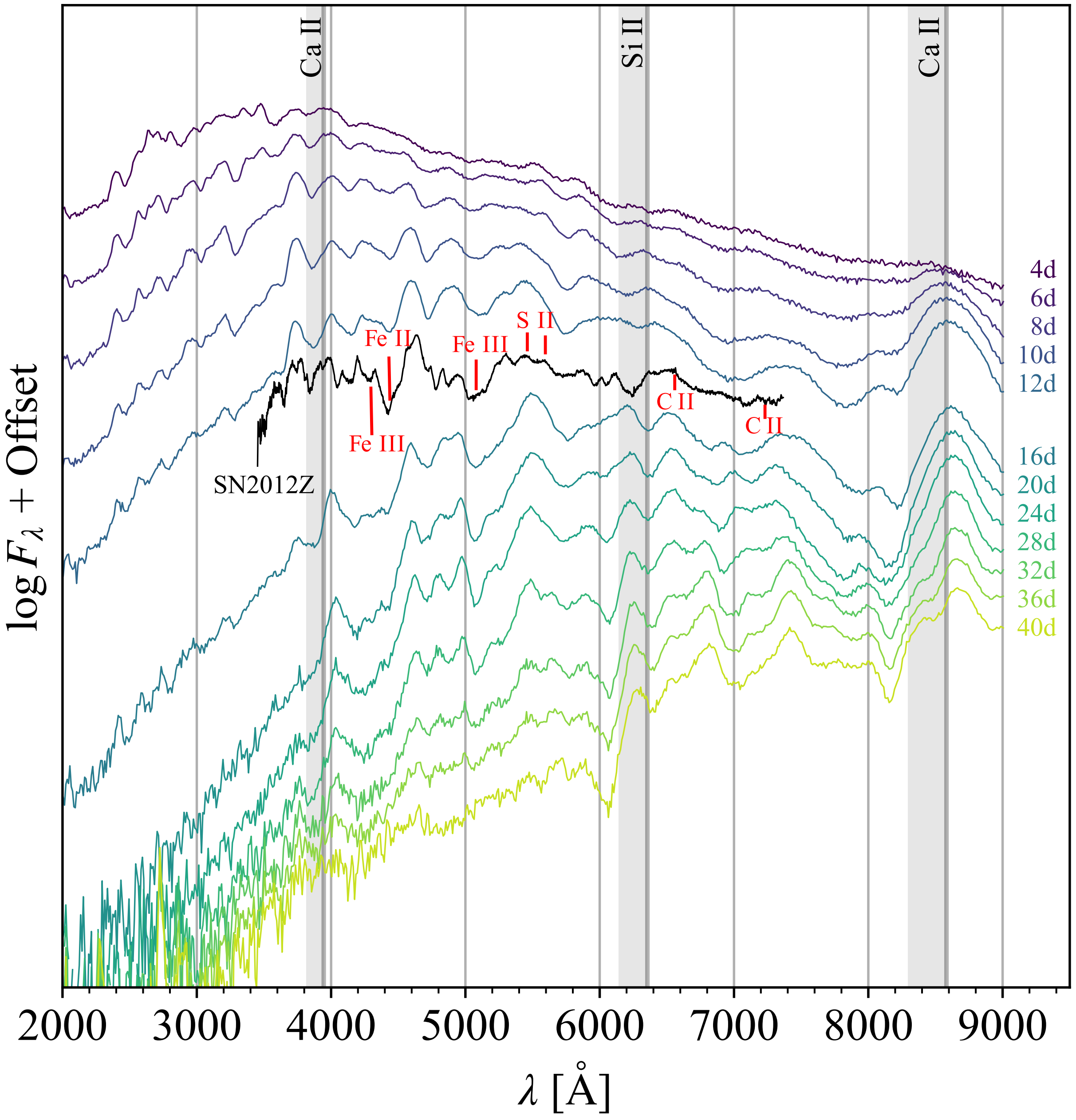

Figure 4.11: Time evolution of spectra of 0.2 M$_\odot$ model. The spectral evolution is calculated by taking the mean over all the angles in the ejecta-comoving frame, and the time is since the tidal disruption. The vertical thick gray lines show rest-frame wavelengths of some lines seen in SNe Ia, and the vertical gray shades show ranges of the wavelengths shifted with a velocity range from $-10,000\,\mathrm{km\,s^{-1}}$ to $0\,\mathrm{km\,s^{-1}}$. Some other spectral lines are shown with the red labels. For comparison, we also show a +1.1 days spectrum of SN2012Z since its V maximum with the black line (Foley et al., 2013).

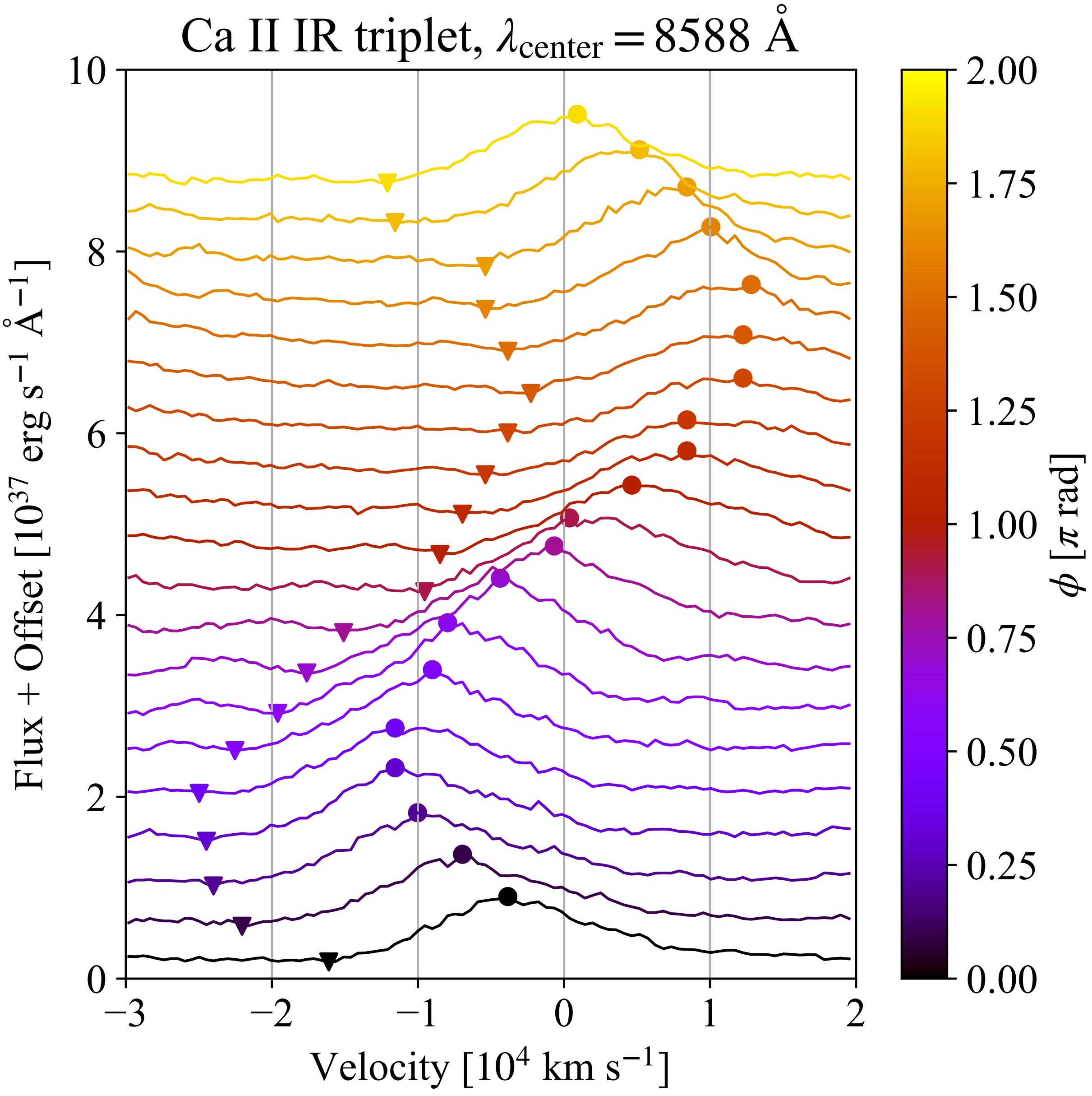

Figure 4.12: Viewing-angle dependence of spectra of $0.2\,\mathrm{M}_\odot$ model. We show the viewing angle dependence of the shape of Ca II IR triplet lines at $t \simeq 16$ days. The circles show peaks of the emission lines, and the triangles show the minima of the absorption lines. We take the mean over the angle of $-0.3 < \cos\theta < 0.3$ with 20 samples of ϕ.

et al., 2018a; Pursiainen et al., 2018). We compare the 0.2 $M_\odot$ model with observed transients of these classes, on their multi-band light curves (see Figure 4.10) and their spectra. There is no good match between the model and the calcium-rich transients, observed candidates of .Ia SNe, or rapid transients reported in Drout et al. (2013, 2014), and De et al. (2018a). The model shows brighter and bluer emission around the peak than the calcium-rich transients. This is because the model has a larger ^{56}Ni mass, 0.030 $M_\odot$ than the calcium-rich transients, whose ^{56}Ni masses are $\lesssim 0.015\,M_\odot$. Additionally, the model shows very weak silicon lines, while in contrast some calcium-rich transients, such as PTF10iuv/SN2010et (Kasliwal et al., 2012) and SN2016hgs (De et al., 2018b), show strong silicon features. SN2010X, an observational candidate of .Ia SNe, also shows strong silicon lines and thus does not match the model, while their light curves are similar except for the r-band maximum: the r-band maximum of the model is brighter than SN2010X by $\simeq -0.4$ mag. Compared with the rapid transients reported in Drout et al. (2013, 2014) and De et al. (2018a), the model shows fainter peak luminosity.

The model well explains multi-band light curves of two rapid transients reported in Pursiainen et al. (2018). These transients, DES14S2plb and DES16S1dxu, have physical offsets from the centers of their host galaxies as 3.26 kpc and 10.2 kpc, respectively. DES16S1dxu is notably far from its host center, which may imply that its environment is an old stellar population. This may support interpreting its origin as a WD TDE, because the plausible environments of WD TDEs are a dwarf galaxy or globular cluster containing an IMBH and WD (see Section 2.2.2). Though comparisons of spectra between the model and these transients are important to certainly identify their origin(s), such observational data are lacking. An interesting point is that the transients are two of the faintest transients among the rapid transients reported in Drout et al. (2013, 2014), De et al. (2018a), and Pursiainen et al. (2018). Pursiainen et al. (2018) reported a much larger sample of rapid transients than the other studies, and thus they would be able to find the faintest transients with relatively low event rates. To find WD TDEs like the 0.2 $M_\odot$ model more frequently and more certainly, we propose to search for a larger number of faint and rapid transients and to perform rapid spectroscopic follow-ups.

4.4 0.4 $M_\odot$ Model

Figure 4.13 shows the distribution of fallback/ejecta debris and ^{56}Ni at the end of the hydrodynamic simulation of the 0.4 $M_\odot$ model. Due to more violent thermonuclear explosions, the bulk velocity of the unbound ejecta with respect to the BH is larger ($\simeq 17,100\,\mathrm{km\,s^{-1}}$) than that of the 0.2 $M_\odot$ model ($\simeq 11,700\,\mathrm{km\,s^{-1}}$). The mass of unbound ejecta is 0.314 $M_\odot$, or 79% of the initial WD mass.

Figure 4.14 shows the elemental abundance of the ejecta in the 0.4 $M_\odot$ model. It is very similar to that of the 0.2 $M_\odot$ model: ^{56}Ni is dominant in the radioactive nuclei with its mass of $0.23\,M_\odot$, and Ca is more dominant than Si. The similarity is due to the same initial composition of ^{4}He 100% between the 0.2 and 0.4 $M_\odot$ model (Kawana et al., 2018).

The multi-band light curves of the 0.4 $M_\odot$ model are shown in Figure 4.4 and Figure 4.15. The variety of photometric properties caused by the viewing angle effect is

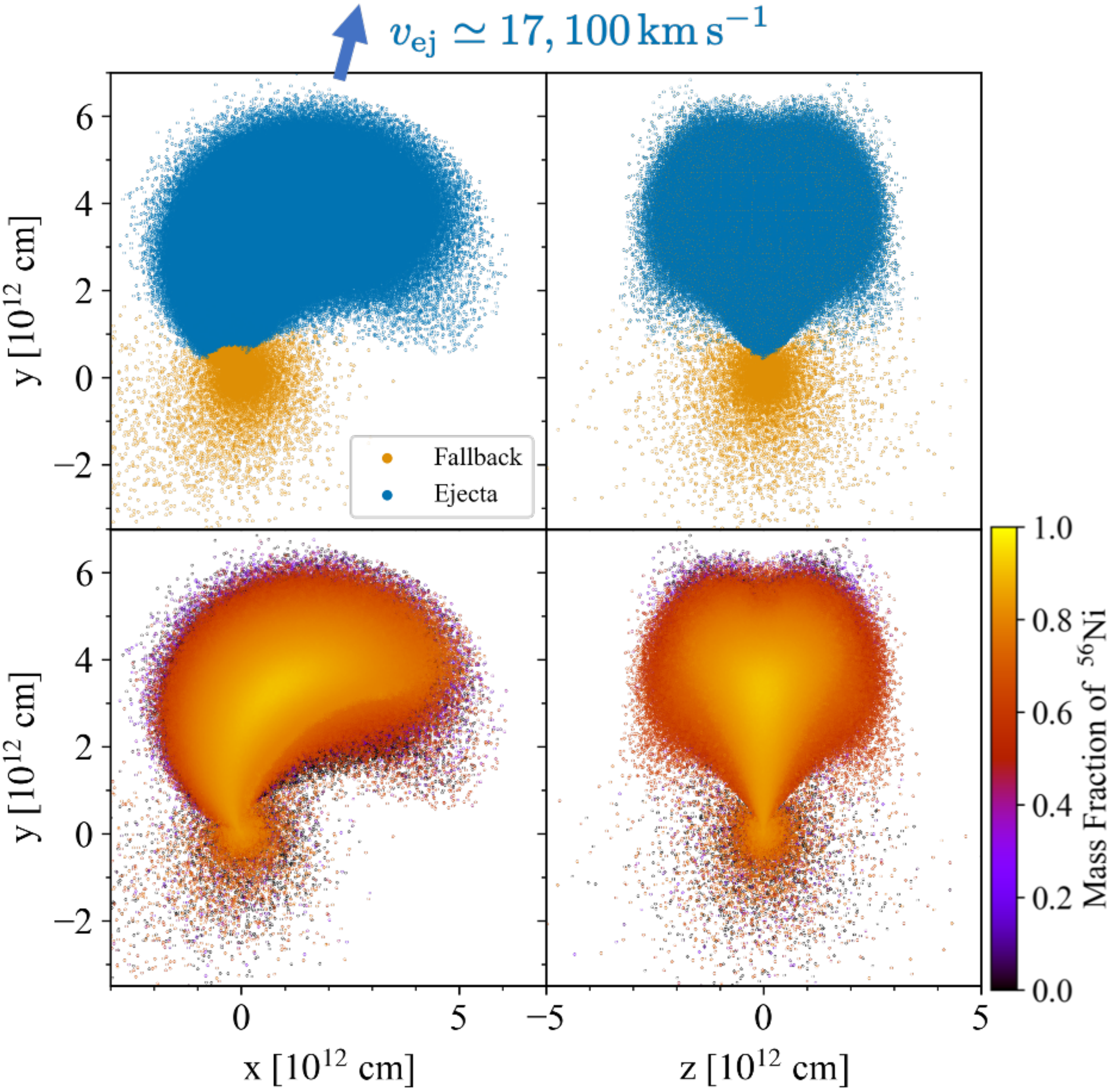

Figure 4.13: Same as Figure 4.6 for the $0.4\,\mathrm{M}_\odot$ model.

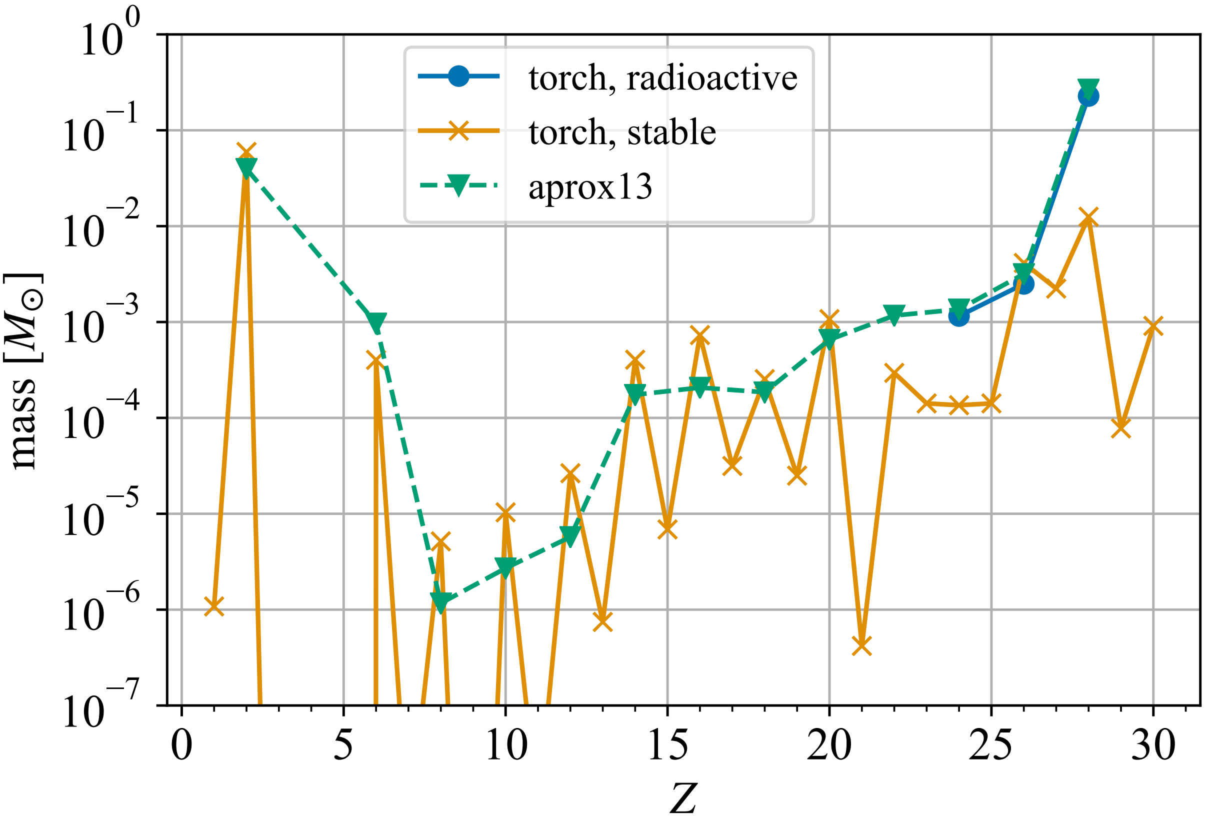

Figure 4.14: Same as Figure 4.7 for the 0.4 M$_\odot$ model.

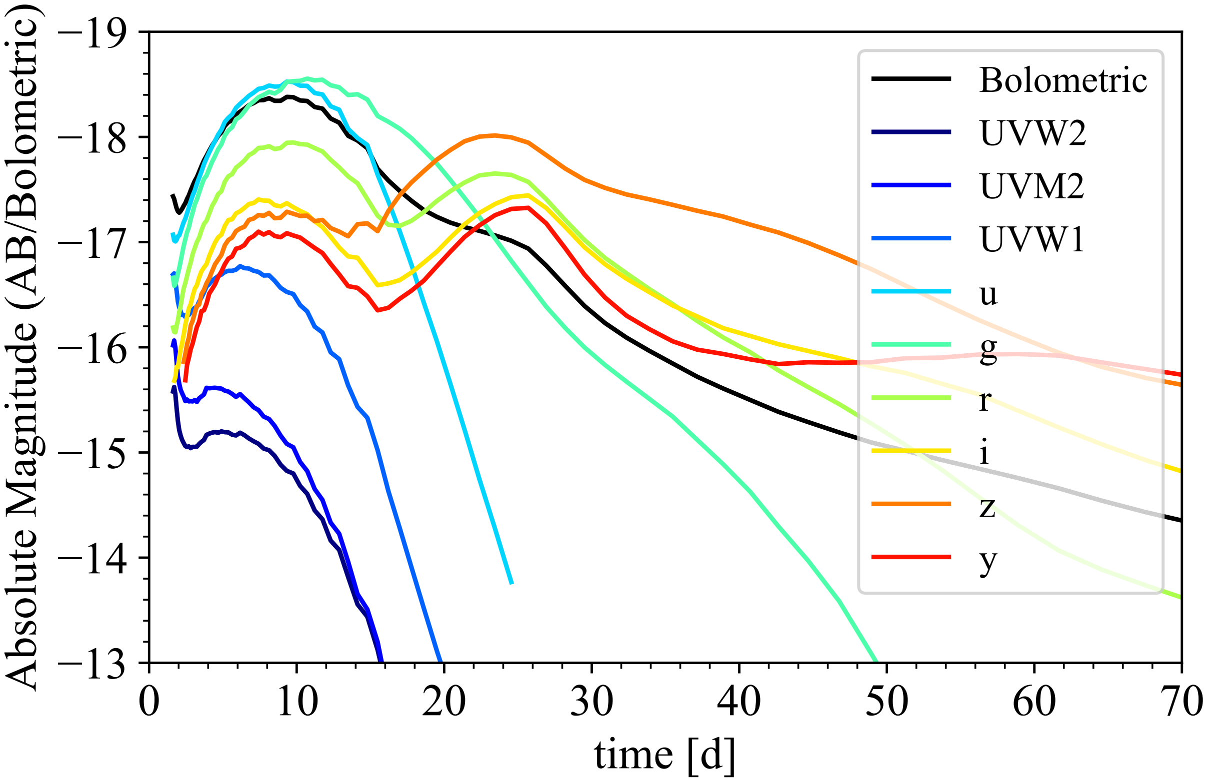

Figure 4.15: Same as Figure 4.8 for the 0.4 $M_\odot$ model.

shown in Figure 4.2 and Figure 4.3. Its *B*-band light curve is very similar to a fast decliner SN2002bj. However, in other bands of *VRI*, the 0.4 $M_\odot$ model is fainter around the *B*-band peak. The 0.4 $M_\odot$ model shows the clear second hump in *RI* bands because it is rich in IGEs, while SN2002bj does not.

Figure 4.16 shows the spectral evolution of the 0.4 $M_\odot$ model and the comparison of it with SN2002bj. The spectra of the 0.4 $M_\odot$ model are similar to those of the 0.2 $M_\odot$ model in the senses that they show strong lines of IGEs and Ca II but IME lines are very weak or absent. Compared with the spectrum of SN2002bj, the model has several different points: line velocities are much larger, IME lines are much weaker, and Ca II lines are much stronger. An interesting feature of SN2002bj is the appearance of He lines. Although our radiative transfer simulations cannot model the appearance/absence of He lines, the 0.4 $M_\odot$ model might show the He lines because it is rich in He.

4.5 0.6 $M_\odot$ Model

Figure 4.17 shows the distribution of fallback/ejecta debris and ^{56}Ni at the end of the hydrodynamic simulation of the 0.6 $M_\odot$ model. The mass of unbound ejecta is 0.440 $M_\odot$, or 73% of the initial WD mass. Because the thermonuclear explosions are moderate in the 0.6 $M_\odot$ model, the bulk velocity of the unbound ejecta is 10,900 km s^{-1}, which is the slowest among our 5 models. It also results in the lower kinetic energy with respect

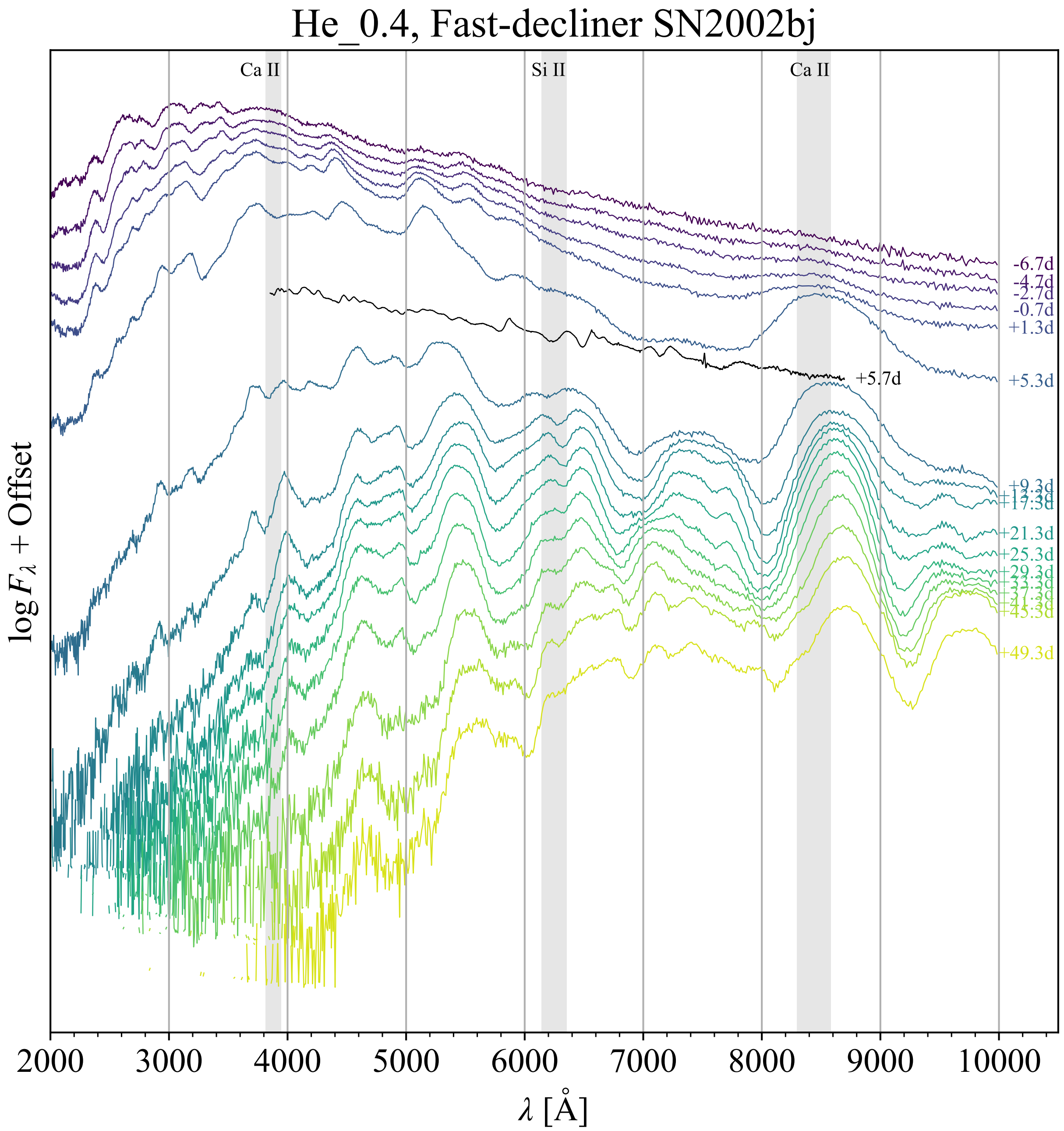

Figure 4.16: Same as Figure 4.11 except for that here we compare the 0.4 $M_\odot$ model spectra with the observed fast decliner SN2002bj, and we show time since the B-band peak.

to the COM of the unbound ejecta, 1.14×10^{50} erg, than that of the 0.4 $M_\odot$ model, 2.90×10^{50} erg, even though the unbound mass of the 0.6 $M_\odot$ model is larger.

Figure 4.18 shows the elemental abundance of the ejecta in the 0.6 $M_\odot$ model. There are clear differences from the He WD TDE models, or the 0.2 and 0.4 $M_\odot$ models. A difference is the He mass: there is a much smaller He in the 0.6 $M_\odot$ model (0.0020 $M_\odot$) than the 0.2 $M_\odot$ model (0.059 $M_\odot$) and the 0.4 $M_\odot$ model (0.076 $M_\odot$). This is because the He WD TDE models have an unburnt part in the unbound ejecta, preserving their initial elemental abundance. This point also results in larger masses of carbon (0.11 $M_\odot$) and oxygen (0.13 $M_\odot$) in the 0.6 $M_\odot$ model than the He WD TDE models. Another difference is the dominance of Si over Ca: the Si mass of 0.038 $M_\odot$ is much larger than the Ca mass of 0.0046 $M_\odot$.

The multi-band light curves of the 0.6 $M_\odot$ model are shown in Figure 4.4 and Figure 4.19. The variety of photometric properties caused by the viewing angle effect is shown in Figure 4.2 and Figure 4.3. Its B-band light curve is similar to an SN Iax SN2012Z, and is in the range of 02es-like SNe. However, in redder bands of VRI the 0.6 $M_\odot$ model is fainter around the B-band peak.

Figure 4.20 shows the spectral evolution of the 0.6 $M_\odot$ model and the comparison of it with a normal SN Ia, 02es-like SN, 91bg-like SN, 91T-like SN, and SN Iax. There are lines of IGEs, Ca II, and O I in the spectra of the 0.6 $M_\odot$ model. The 0.6 $M_\odot$ model exceptionally shows clear Si II and S II lines among our 5 models. This is caused by the large masses of Si and S in the 0.6 $M_\odot$ model. Compared with the observed thermonuclear transients, however, the IME lines are weaker than them. The absorption velocity of the Si II lines, $\simeq 6,000\,\mathrm{km\,s^{-1}}$, is relatively slower than that of normal SNe Ia, 91bg-like SNe, and 91T-like SNe, while being similar to some 02es-like SNe and some SNe Iax.

4.6 1.0 $M_\odot$ Model

Figure 4.21 shows the distribution of fallback/ejecta debris and ^{56}Ni at the end of the hydrodynamic simulation of the 1.0 $M_\odot$ model. The model is the case where the most violent thermonuclear explosions occur among our 5 models. The kinetic energy is the largest with 5.81×10^{50} erg, and the bulk velocity is also the largest with 16,400 $\mathrm{km\,s^{-1}}$.

Figure 4.22 shows the elemental abundance of the ejecta in the 1.0 $M_\odot$ model. Because of the large initial mass and violent thermonuclear explosions, the largest mass of ^{56}Ni, 0.49 $M_\odot$, is synthesized in the 1.0 $M_\odot$ model. The elemental abundance pattern is basically similar to the 0.6 $M_\odot$ model in the sense that Si is more dominant than Ca. Due to the more violent thermonuclear explosions, there are less C and O than the 0.6 $M_\odot$ model. The Si mass is also smaller than the 0.6 $M_\odot$ model because incomplete burning with moderate density and temperature yielding Si is inefficient in the 1.0 $M_\odot$ model with the most violent thermonuclear explosions.

The multi-band light curves of the 1.0 $M_\odot$ model are shown in Figure 4.4 and Figure 4.23. The variety of photometric properties caused by the viewing angle effect is shown in Figure 4.2 and Figure 4.3. It is the brightest model among our 5 models, reflecting the largest ^{56}Ni mass. Its B-band light curve is similar to a 91T-like SN1991T,

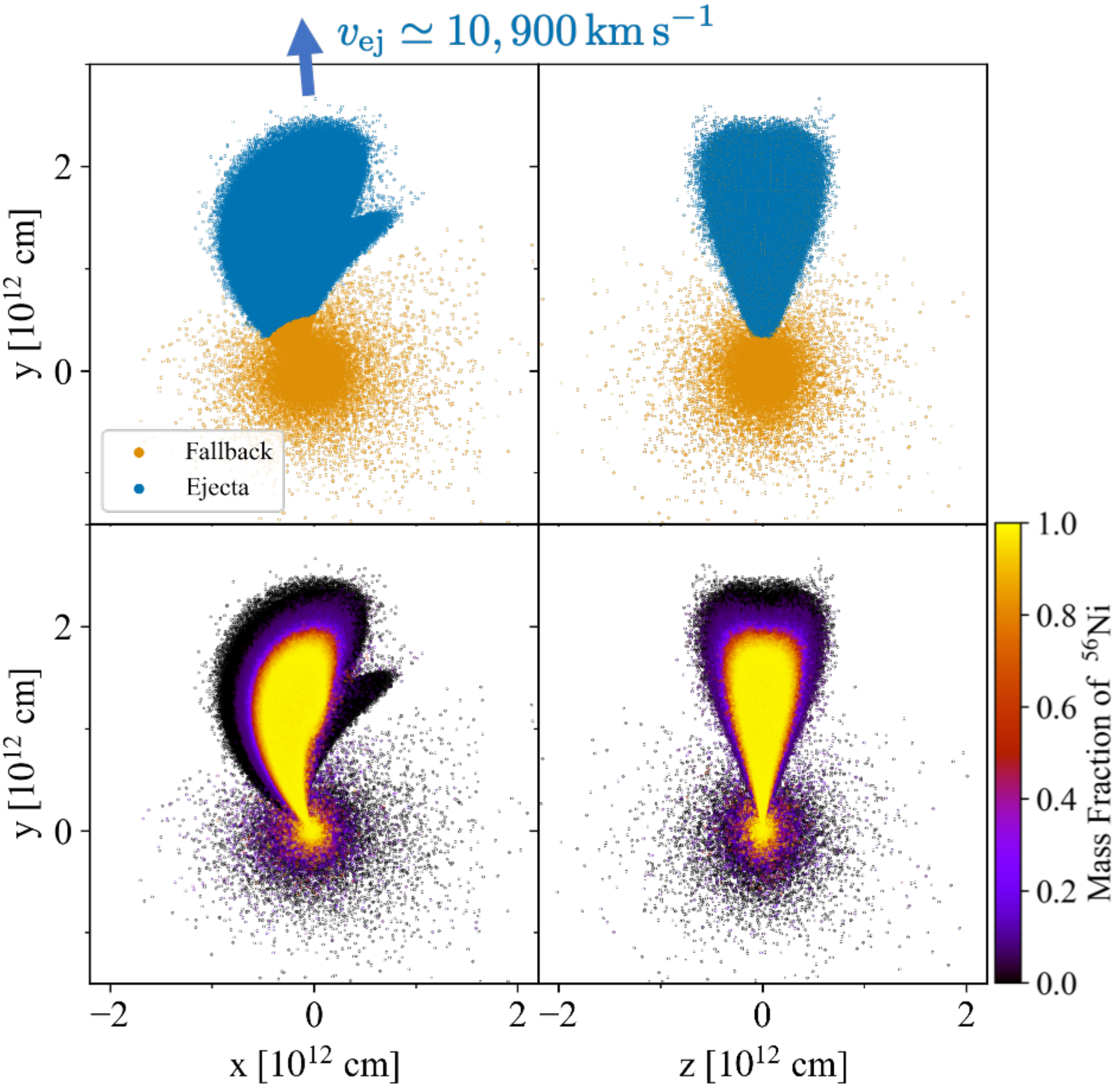

Figure 4.17: Same as Figure 4.6 for the 0.6 $M_\odot$ model.

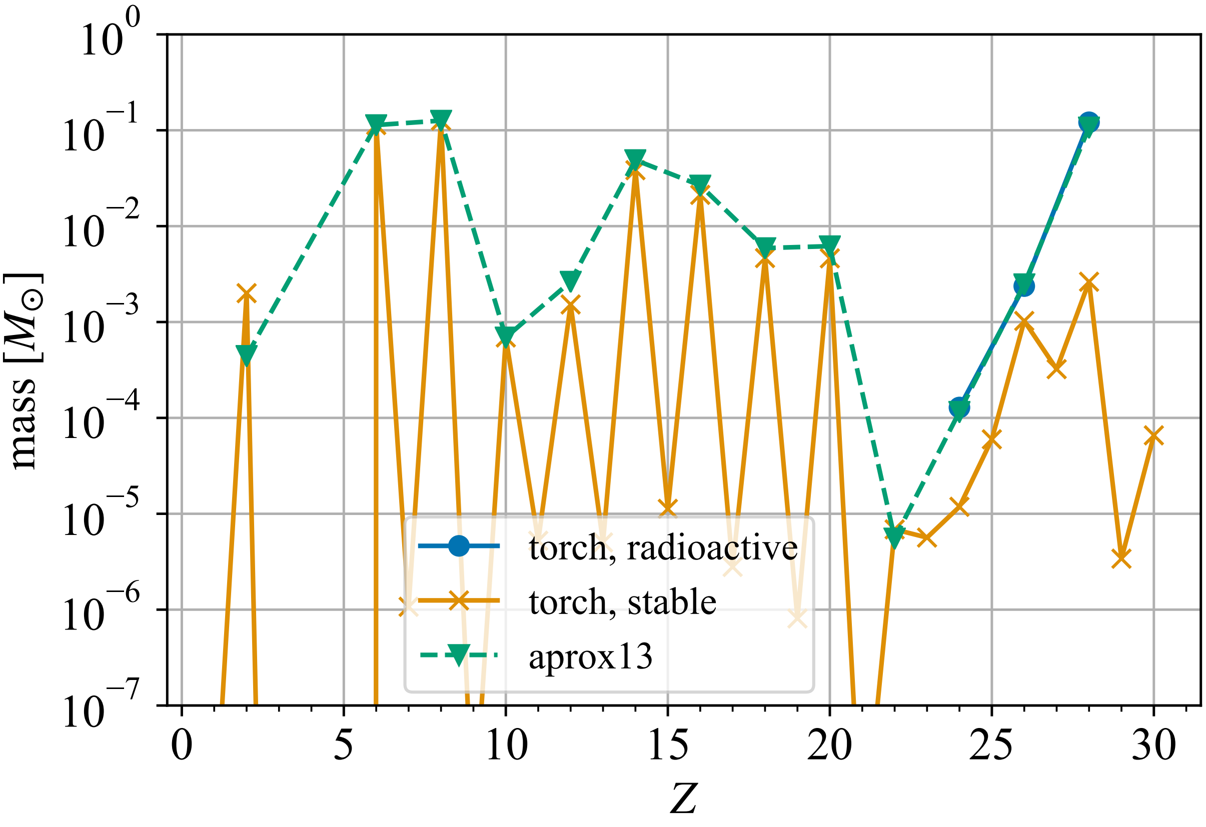

Figure 4.18: Same as Figure 4.7 for the 0.6 M$_\odot$ model.

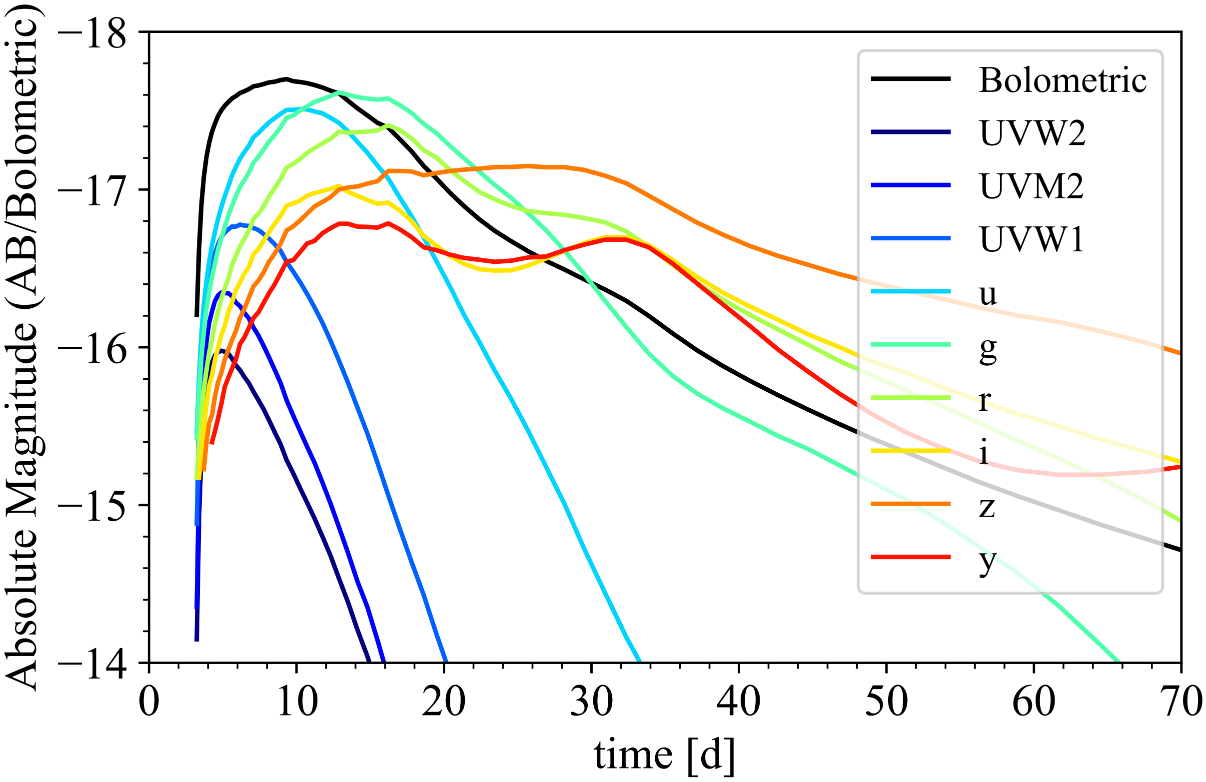

Figure 4.19: Same as Figure 4.8 for the 0.6 M$_\odot$ model.

and a normal SN Ia SN2011fe. However, in redder bands of VRI, the 1.0 M$_\odot$ model is fainter around the B-band peak.

Figure 4.24 shows the spectral evolution of the 1.0 M$_\odot$ model and the comparison of it with a normal SN Ia, 02es-like SN, 91bg-like SN, 91T-like SN, and SN Iax. As same as the 0.6 M$_\odot$ model, the 1.0 M$_\odot$ model shows lines of IGEs, Ca II, and O I, while lines of IMEs are almost absent. The lack of IME lines is a clear difference between the 1.0 M$_\odot$ model and the observed thermonuclear transients. Another difference is that the line width of the model is broader than theirs.

4.7 1.2 M$_\odot$ Model

Figure 4.25 shows the distribution of fallback/ejecta debris and ^{56}Ni at the end of the hydrodynamic simulation of the 1.2 M$_\odot$ model. The mass of the unbound ejecta is the largest with 0.775 M$_\odot$ among our 5 models, which is caused by the most massive initial WD. The thermonuclear explosions are less violent than the 1.0 M$_\odot$ model, resulting in the kinetic energy of 4.14×10^{50} erg and the bulk velocity of 13,400 km s^{-1}.

Figure 4.26 shows the elemental abundance of the ejecta in the 1.2 M$_\odot$ model. The ^{56}Ni mass is 0.27 M$_\odot$, which is less than that of the 1.0 M$_\odot$ model (0.27 M$_\odot$), reflecting the less violent thermonuclear explosions of the 1.2 M$_\odot$ model. The elemental abundance pattern is similar to the 0.6 and 1.0 M$_\odot$ models, because they share the same initial

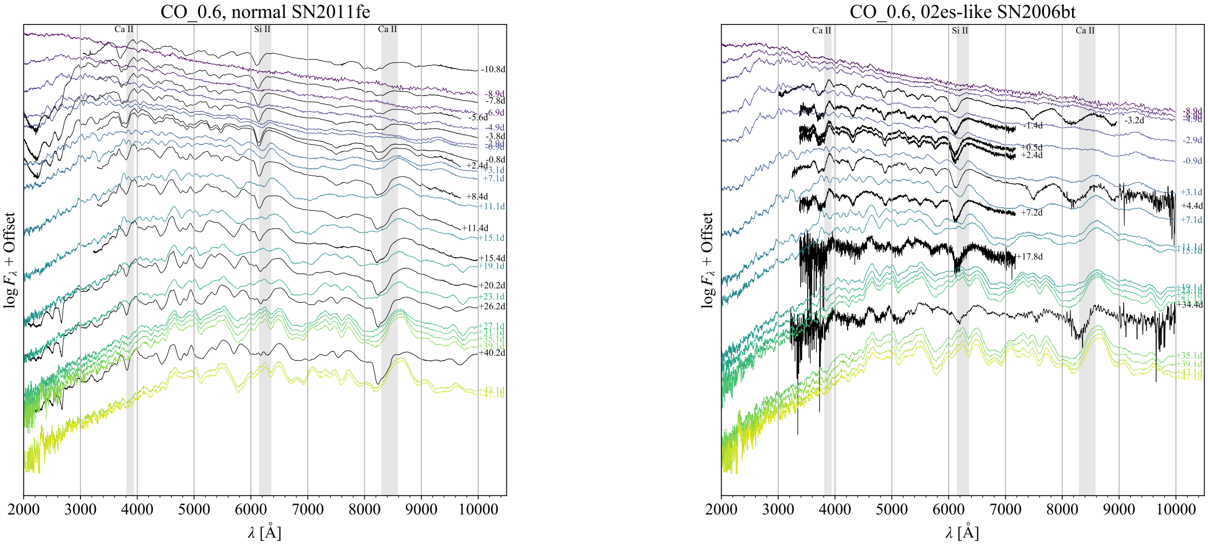

(a) SN2011fe (normal)

(b) SN2006bt (02es-like)

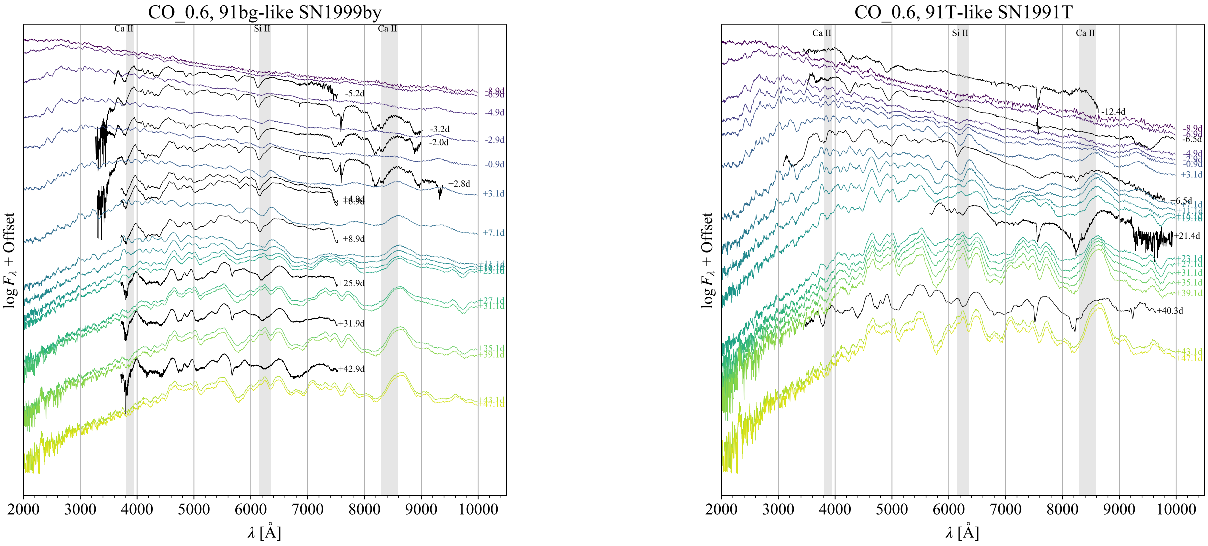

(c) SN1999by (91bg-like)

(d) SN1991T (91T-like)

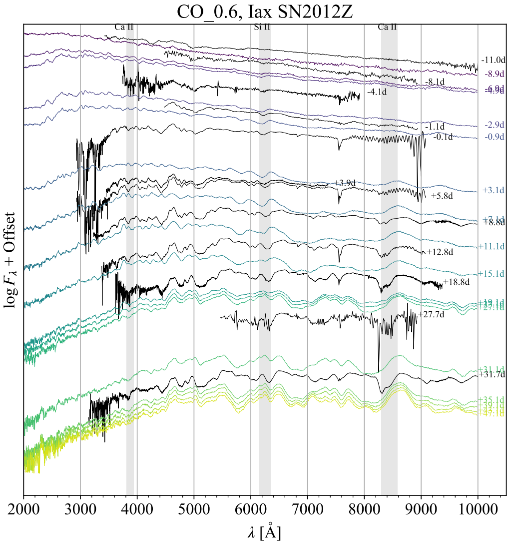

(e) SN2012Z (Iax)

Figure 4.20: Same as Figure 4.16 except for that here we compare the 0.6 $M_\odot$ model spectra with the observed thermonuclear transients shown in the sub-captions respectively.

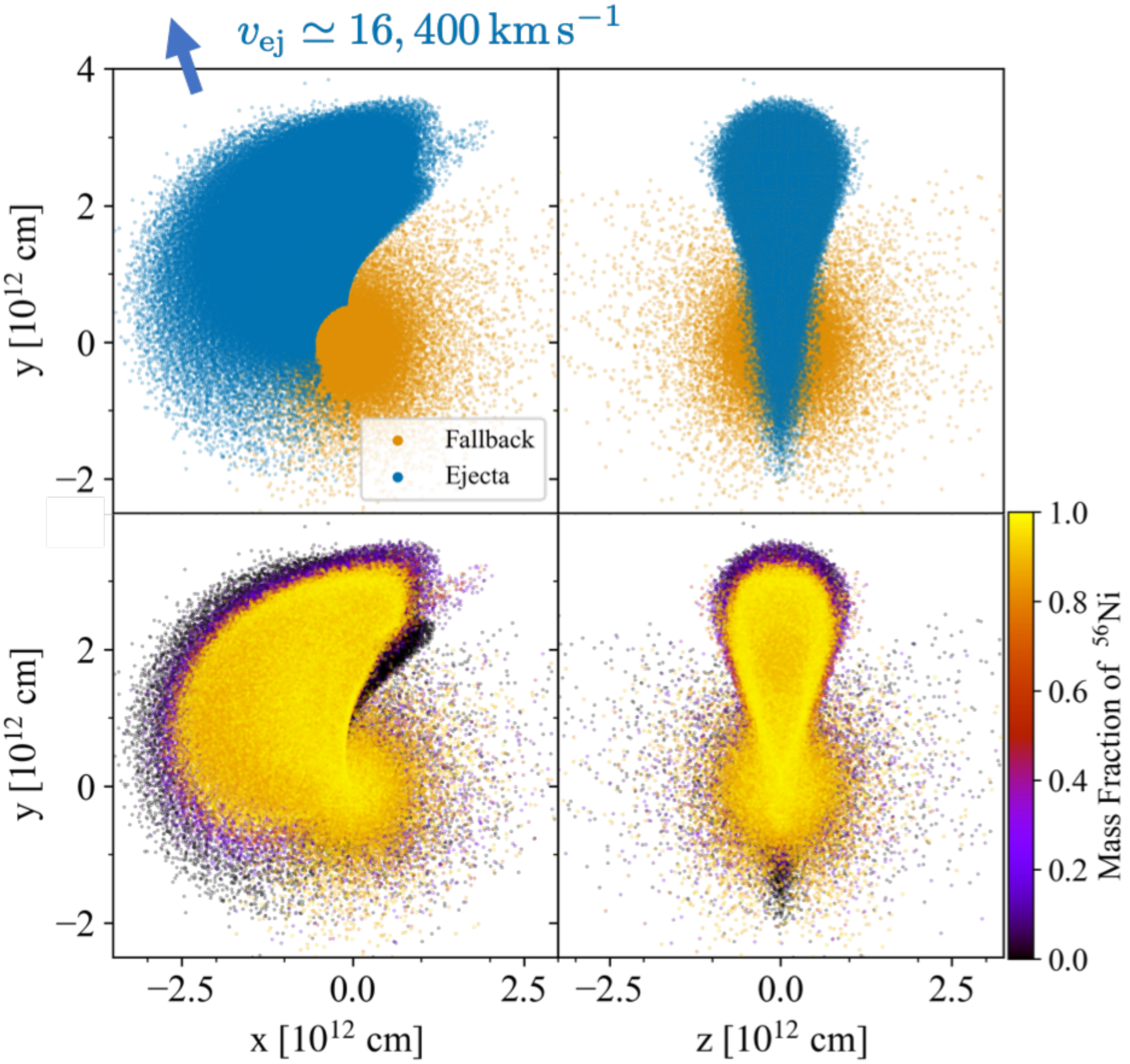

Figure 4.21: Same as Figure 4.6 for the 1.0 $M_\odot$ model.

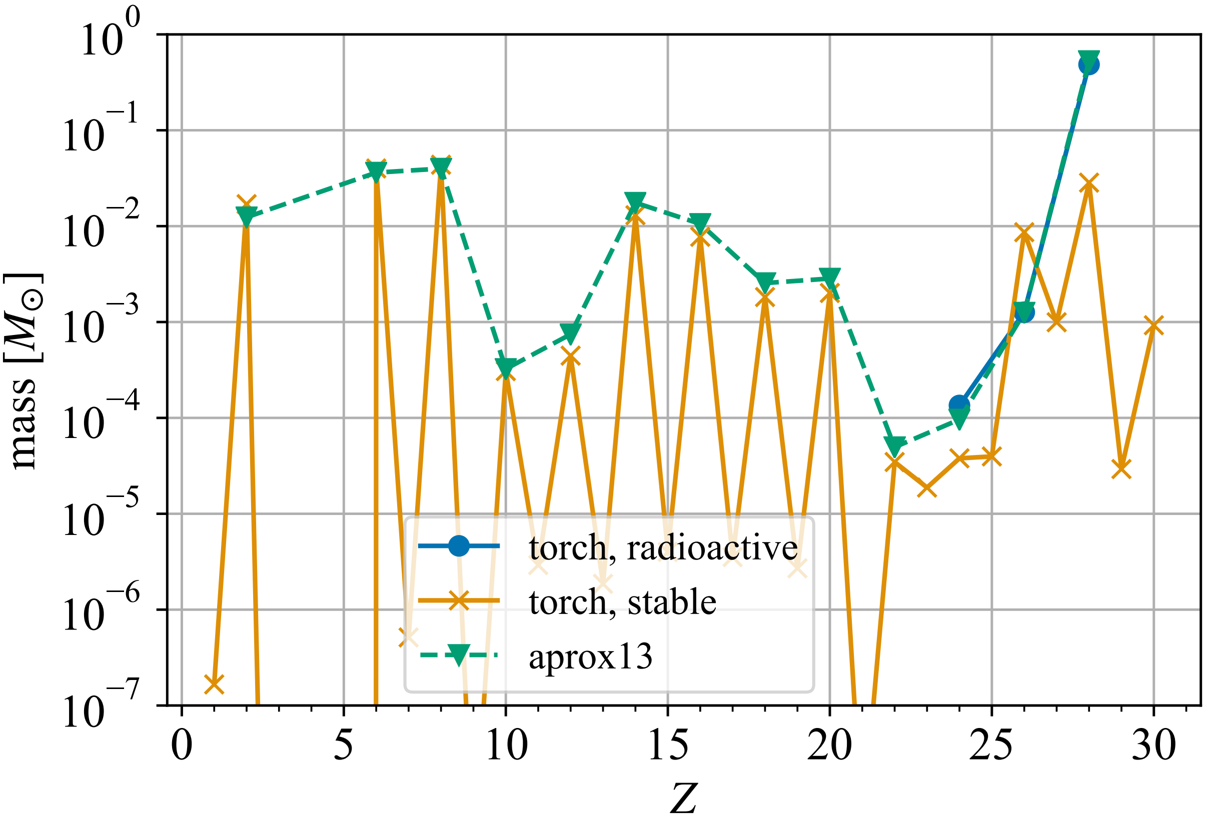

Figure 4.22: Same as Figure 4.7 for the 1.0 M$_\odot$ model.

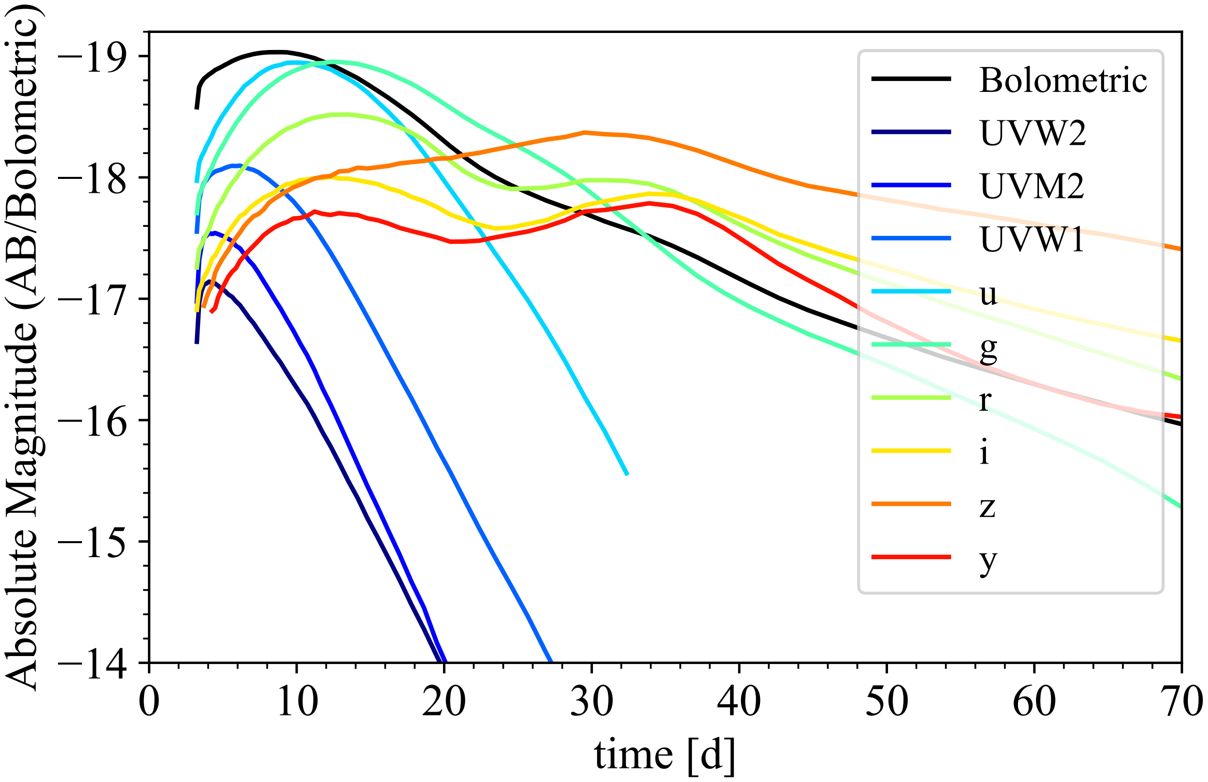

Figure 4.23: Same as Figure 4.8 for the 1.0 M$_\odot$ model.

nuclear composition.

The multi-band light curves of the 1.2 M$_\odot$ model are shown in Figure 4.4 and Figure 4.27. The variety of photometric properties caused by the viewing angle effect is shown in Figure 4.2 and Figure 4.3. The peak *B*-band magnitude is similar to a 02es-like SN2006bt and a 91T-like SN2000cx. However, the model declines faster than those SNe, and is fainter than them in redder bands of *VRI* around the *B*-band peak.

Figure 4.28 shows the spectral evolution of the 1.2 M$_\odot$ model and the comparison of it with a normal SN Ia, 02es-like SN, 91bg-like SN, 91T-like SN, and SN Iax. The spectra of the 1.2 M$_\odot$ model are very similar to those of the 1.0 M$_\odot$ model in the following points: the appearance of lines of IGEs, Ca II, and O I, the absence of IME lines, broader line width compared with the observed thermonuclear transients.

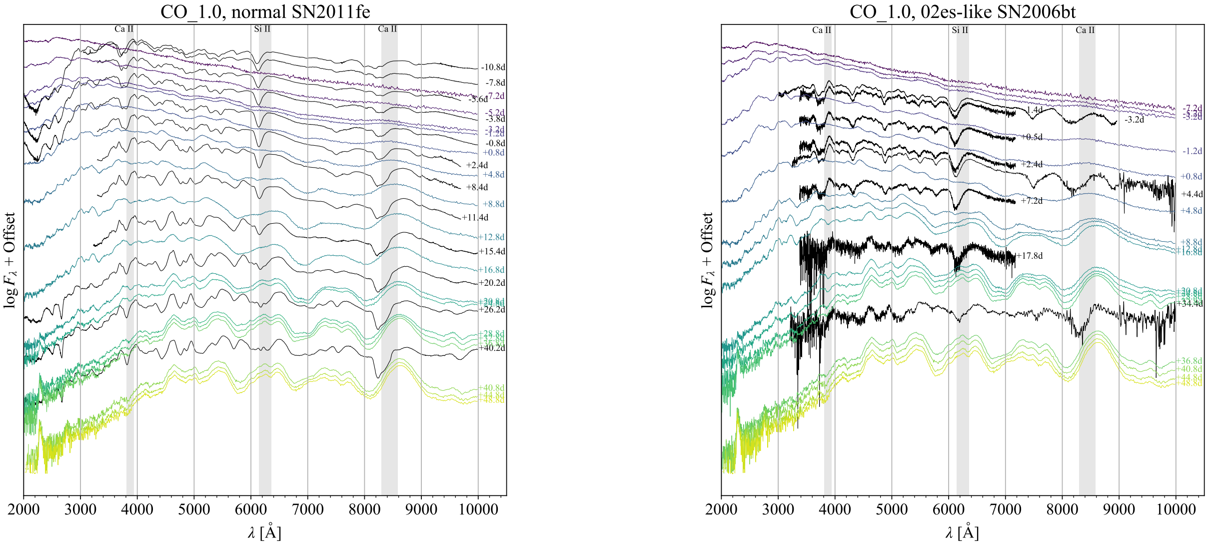

(a) SN2011fe (normal)

(b) SN2006bt (02es-like)

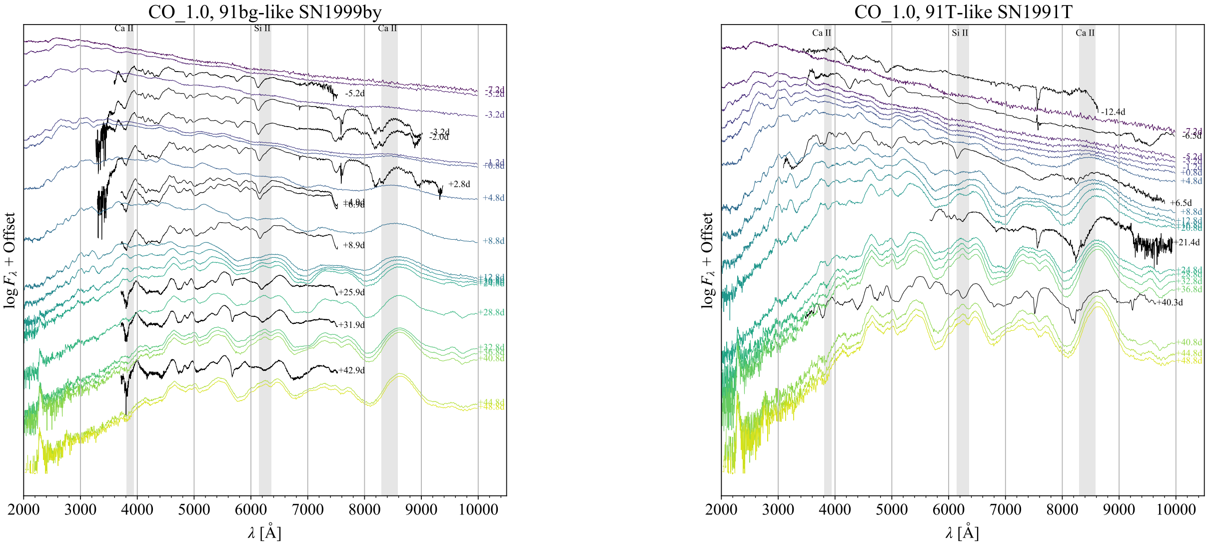

(c) SN1999by (91bg-like)

(d) SN1991T (91T-like)

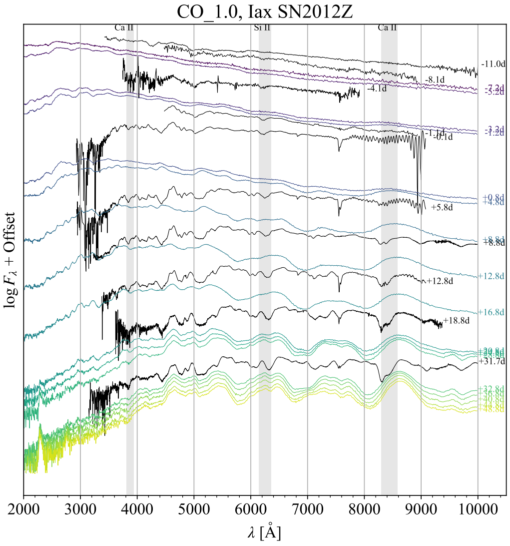

(e) SN2012Z (Iax)

Figure 4.24: Same as Figure 4.24 except for that here we compare the 1.0 $M_\odot$ model.

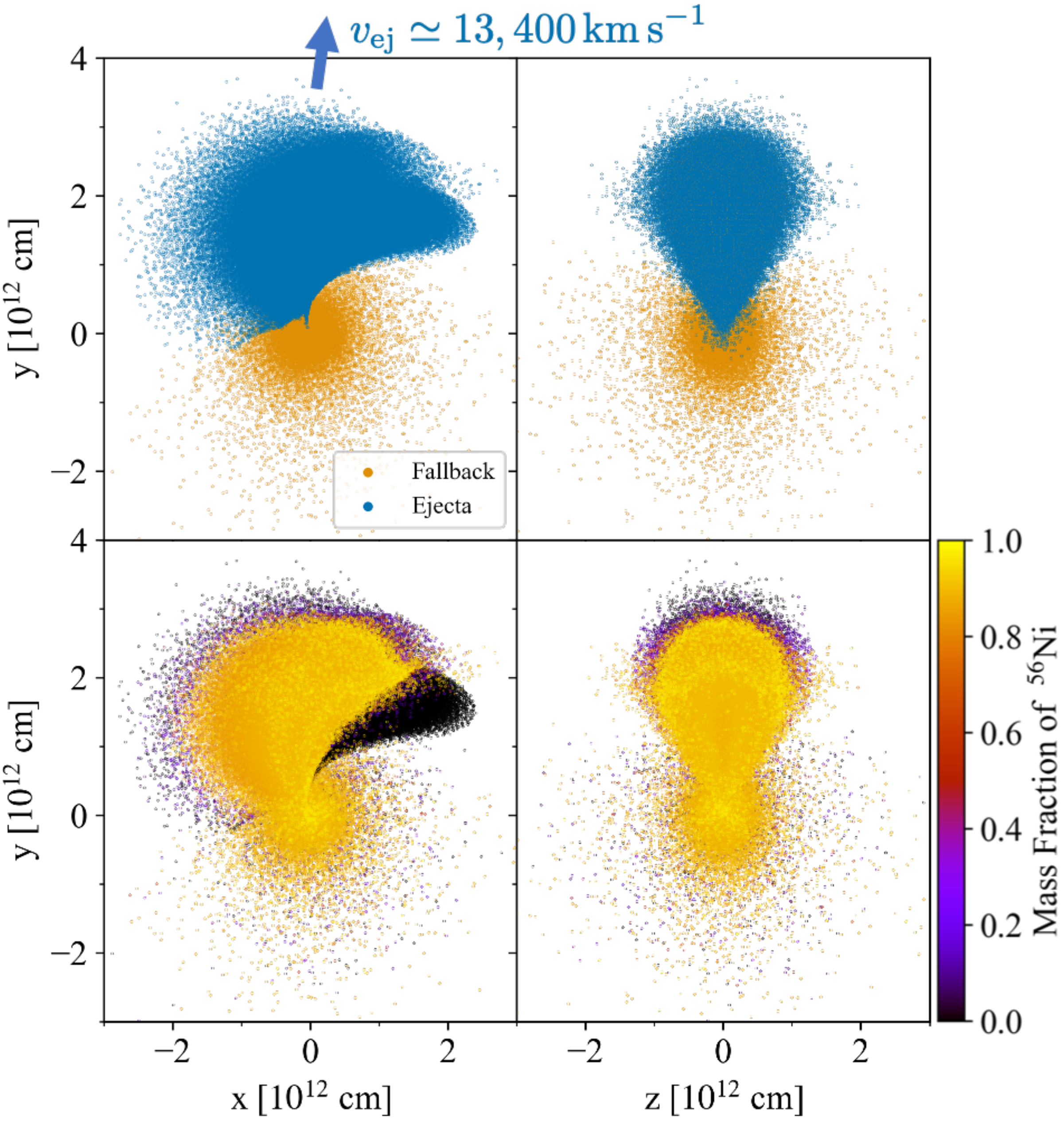

Figure 4.25: Same as Figure 4.6 for the 1.2 $M_\odot$ model.

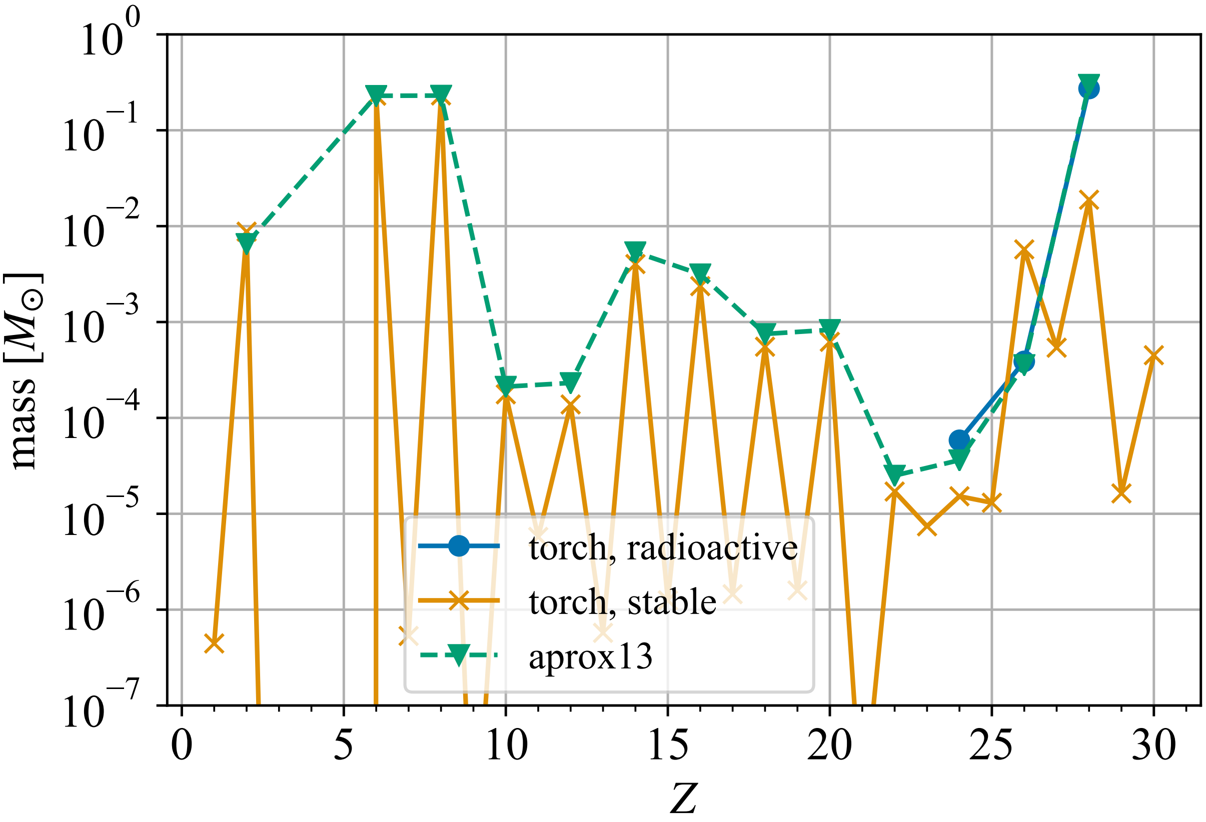

Figure 4.26: Same as Figure 4.7 for the 1.2 $M_\odot$ model.

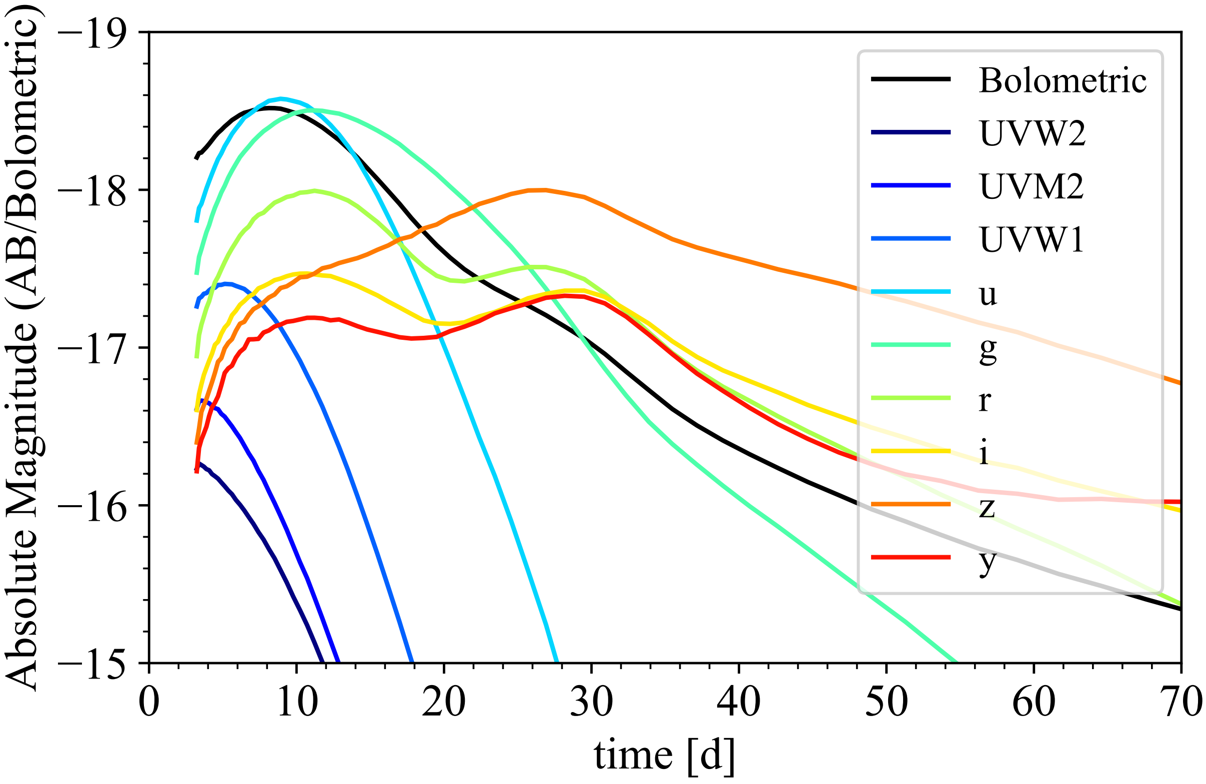

Figure 4.27: Same as Figure 4.8 for the 1.2 M$_\odot$ model.

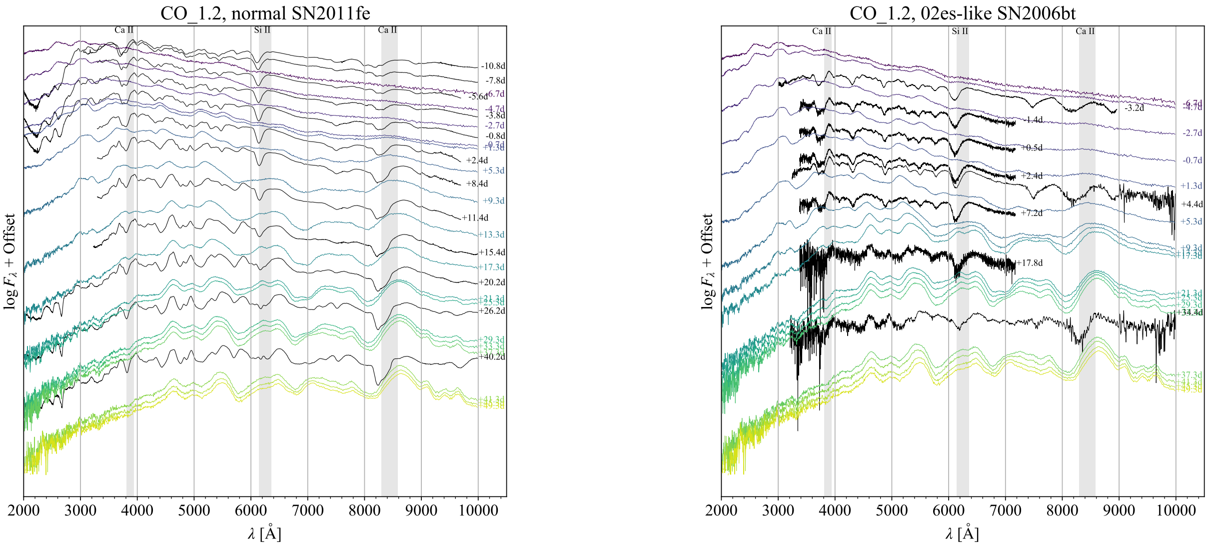

(a) SN2011fe (normal)

(b) SN2006bt (02es-like)

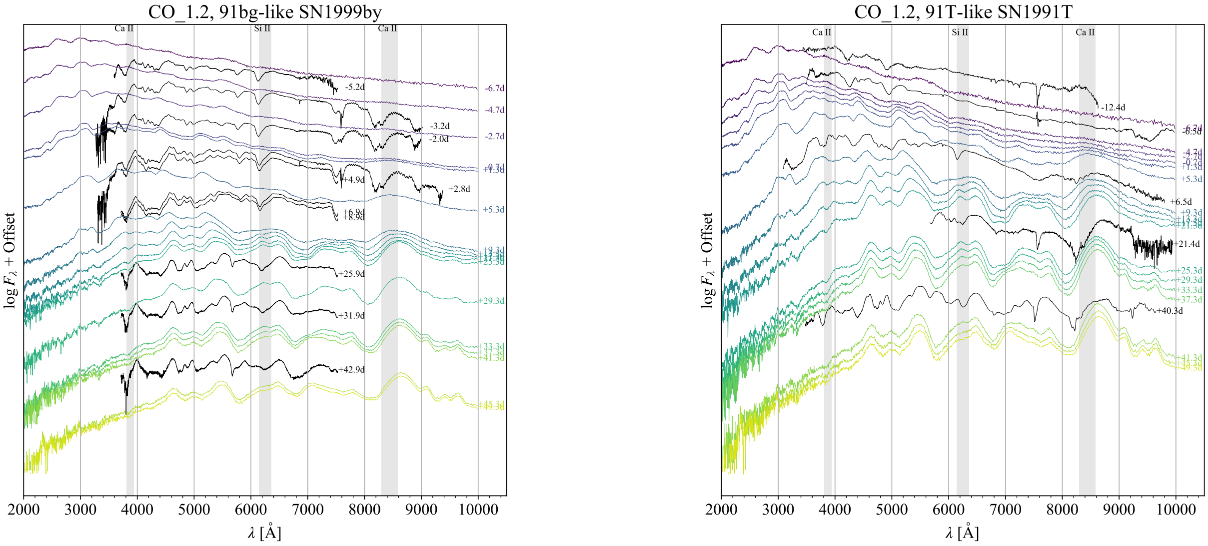

(c) SN1999by (91bg-like)

(d) SN1991T (91T-like)

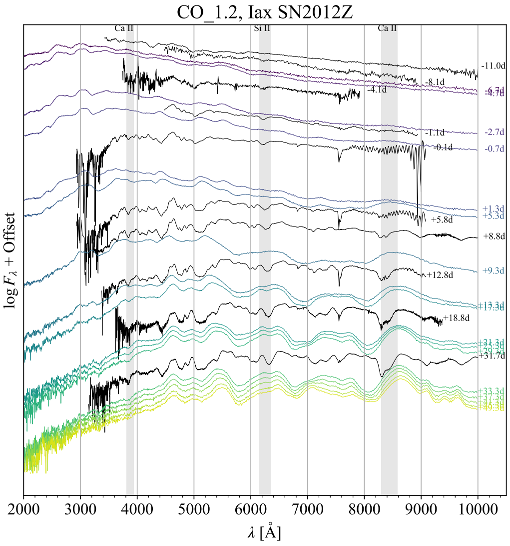

(e) SN2012Z (Iax)

Figure 4.28: Same as Figure 4.20 except for that here we compare the 1.2 $M_\odot$ model.

Chapter 5

Discussions

5.1 Variety of Observational Signatures

In Chapter 4, we derive synthetic observational signatures for the 5 parameter sets of WD TDEs. The phase space of photometric properties of our models cover a wide space (see Figure 4.2 and Figure 4.3). However, there could be a more variety of them because the intrinsic parameter sets of WD TDEs ($M_{\rm WD}$, $M_{\rm BH}$, β) can vary over a wider parameter space than our parameter sets (see Figure 2.3). Here we discuss the possible range of the variety of observational signatures of WD TDEs.

Peak time and peak luminosity of transients are basic photometric properties of transients, and are derived in our models. The Arnett rule (Arnett, 1982) gives simple analytic formulae to estimate them. Assuming the spherical symmetry and that a transient is purely powered by the radioactive decay of ^{56}Ni and the energy is deposited in the center of the transient, we can approximately estimate the peak time as

$$t_{\rm peak} \simeq 16\,{\rm d} \left(\frac{\kappa}{0.1\,{\rm cm^2\,g^{-1}}}\right)^{1/2} \left(\frac{M_{\rm ej}}{{\rm M_\odot}}\right)^{1/2} \left(\frac{v_{\rm ph}}{10^9 {\rm cm\,s^{-1}}}\right)^{-1/2}, \tag{5.1}$$

where we take fiducial value of the opacity κ as $0.1\,{\rm cm^2\,g^{-1}}$, $M_{\rm ej}$ is the ejecta mass, and $v_{\rm ph}$ is the photospheric velocity. The peak luminosity powered by the radioactive decay of ^{56}Ni is (Equation (1) in Moriya et al., 2018, and see references therein)

$$L_{\rm peak} \simeq L_{\rm 56Ni}(t = t_{\rm peak}) \tag{5.2}$$

$$\simeq 10^{43}\,{\rm erg\,s^{-1}} \left[6.48 \exp\left(-\frac{t_{\rm peak}}{8.76\,{\rm d}}\right) + 1.44 \exp\left(-\frac{t_{\rm peak}}{111.42\,{\rm d}}\right)\right] \left(\frac{M_{\rm 56Ni}}{{\rm M_\odot}}\right), \tag{5.3}$$

We apply these equations to the results of our hydrodynamic and nucleosynthesis simulations with an approximation that the photospheric velocity is the same as the ejecta velocity $v_{\rm ej} = (2E_{\rm kin}/M_{\rm ej})^{1/2}$. Then we compare the peak time and peak luminosity given by the Arnett rule and by our models in Figure 5.1. The mean of peak time and peak luminosity of our models over all the viewing angles match those of the Arnett rule within a factor of about 1.5 (see Figure 5.2). Thus, the Arnett rule gives a reasonable estimation for the peak time and peak luminosity of emission from thermonuclear explosions in WD TDEs, although there is a large variety of them due to the viewing angle effect.

The peak time of the 0.6, 1.0, and 1.2 $\mathrm{M}_{\odot}$ models given by our numerical simulations is smaller than that given by the Arnett rule. This is because the ejecta shapes are very aspherical and thus a ratio of surface area to volume is larger than a spherical shape, which is assumed in the Arnett rule. In contrast, the peak time of the 0.2 and 0.4 $\mathrm{M}_{\odot}$ models given by the simulations is larger than that given by the Arnett rule, although the ejecta shapes of these models are also aspherical. A reason is that we choose a larger initial time of the radiative transfer simulations for these models than the other models (see Table 3.1). Because we assume that nuclear energy released before the initial time is completely absorbed by the ejecta (see Section 3.4.1), this choice makes escapes of photons less efficient, and thus would result in the larger peak time. Another reason for the 0.4 $\mathrm{M}_{\odot}$ model is that the temperature in the pre-peak phase is larger than the other models (see Figure 4.5). Opacity is larger than the fiducial value used in Equation (5.1) in such a case (Swartz, 1991), which leads to the larger peak time than the estimated peak time given by Equation (5.1).

The reasonable match between the numerical simulations and the Arnett rule motivates us to study the thermonuclear emission from WD TDEs over a larger parameter space with a less expensive computational cost: we apply the Arnett rule to the results of a variety of hydrodynamic simulations performed in Kawana et al. (2018) (see Figure 2.3) and derive the peak time and peak luminosity. Figure 5.3 shows the results. We see that there could be fainter ($10^{38}\,\mathrm{erg\,s^{-1}} \lesssim L_{\mathrm{peak}} \lesssim 10^{42}\,\mathrm{erg\,s^{-1}}$) and slower emission than that of our 5 models. They arise from WD TDEs with weaker thermonuclear explosions, where less ^{56}Ni is synthesized and slower expansions of the ejecta are realized. Thus, such faint transients should also be considered as candidates of WD TDEs. Note that Kawana et al. (2018) explore the parameter space of $\beta \leq 6$ for the He $0.2\,\mathrm{M}_{\odot}$ WD, and of $\beta \leq 5$ for the CO $0.6\,\mathrm{M}_{\odot}$ WD and ONeMg $1.2\,\mathrm{M}_{\odot}$ WD. There could be brighter emission if we consider higher β, although they are relatively rare than the lower β cases (see Equation (2.50)).

There would also be a more variety of spectroscopic features than those shown in our 5 models. Absorption velocities could be larger(smaller) if the thermonuclear explosions are stronger(weaker) than our models and thus the unbound ejecta have more(less) kinetic energy. However, we expect that which atomic lines are present/absent is not significantly affected by M_{BH} or β but by M_{WD}, or the initial composition of the WD. This is because nucleosynthesis dominantly depends on the initial composition of the WD (Kawana et al., 2018). Additionally, the Doppler shift due to the bulk motion of the unbound ejecta, which is the most important spectroscopic feature of WD TDEs, is common among all the WD TDEs although it depends on the viewing angle.

5.2 Emission from Fallback Debris

In this study, we focus on emission from the unbound ejecta powered by the thermonuclear explosions. There could be another power source: the bound debris falling back on to the BH. In this Section, we discuss which emission dominates over the other. It is naively

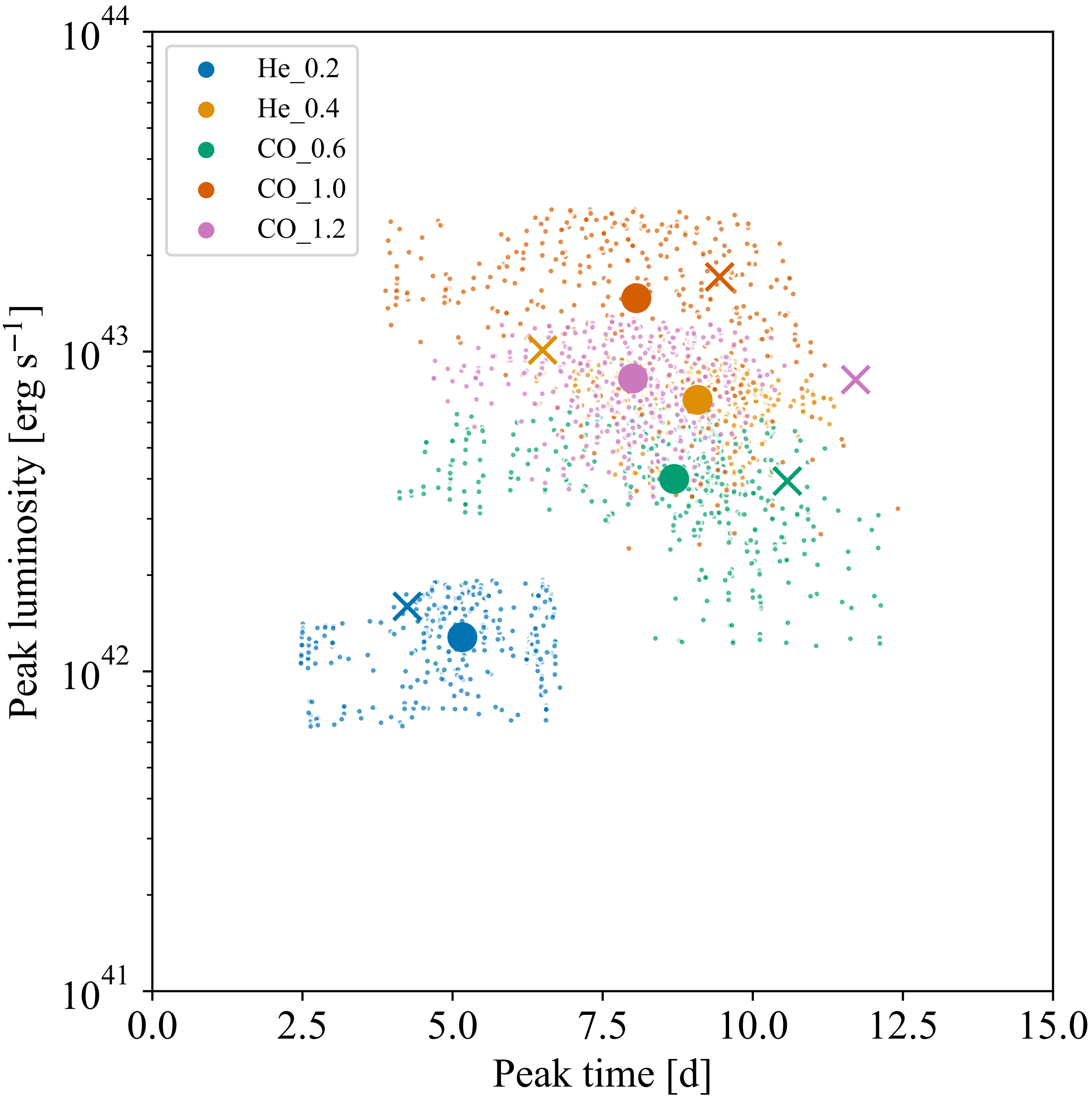

Figure 5.1: Comparisons between peak time and peak luminosity given by our models and those given by the Arnett rule (Arnett, 1982). The small circles show those of our models, where we consider various viewing angles $(\cos\theta, \phi)$ equally sampled with $(20, 20)$ bins. The large circles show the mean of them. The crosses show the peak time and peak luminosity given by the Arnett rule, where the ejecta mass, ^{56}Ni mass, and ejecta velocity are taken from our hydrodynamic and nucleosynthetic results.

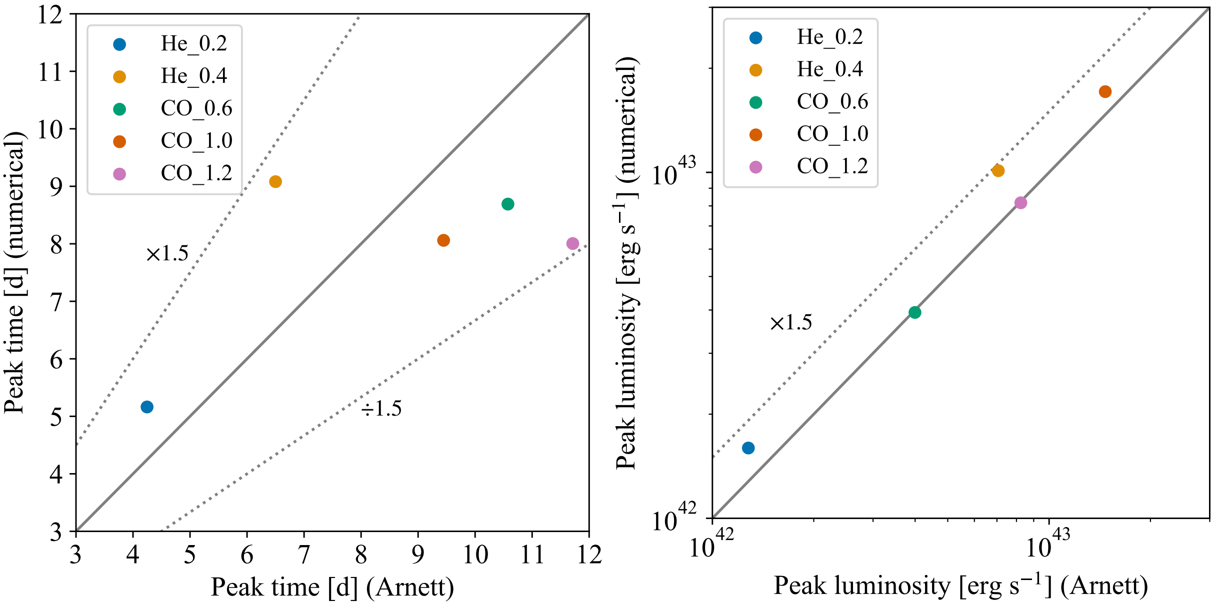

Figure 5.2: Difference between peak time t_{peak} and peak luminosity L_{peak} given by our models and those given by the Arnett rule (Arnett, 1982). The horizontal axes of the left and right panel respectively show t_{peak} and L_{peak} estimated by the Arnett rule, corresponding to the crosses in Figure 5.1. The vertical axes of the left and right panel respectively show the mean of the peak time and peak luminosity given by our numerical simulations over all the viewing angles, corresponding to the large circles in Figure 5.1. On the solid lines the values estimated by the Arnett rule and our numerical simulations are same. The dotted lines show ×1.5 or ÷1.5 of the solid lines.

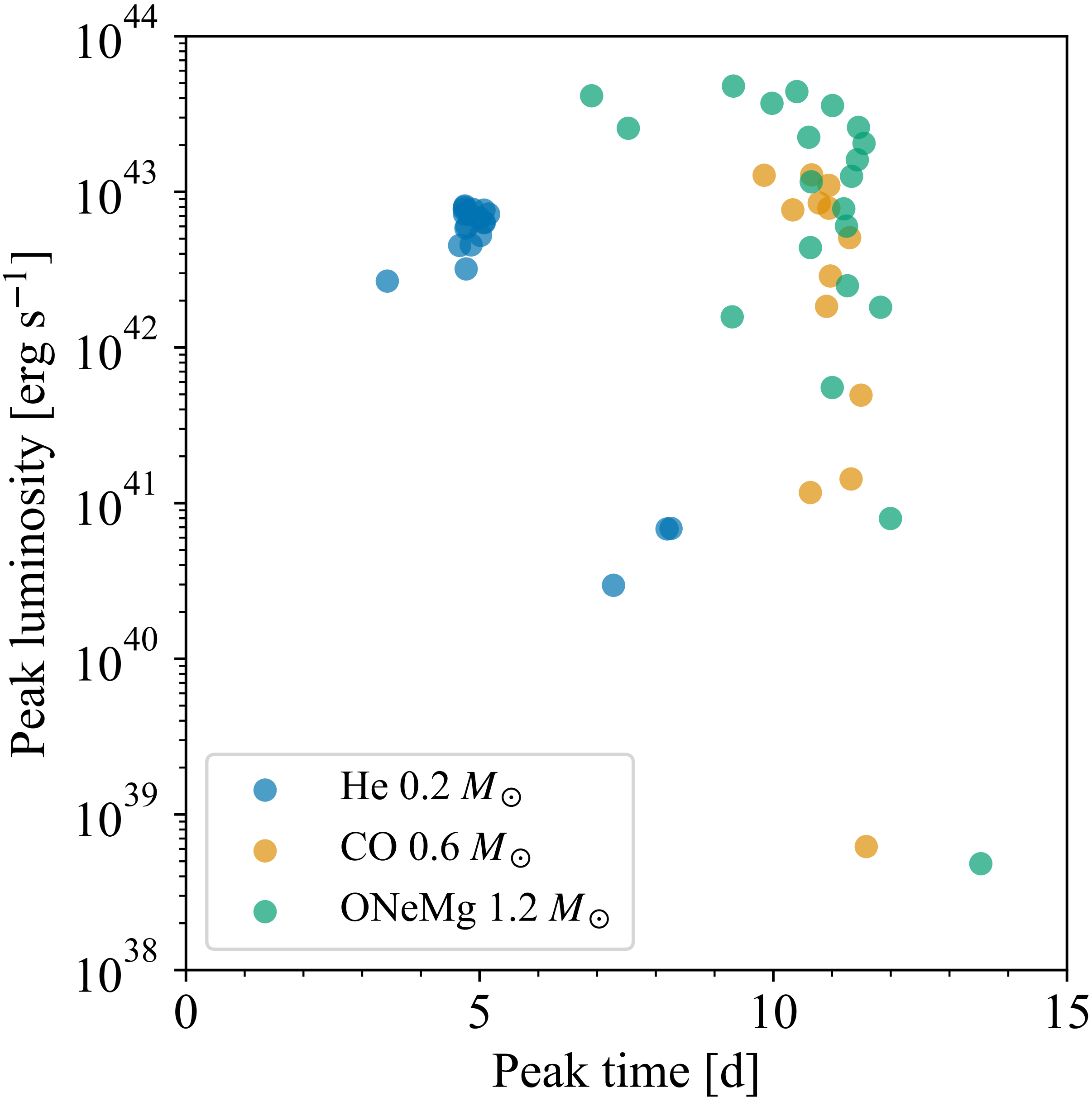

Figure 5.3: Peak time and peak luminosity given by the Arnett rule (Arnett, 1982) and hydrodynamic results of Kawana et al. (2018). Each point represents a parameter set of ($M_{\rm WD}$, $M_{\rm BH}$, β). Note that there would be an additional variety in the peak time and peak luminosity due to the viewing angle effect (see Figure 5.1).

expected that the luminosity from the fallback debris follows the mass fallback rate, as we review in Section 2.1.1 and as observed MS TDEs show (see Section 2.1.2). With that expectation, we can make a rough estimation of the fallback luminosity with the mass fallback rate as

$$L_{\rm fb} \sim \eta \dot{M}_{\rm fb} c^2 \tag{5.4}$$

$$\sim 10^{50}\,{\rm erg\,s^{-1}} \left(\frac{t}{10^2\,{\rm s}}\right)^{-5/3} \left(\frac{\eta}{0.1}\right) \left(\frac{\dot{M}_{\rm fb,p}}{10^{-3}\,{\rm M_\odot\,s^{-1}}}\right) \left(\frac{t_{\rm fb}}{10^2\,{\rm s}}\right)^{5/3}, \tag{5.5}$$

where η is the conversion efficiency. We estimate the peak mass fallback rate $\dot{M}_{\rm fb,p}$ and fallback timescale $t_{\rm fb}$ from the results of the hydrodynamic simulations (see also Figure 5.4). This fallback luminosity is larger than the luminosity of thermonuclear emission $L_{\rm therm} \simeq 10^{42}$–$10^{43}\,{\rm erg\,s^{-1}}$ around its peak $t \simeq 10$ days. However, the thermonuclear emission can be dominant if the fallback emission is limited by the Eddington luminosity,

$$L_{\rm Edd} \simeq 1.6 \times 10^{41}\,{\rm erg\,s^{-1}} \left(\frac{\kappa}{0.1\,{\rm cm^2\,g^{-1}}}\right)^{-1} \left(\frac{M_{\rm BH}}{10^{2.5}\,{\rm M_\odot}}\right). \tag{5.6}$$

Note that we show the Eddington luminosity in a different formula in Equation (2.29), where the complete ionization is assumed. We adopt Equation (5.6) here because the burnt ash is rich in heavy nuclei and thus the assumption of the complete ionization is invalid. We see $L_{\rm Edd} \ll L_{\rm therm} < L_{\rm fb}$ at $t \sim 10$ d, where $L_{\rm therm}$ is the bolometric luminosity of the emission from the unbound ejecta. It is expected that super-Eddington emission from the fallback debris is observed only when relativistic jets are formed and are viewed on-axis (e.g. MacLeod et al. 2016). In addition, if an accretion disk is formed from the fallback debris and emits thermal emission, its temperature would be $\sim 10^6$ K (Miller, 2015; MacLeod et al., 2016). In the optical wavelength, the disk thermal emission would be much smaller than the thermonuclear emission. Thus we expect the observational signatures we derive in this study is not significantly affected by the fallback emission in most cases. Still the fallback emission is of interest in the sense that relativistic jets would form from the fallback debris and the emission would be main counterparts of WD TDEs observed in X-ray (see Section 2.2.3).

5.3 Implications for IMBH Properties

We find two observed candidates of WD TDEs, which are rapid and faint transients showing similar multi-band light curves with our $0.2\,{\rm M_\odot}$ model (see Section 4.3). If they are really counterparts from thermonuclear explosions in WD TDEs, they bring us insights into the event rate of WD TDEs, and thus on the IMBH number density (see Section 2.2.2). A volumetric event rate of each event $\dot{n}$ is calculated as (Drout et al., 2014; Tampo et al., 2020)

$$\dot{n} = \frac{1+z}{\epsilon T V_{\rm max}}, \tag{5.7}$$

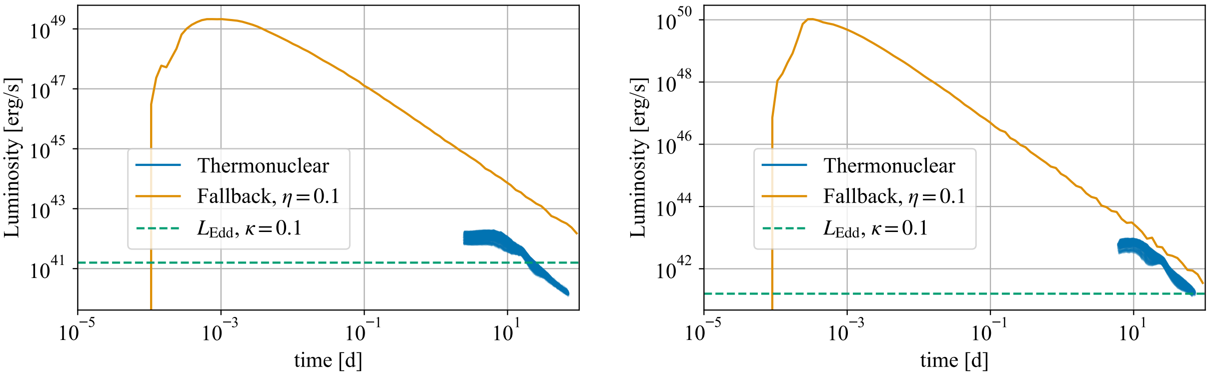

(a) The 0.2 $\mathrm{M}_\odot$ model (b) The 0.4 $\mathrm{M}_\odot$ model

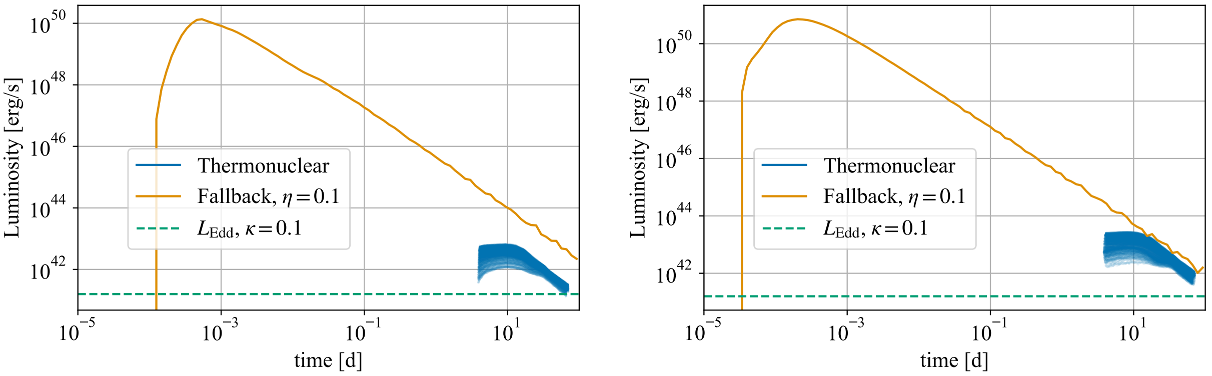

(c) The 0.6 $\mathrm{M}_\odot$ model (d) The 1.0 $\mathrm{M}_\odot$ model

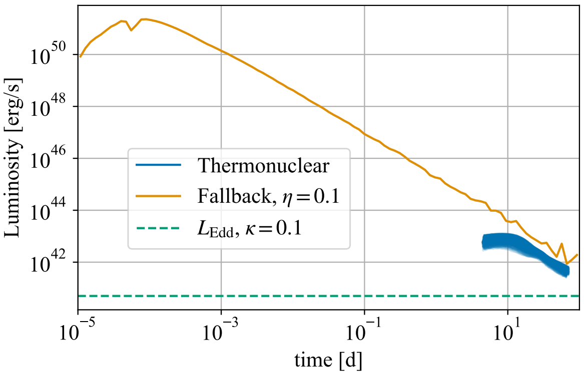

(e) The 1.2 $\mathrm{M}_\odot$ model

Figure 5.4: Comparisons of thermonuclear luminosity, fallback luminosity, and the Eddington luminosity of our models. We calculate the mass fallback rate with Equation (2.19), and obtain the orbital energy distribution $\mathrm{d}M/\mathrm{d}\epsilon$ from the hydrodynamic simulations. We assume the conversion efficiency from mass to luminosity as $\eta = 0.1$. We assume that the opacity κ as $0.1\,\mathrm{cm}^2\,\mathrm{g}^{-1}$ to calculate the Eddington luminosity. For the thermonuclear luminosity, we consider various viewing angles $(\cos\theta, \phi)$ equally sampled with $(20, 20)$ bins.

where z is the redshift of the event, ϵ is the efficiency to detect the transient and is assumed to be unity, T is the survey duration of 600 d, and $V_{\rm max}$ is the comoving volume in which the transient can be detected. Table 5.1 shows the redshifts, $V_{\rm max}$, and the derived event rates ($V_{\rm max}$ is given in Pursiainen, 2020). Then we estimate the event rate of WD TDEs with thermonuclear explosions as $\sim 600\,{\rm Gpc}^{-3}\,{\rm yr}^{-1}$. Note that the estimated event rate can be smaller if the two candidates of WD TDEs do not originate from WD TDEs in real, and also can be larger if we find other WD TDE candidates. We also estimate the rate of total WD TDEs including both with and without thermonuclear explosions multiplying the former rate by the minimum penetration parameter needed to ignite the explosions, or $\beta_{\rm thermo}$. We take $\beta_{\rm thermo} \simeq 5$ for He WD TDEs (Kawana et al., 2018), and then we obtain the total WD TDE rate as $\sim 3 \times 10^3\,{\rm Gpc}^{-3}\,{\rm yr}^{-1}$. Substituting the event rate in Equation (2.70), we obtain the number density of IMBHs as

$$n_{\rm IMBH} \sim 3\,{\rm Mpc}^{-3} \left(\frac{\dot{n}_{\rm WD\,TDE,\,thermo}}{600\,{\rm Gpc}^{-3}\,{\rm yr}^{-1}}\right) \left(\frac{\dot{N}_{\rm WD\,TDE}}{10^{-6}\,{\rm yr}^{-1}\,{\rm BH}^{-1}}\right)^{-1} \left(\frac{\beta_{\rm thermo}}{5}\right), \tag{5.8}$$

where we take the intrinsic WD TDE rate per BH as $10^{-6}\,{\rm yr}^{-1}\,{\rm BH}^{-1}$, which is the estimated rate in centers of dwarf galaxies (MacLeod et al. 2014; see also Section 2.2.2).

Although our estimates of the WD TDE rate and the IMBH number density are not highly confident and there is large uncertainty in $\dot{N}_{\rm WD\,TDE}$ (see Section 2.2.2), it is valuable to check the consistency of the estimates with constraints given by previous studies. The total WD TDE rate estimated here, $\sim 3 \times 10^3\,{\rm Gpc}^{-3}\,{\rm yr}^{-1}$, is larger than those of $\sim 500\,{\rm Gpc}^{-3}\,{\rm yr}^{-1}$ and $\sim 50\,{\rm Gpc}^{-3}\,{\rm yr}^{-1}$ respectively estimated in Haas et al. (2012) and Shcherbakov et al. (2013) as the rates of WD TDEs in globular clusters. The discrepancies imply that environments of the WD TDE candidates would not be globular clusters but centers of dwarf galaxies. If dwarf galaxies mainly contribute to the WD TDE rate, the estimated IMBH number density implies a number density of dwarf galaxies, and we can check its consistency. If we assume an occupation fraction of IMBHs in centers of dwarf galaxies as unity, the number density of dwarf galaxies is estimated as the same as that of IMBHs, $\sim 3\,{\rm Mpc}^{-3}$, corresponding to ~ 100 dwarf galaxies per a Milky Way-like galaxy. The faint dwarf galaxies are difficult to be completely detected even around the Milky Way and thus their density is under debated (for a review see Bullock & Boylan-Kolchin, 2017). In the standard ΛCDM framework, which considers the dark energy and cold dark matter, it is predicted that there are ~ 1000 dark matter subhalos around the Milky Way, but only ~ 50 dwarf galaxies have been detected. A modification to the theoretical predictions is introduced to solve the mismatch and indicates ~ 100 dwarf galaxies around the Milky Way, which would be consistent with our estimate of the number density of dwarf galaxies. There is almost no constraint on the number density of IMBHs, except for the recent discovery of a $142\,{\rm M}_\odot$ BH as a remnant of a merger of stellar mass BHs (Abbott et al., 2020b). The inferred merger rate of such an event is $0.13^{+0.30}_{-0.11}{\rm Gpc}^{-3}\,{\rm yr}^{-1}$. If we naively integrate the merger rate over the Hubble time, we obtain the IMBH number density as $n_{\rm IMBH} \sim 2\,{\rm Mpc}^{-3}$. The number density should be regarded as a lower limit because IMBHs could be formed by other paths rather than the merger of stellar mass BHs, and thus the lower limit is consistent with our estimate.

Table 5.1: Volumetric event rates of observed WD TDE candidates found in our study. $V_{\max}$ is the comoving volume in which the transient can be detected.

name	redshift	$V_{\max}$ $[10^{-3}\,\mathrm{Gpc}^3]$	event rate $[\mathrm{Gpc}^{-3}\,\mathrm{yr}^{-1}]$
DES14S2plb	0.12	1.97	346
DES16S1dxu	0.13	2.90	237

We also discuss a possible implication on the mass distribution of MBHs given by the estimated IMBH number density. We adopt the mass distribution parametrized in MacLeod et al. (2016) as a power-law function extrapolated from SMBHs,

$$\frac{\mathrm{d}n_{\mathrm{IMBH}}}{\mathrm{d}\log M_{\mathrm{BH}}} = 5\times 10^{6}\,\mathrm{Gpc}^{-3}\,\mathrm{dex}^{-1}\left(\frac{M_{\mathrm{BH}}}{10^{7}\,\mathrm{M}_{\odot}}\right)^{\alpha}. \tag{5.9}$$

Integrating the equation over $[10^2\,\mathrm{M}_\odot,\ 10^5\,\mathrm{M}_\odot]$, we obtain $\alpha \sim -0.6$ for our WD TDE rates. It is interesting to compare the power-law index with that given by a very naive interpolation between the number density of SMBHs and that of stellar mass BHs, $\sim 2.4\times 10^5\,\mathrm{Mpc}^{-3}$ (Caputo et al., 2017). The naive interpolation gives a power-law index of $\alpha \sim -1.3$ assuming the mass range of stellar mass BHs of $[5\,\mathrm{M}_\odot,\ 100\,\mathrm{M}_\odot]$. Note that Caputo et al. (2017) estimated the number density of stellar mass BHs as 1/1000 of that of stars. There is also uncertainty in the fraction, and thus in α. Our estimate of the power-law index $\alpha \sim -0.6$ is thus middle between the naive interpolation between SMBHs and stellar mass BHs and the simple log-flat distribution ($\alpha = 0$).

Chapter 6

Conclusions

WD TDEs are exciting transients in the senses that they can be used as probes of IMBHs and can be accompanied by thermonuclear explosions of a WD. Although they are expected to be possibly detected with current and future transient surveys, there have not been any confirmed detection of WD TDEs. Further detailed modeling of observational signatures of WD TDEs is needed to search for them. In this thesis, we have first studied a variety and characteristics of the observational signatures from the thermonuclear explosions in WD TDEs, and constrained a number density of IMBHs.

We performed a suite of three different numerical simulations considering 5 parameter sets of WD TDEs where thermonuclear explosions occur. We took the WD mass as the main parameter to be varied over 0.2, 0.4, 0.6, 1.0, and 1.2 $\mathrm{M}_{\odot}$. First, we performed three-dimensional hydrodynamic simulations coupled with simplified nuclear reaction networks, and followed dynamical evolution of the tidal disruption of a WD by a BH and thermonuclear explosions in the disruption phase. Second, we performed detailed nucleosynthesis simulations in a post-process manner, and derived the synthesized nuclear compositions of the unbound ejecta. Finally, we performed radiative transfer simulations, and followed generation of photons by the radioactive decays, interactions of the photons with the unbound ejecta, and escapes of the photons from the ejecta, from which we derived the synthetic observational signatures.

As the results of the numerical simulations, we derived multi-band light curves and spectral evolutions of the 5 models as templates of the thermonuclear emission from the WD TDEs. On photometric properties, the 0.2 $\mathrm{M}_{\odot}$ model exceptionally shows relatively faint ($L_{\mathrm{peak}} \sim 10^{42}\,\mathrm{erg\,s^{-1}}$) and rapidly evolving light curves (decay timescale of $\simeq 5-10$ d), because the ejecta mass and ^{56}Ni mass are low ($0.12\,\mathrm{M}_{\odot}$ and $0,03\,\mathrm{M}_{\odot}$, respectively). The 0.4, 0.6, 1.0, and 1.2 $\mathrm{M}_{\odot}$ models are similar to some classes of thermonuclear transients, or SNe Ia, in photometric properties such as the bolometric peak luminosity, decay timescale, B-band peak magnitudes, and B-band decay timescale. However, they commonly show higher temperature than the observed thermonuclear transients around their B-band peaks. The difference can be used as a signature to distinguish the thermonuclear emission from WD TDEs from the other thermonuclear transients. All the models show a large variety in their light curves dependent on viewing angles because the ejecta is very aspherical due to the tidal disruption.

On spectroscopic properties, our WD TDE models are indeed similar to observed thermonuclear transients in some senses, such as absence of hydrogen lines and appearance of lines of iron group elements and calcium. However, there is a difference in lines of intermediate mass elements (IMEs): the observed thermonuclear transients show strong IME lines, while our models show (very) weak IME lines as a result of nucleosynthesis yielding low mass IMEs. This difference might not be conclusive because the synthesized IME masses are sensitive to numerical resolutions, and simulations with higher resolutions might result in larger IME masses and thus in stronger IME lines. Another more robust difference is Doppler shifts of spectra shown in our models. The Doppler shifts are caused by the bulk motion of the unbound ejecta escaping from the BH with velocities of $\gtrsim 10^4\,\mathrm{km\,s^{-1}}$. Although the Doppler shifts depend on viewing angles, they can be a crucial signature to distinguish WD TDEs from other transients.

We searched for observational counterparts of WD TDEs that show similar observational signatures to our models. For the 0.4, 0.6, 1.0, and 1.2 $\mathrm{M_\odot}$ models, we cannot find any good match in multi-band light curves between our models and observed transients. For the 0.2 $\mathrm{M_\odot}$ model, we found two observational candidates in relatively faint and rapid transients, which show similar multi-band light curves to the model. Because the observational data of spectra for those transients are lacking, we failed to confirm their origin as a WD TDE by comparing the spectra. However, one of the transients has a distant 10.2 kpc offset from the center of its host galaxy, which may imply that an old stellar population is the source. This may support interpreting its possible origin as a WD TDE, of which a dwarf galaxy or globular cluster containing an IMBH and WD is the plausible environment.

The photometric properties of our models cover a wide phase space. There could be a more variety of them because the intrinsic parameter sets of WD TDEs (M_WD, M_BH, β) can vary over a wider parameter space than the 5 parameter sets. We discussed the possible range of the variety of observational signatures of WD TDEs by applying the Arnett rule. First, we checked the validity of the application of the Arnett rule to WD TDEs by comparing the peak time and peak luminosity predicted by the Arnett rule and by our numerical simulations. They show reasonable matches, and thus we applied the Arnett rule to results of hydrodynamic simulations of WD TDEs considering 180 parameter sets. There could be more slowly evolving and much fainter WD TDEs with $L_\mathrm{peak} \gtrsim 10^{38}\,\mathrm{erg\,s^{-1}}$ than our 5 models with $L_\mathrm{peak} \sim 10^{42}$–$10^{43}\,\mathrm{erg\,s^{-1}}$, which arise from WD TDEs with weaker thermonuclear explosions. Such faint transients should also be searched for as WD TDEs.

Emission from WD TDEs is not only caused by thermonuclear explosions, but also by debris falling back on to the BH. If the luminosity of the fallback emission follows the mass fallback rate of the debris, the thermonuclear emission would be fainter than the fallback emission. However, it is naively expected that the fallback luminosity is limited by the Eddington luminosity unless relativistic jets are viewed on-axis. Additionally, the accretion disk formed by the fallback debris would be bright mainly in X-rays. Thus, we expect that the thermonuclear optical emission is not significantly affected by the fallback emission in most cases.

If the two observational candidates found in this thesis are really WD TDEs, they bring us insights into the event rate of WD TDEs, and thus on the number density of IMBHs. The sum of their volumetric event rates are estimated as $\simeq 600\,\mathrm{Gpc}^{-3}\,\mathrm{yr}^{-1}$. Considering a ratio of WD TDEs with thermonuclear explosions to all the WD TDEs, we obtain the total WD TDE rate as $\sim 3 \times 10^{3}\,\mathrm{Gpc}^{-3}\,\mathrm{yr}^{-1}$. Taking a WD TDE rate per an IMBH as that in centers of dwarf galaxies, $\sim 10^{-6}\,\mathrm{yr}^{-1}\,\mathrm{BH}^{-1}$, though it is still uncertain, we estimated the number density of IMBHs from the total WD TDE rate as $n_{\mathrm{IMBH}} \sim 3\,\mathrm{Mpc}^{-3}$. Although the confidence is not very high, this estimate is valuable because there has been almost no constraint on the number density of IMBHs.

The observational signatures of WD TDEs derived in this thesis are useful to search for WD TDEs with current and upcoming optical surveys. We found two observed candidates of WD TDEs in a sample of rapid transients discovered by the Dark Energy Survey. In the near future, we would be able to find more WD TDE candidates with a much larger sample of transients detected by more powerful transient surveys, such as the ZTF (Graham et al., 2019) and the LSST (LSST Science Collaboration et al., 2009; Ivezić et al., 2019). There might be transients matched with our 0.4, 0.6, 1.0, or 1.2 $\mathrm{M}_{\odot}$ model, and WD TDEs detected with high certainties showing good matches both in photometric and spectroscopic properties to our models. Although they are not the focus of this thesis, other observational signatures from WD TDEs are also worth to be studied. As we briefly mentioned in Section 4.3, the thermonuclear emission from WD TDEs may show polarization due to the aspherical shape of the unbound ejecta, and could be another distinguishable feature of WD TDEs. It is also important to model emission from fallback debris in more detail, because detection of the fallback emission by the X-ray telescope eROSITA, currently in operation, is expected (Malyali et al., 2019). Multi-messenger signals from WD TDEs, such as GWs and high energy neutrinos and cosmic rays, would independently bring us insights into dynamical parameters (the BH/WD masses and orbital parameter) and on high-energy physical processes. Finding those signatures from WD TDEs would contribute to explore origins of observed transients, to study physical processes in extreme conditions around BHs, and to reveal the unknown nature of massive BHs.

Acknowledgement

First of all, I would like to express my sincere gratitude to my supervisor Naoki Yoshida for his continuous support and advice on many aspects. He introduced the research topic and interests of academic research to me. He has not only guided me on how to conduct research but also encouraged me to proceed with my research. He also gave me many chances to have discussions and presentations in many places with his great support. The 5 years I have spent under his supervision are precious to me, and must be beneficial for the rest of my life.

I am indebted to my collaborates, Ataru Tanikawa and Keiichi Maeda. Their professional knowledge and constructive advice were essential to conduct the research. Discussions with them always gave me new insights and help to solve problems. I also thank my collaborators in the Subaru Hyper Suprime-Cam transient team, Takashi J. Moriya, Masaomi Tanaka, Nozomu Tominaga, Tomoki Morokuma, Ji-an Jiang, Naoki Yasuda, Nao Suzuki, Ichiro Takahashi, and Yusuke Tampo for their fruitful advice and discussions.

I thank Re'em Sari for his great hospitality and his advice with great insights during my visit to the Racah Institute of Physics, the Hebrew University of Jerusalem. I am also grateful to Tatsuya Matsumoto, who personally supported my stay in Jerusalem and had interesting discussions. I want to thank Shotaro Yamasaki for having interesting discussions and sharing fun times. I would like to express my appreciation to Masahiro Hoshino and Hiromoto Shibahashi for their mentorship, fruitful discussions, and insightful advice. I express my gratitude to the committee members of this dissertation, Profs. Kenta Hotokezaka, Kipp Cannon, Jun'ichi Yokoyama, Fujihiro Hamba, and Takao Nakagawa for their insightful comments and fruitful discussions.

I also thank all the members of the University of Tokyo Theoretical Astrophysical Group (UTAP) and Research Center for the Early Universe (RESCEU). I am grateful to Kazumi Kashiyama. Discussions with him motivated me to explore research fields widely and deeply. I often consulted him on many topics, including both scientific and personal ones, and he kindly listened to me and gave me fruitful advice. I also thank my colleagues, Conor Omand, Leo Tsukada, Yuta Nakagawa, Minxi He, and Akinari Hamabata for sharing precious times. My heartfelt appreciation goes to Masataka Aizawa, Taizo Okabe, Riouhei Nakatani, Ken Osato, Ryo Harada, Yuya Sakurai, and Sunmyon Chon for their advice and for sharing a nice time. I would like to thank Soichiro Hashiba, Kana Moriwaki, Yuta Tarumi, Mitani Hiroto, and Tomohisa Ueno. Discussions with them and their eager researches have motivated me to proceed with my research, and I have enjoyed sharing time with them.

Finally, I deeply thank my family and friends for their immense support and encouragement. Words are not enough to express my appreciation for them.

I am grateful to Morgan MacLeod and Miika Pursiainen for kindly sharing their data with me. I acknowledge the supports by JSPS KAKENHI Grant Number 18J20547 and by the Advanced Leading Graduate Course for Photon Science (ALPS). Numerical calculations in this work were carried out on Cray XC50/XC30 at Center for Computational Astrophysics, National Astronomical Observatory of Japan, and on Cray XC40 at the Yukawa Institute Computer Facility.

Bibliography

Abbott B. P., et al., 2017, Multi-messenger Observations of a Binary Neutron Star Merger, ApJ, 848, L12

Abbott R., et al., 2020a, GWTC-2: Compact Binary Coalescences Observed by LIGO and Virgo During the First Half of the Third Observing Run, arXiv e-prints, p. arXiv:2010.14527

Abbott R., et al., 2020b, GW190521: A Binary Black Hole Merger with a Total Mass of 150 $M_{\odot}$, Phys. Rev. Lett., 125, 101102

Abbott B. P., et al., 2020c, GW190425: Observation of a Compact Binary Coalescence with Total Mass ~ 3.4 $M_{\odot}$, ApJ, 892, L3

Alexander T., 2017, Stellar Dynamics and Stellar Phenomena Near a Massive Black Hole, ARA&A, 55, 17

Alexander K. D., Berger E., Guillochon J., Zauderer B. A., Williams P. K. G., 2016, Discovery of an Outflow from Radio Observations of the Tidal Disruption Event ASASSN-14li, ApJ, 819, L25

Alexander K. D., van Velzen S., Horesh A., Zauderer B. A., 2020, Radio Properties of Tidal Disruption Events, Space Sci. Rev., 216, 81

Alves Batista R., Silk J., 2017, Ultrahigh-energy cosmic rays from tidally-ignited white dwarfs, Phys. Rev. D, 96, 103003

Amaro-Seoane P., et al., 2017, Laser Interferometer Space Antenna, arXiv e-prints, p. arXiv:1702.00786

Ambwani K., Sutherland P., 1988, Gamma-Ray Spectra and Energy Deposition for Type IA Supernovae, ApJ, 325, 820

Anninos P., Fragile P. C., Olivier S. S., Hoffman R., Mishra B., Camarda K., 2018, Relativistic Tidal Disruption and Nuclear Ignition of White Dwarf Stars by Intermediate-mass Black Holes, ApJ, 865, 3

Anninos P., Hoffman R. D., Grewal M., Lavell M. J., Fragile P. C., 2019, Nuclear Ignition of White Dwarf Stars by Relativistic Encounters with Rotating Intermediate Mass Black Holes, ApJ, 885, 136

Arnett W. D., 1982, Type I supernovae. I - Analytic solutions for the early part of the light curve, ApJ, 253, 785

Auchettl K., Guillochon J., Ramirez-Ruiz E., 2017, New Physical Insights about Tidal Disruption Events from a Comprehensive Observational Inventory at X-Ray Wavelengths, ApJ, 838, 149

Baade W., Zwicky F., 1934, On Super-novae, Proceedings of the National Academy of Science, 20, 254

Bade N., Komossa S., Dahlem M., 1996, Detection of an extremely soft X-ray outburst in the HII-like nucleus of NGC 5905., A&A, 309, L35

Bader G., Deuflhard P., 1983, A semi-implicit mid-point rule for stiff systems of ordinary differential equations, Numerische Mathematik, 41, 373

Bahcall J. N., Ostriker J. P., 1975, Massive black holes in globular clusters., Nature, 256, 23

Balsara D. S., 1995, von Neumann stability analysis of smooth particle hydrodynamics–suggestions for optimal algorithms, Journal of Computational Physics, 121, 357

Bauer F. E., et al., 2017, A new, faint population of X-ray transients, MNRAS, 467, 4841

Baumgardt H., Makino J., Ebisuzaki T., 2004a, Massive Black Holes in Star Clusters. I. Equal-Mass Clusters, ApJ, 613, 1133

Baumgardt H., Makino J., Ebisuzaki T., 2004b, Massive Black Holes in Star Clusters. II. Realistic Cluster Models, ApJ, 613, 1143

Begelman M. C., Rees M. J., 1978, The fate of dense stellar systems, MNRAS, 185, 847

Bersten M. C., Benvenuto O. G., Orellana M., Nomoto K., 2016, The Unusual Super-luminous Supernovae SN 2011kl and ASASSN-15lh, ApJ, 817, L8

Bicknell G. V., Gingold R. A., 1983, On tidal detonation of stars by massive black holes, ApJ, 273, 749

Bildsten L., Shen K. J., Weinberg N. N., Nelemans G., 2007, Faint Thermonuclear Supernovae from AM Canum Venaticorum Binaries, ApJ, 662, L95

Blanchard P. K., et al., 2017, PS16dtm: A Tidal Disruption Event in a Narrow-line Seyfert 1 Galaxy, ApJ, 843, 106

Bloom J. S., et al., 2011, A Possible Relativistic Jetted Outburst from a Massive Black Hole Fed by a Tidally Disrupted Star, Science, 333, 203

Bond J. R., Arnett W. D., Carr B. J., 1984, The evolution and fate of Very Massive Objects, ApJ, 280, 825

Bonnerot C., Stone N., 2020, Formation of an Accretion Flow, arXiv e-prints, p. arXiv:2008.11731

Branch D., Baron E., Thomas R. C., Kasen D., Li W., Filippenko A. V., 2004, Reading the Spectra of the Most Peculiar Type Ia Supernova 2002cx, PASP, 116, 903

Brassart M., Luminet J. P., 2008, Shock waves in tidally compressed stars by massive black holes, A&A, 481, 259

Brassart M., Luminet J. P., 2010, Relativistic tidal compressions of a star by a massive black hole, A&A, 511, A80

Bricman K., Gomboc A., 2020, The Prospects of Observing Tidal Disruption Events with the Large Synoptic Survey Telescope, ApJ, 890, 73

Brodie J. P., Strader J., 2006, Extragalactic Globular Clusters and Galaxy Formation, ARA&A, 44, 193

Brown G. C., Levan A. J., Stanway E. R., Tanvir N. R., Cenko S. B., Berger E., Chornock R., Cucchiaria A., 2015, Swift J1112.2-8238: a candidate relativistic tidal disruption flare, MNRAS, 452, 4297

Bullock J. S., Boylan-Kolchin M., 2017, Small-Scale Challenges to the ΛCDM Paradigm, ARA&A, 55, 343

Burrows A., Vartanyan D., 2020, Core-Collapse Supernova Explosion Theory, arXiv e-prints, p. arXiv:2009.14157

Burrows D. N., et al., 2011, Relativistic jet activity from the tidal disruption of a star by a massive black hole, Nature, 476, 421

Cannizzo J. K., Lee H. M., Goodman J., 1990, The Disk Accretion of a Tidally Disrupted Star onto a Massive Black Hole, ApJ, 351, 38

Caputo D. P., de Vries N., Patruno A., Portegies Zwart S., 2017, On Estimating the Total Number of Intermediate Mass Black Holes, MNRAS, 468, 4000

Carter B., Luminet J. P., 1982, Pancake detonation of stars by black holes in galactic nuclei, Nature, 296, 211

Carter B., Luminet J.-P., 1983, Tidal compression of a star by a large black hole. I Mechanical evolution and nuclear energy release by proton capture, A&A, 121, 97

Caughlan G. R., Fowler W. A., 1988, Thermonuclear Reaction Rates V, Atomic Data and Nuclear Data Tables, 40, 283

Cenko S. B., 2017, Astrophysics: The true nature of transients, Nature Astronomy, 1, 0008

Cenko S. B., et al., 2012, Swift J2058.4+0516: Discovery of a Possible Second Relativistic Tidal Disruption Flare?, ApJ, 753, 77

Chen P., et al., 2020, The Most Rapidly Declining Type I Supernova 2019bkc/ATLAS19dqr, ApJ, 889, L6

Chomiuk L., Metzger B. D., Shen K. J., 2020, New Insights into Classical Novae, arXiv e-prints, p. arXiv:2011.08751

Curd B., Narayan R., 2019, GRRMHD simulations of tidal disruption event accretion discs around supermassive black holes: jet formation, spectra, and detectability, MNRAS, 483, 565

Dai L., Fang K., 2017, Can tidal disruption events produce the IceCube neutrinos?, MNRAS, 469, 1354

Dai L., McKinney J. C., Roth N., Ramirez-Ruiz E., Miller M. C., 2018, A Unified Model for Tidal Disruption Events, ApJ, 859, L20

Dainotti M. G., Bernardini M. G., Bianco C. L., Caito L., Guida R., Ruffini R., 2007, GRB 060218 and GRBs associated with supernovae Ib/c, A&A, 471, L29

De Colle F., Lu W., 2020, Jets from Tidal Disruption Events, New Astron. Rev., 89, 101538

De Colle F., Guillochon J., Naiman J., Ramirez-Ruiz E., 2012, The Dynamics, Appearance, and Demographics of Relativistic Jets Triggered by Tidal Disruption of Stars in Quiescent Supermassive Black Holes, ApJ, 760, 103

De K., et al., 2018a, A hot and fast ultra-stripped supernova that likely formed a compact neutron star binary, Science, 362, 201

De K., et al., 2018b, iPTF 16hgs: A Double-peaked Ca-rich Gap Transient in a Metal-poor, Star-forming Dwarf Galaxy, ApJ, 866, 72

Dehnen W., Aly H., 2012, Improving convergence in smoothed particle hydrodynamics simulations without pairing instability, MNRAS, 425, 1068

Dong S., et al., 2016, ASASSN-15lh: A highly super-luminous supernova, Science, 351, 257

Dou L., Wang T.-g., Jiang N., Yang C., Lyu J., Zhou H., 2016, Long Fading Mid-infrared Emission in Transient Coronal Line Emitters: Dust Echo of a Tidal Disruption Flare, ApJ, 832, 188

Dou L., Wang T., Yan L., Jiang N., Yang C., Cutri R. M., Mainzer A., Peng B., 2017, Discovery of a Mid-infrared Echo from the TDE Candidate in the Nucleus of ULIRG F01004-2237, ApJ, 841, L8

Drout M. R., et al., 2013, The Fast and Furious Decay of the Peculiar Type Ic Supernova 2005ek, ApJ, 774, 58

Drout M. R., et al., 2014, Rapidly Evolving and Luminous Transients from Pan-STARRS1, ApJ, 794, 23

Duff I., Erisman A., Reid J., 1986, Direct methods for sparse matrices. Clarendon

East W. E., 2014, Gravitational Waves from the Collision of Tidally Disrupted Stars with Massive Black Holes, ApJ, 795, 135

Eastman R. G., Pinto P. A., 1993, Spectrum Formation in Supernovae: Numerical Techniques, ApJ, 412, 731

Esquej P., Saxton R. D., Freyberg M. J., Read A. M., Altieri B., Sanchez-Portal M., Hasinger G., 2007, Candidate tidal disruption events from the XMM-Newton slew survey, A&A, 462, L49

Esquej P., et al., 2008, Evolution of tidal disruption candidates discovered by XMM-Newton, A&A, 489, 543

Evans C. R., Kochanek C. S., 1989, The Tidal Disruption of a Star by a Massive Black Hole, ApJ, 346, L13

Farr W. M., Sravan N., Cantrell A., Kreidberg L., Bailyn C. D., Mandel I., Kalogera V., 2011, The Mass Distribution of Stellar-mass Black Holes, ApJ, 741, 103

Ferrarese L., Merritt D., 2000, A Fundamental Relation between Supermassive Black Holes and Their Host Galaxies, ApJ, 539, L9

Foley R. J., et al., 2013, Type Iax Supernovae: A New Class of Stellar Explosion, ApJ, 767, 57

Fragione G., Leigh N. W. C., Ginsburg I., Kocsis B., 2018, Tidal Disruption Events and Gravitational Waves from Intermediate-mass Black Holes in Evolving Globular Clusters across Space and Time, ApJ, 867, 119

Fragione G., Metzger B. D., Perna R., Leigh N. W. C., Kocsis B., 2020, Electromagnetic transients and gravitational waves from white dwarf disruptions by stellar black holes in triple systems, MNRAS, 495, 1061

Frank J., 1978, Tidal disruption by a massive black hole and collisions in galactic nuclei, MNRAS, 184, 87

Frank J., Rees M. J., 1976, Effects of massive central black holes on dense stellar systems, MNRAS, 176, 633

Fraser M., 2020, Supernovae and transients with circumstellar interaction, Royal Society Open Science, 7, 200467

Fryxell B., et al., 2000, FLASH: An Adaptive Mesh Hydrodynamics Code for Modeling Astrophysical Thermonuclear Flashes, ApJS, 131, 273

Gafton E., Rosswog S., 2019, Tidal disruptions by rotating black holes: effects of spin and impact parameter, MNRAS, 487, 4790

Gao H., Lei W.-H., You Z.-Q., Xie W., 2016, The Black Hole Central Engine for Ultra-long Gamma-Ray Burst 111209A and Its Associated Supernova 2011kl, ApJ, 826, 141

García-Berro E., Badenes C., Aznar-Siguán G., Lorén-Aguilar P., 2017, White dwarf dynamical interactions and fast optical transients, MNRAS, 468, 4815

Generozov A., Mimica P., Metzger B. D., Stone N. C., Giannios D., Aloy M. A., 2017, The influence of circumnuclear environment on the radio emission from TDE jets, MNRAS, 464, 2481

Gezari S., et al., 2012, An ultraviolet-optical flare from the tidal disruption of a helium-rich stellar core, Nature, 485, 217

Giannios D., Metzger B. D., 2011, Radio transients from stellar tidal disruption by massive black holes, MNRAS, 416, 2102

Graham M. J., et al., 2019, The Zwicky Transient Facility: Science Objectives, PASP, 131, 078001

Greene J. E., Strader J., Ho L. C., 2020, Intermediate-Mass Black Holes, ARA&A, 58, 257

Grupe D., Thomas H. C., Leighly K. M., 1999, RX J1624.9+7554: a new X-ray transient AGN, A&A, 350, L31

Guillochon J., Ramirez-Ruiz E., 2013, Hydrodynamical Simulations to Determine the Feeding Rate of Black Holes by the Tidal Disruption of Stars: The Importance of the Impact Parameter and Stellar Structure, ApJ, 767, 25

Guillochon J., Ramirez-Ruiz E., Rosswog S., Kasen D., 2009, Three-dimensional Simulations of Tidally Disrupted Solar-type Stars and the Observational Signatures of Shock Breakout, ApJ, 705, 844

Guillochon J., Manukian H., Ramirez-Ruiz E., 2014, PS1-10jh: The Disruption of a Main-sequence Star of Near-solar Composition, ApJ, 783, 23

Guillochon J., McCourt M., Chen X., Johnson M. D., Berger E., 2016, Unbound Debris Streams and Remnants Resulting from the Tidal Disruptions of Stars by Supermassive Black Holes, ApJ, 822, 48

Guillochon J., Parrent J., Kelley L. Z., Margutti R., 2017, An Open Catalog for Supernova Data, ApJ, 835, 64

Haas R., Shcherbakov R. V., Bode T., Laguna P., 2012, Tidal Disruptions of White Dwarfs from Ultra-close Encounters with Intermediate-mass Spinning Black Holes, ApJ, 749, 117

Hachinger S., Mazzali P. A., Taubenberger S., Hillebrand t W., Nomoto K., Sauer D. N., 2012, How much H and He is 'hidden' in SNe Ib/c? - I. Low-mass objects, MNRAS, 422, 70

Haehnelt M. G., Rees M. J., 1993, The formation of nuclei in newly formed galaxies and the evolution of the quasar population, MNRAS, 263, 168

Harkness R. P., et al., 1987, The Early Spectral Phase of Type Ib Supernovae: Evidence for Helium, ApJ, 317, 355

Hayasaki K., Yamazaki R., 2019, Neutrino Emissions from Tidal Disruption Remnants, ApJ, 886, 114

Hayasaki K., Stone N., Loeb A., 2016, Circularization of tidally disrupted stars around spinning supermassive black holes, MNRAS, 461, 3760

Hills J. G., 1975, Possible power source of Seyfert galaxies and QSOs, Nature, 254, 295

Hoeflich P., Khokhlov A., Mueller E., 1992, Gamma-ray light curves and spectra for Type IA supernovae, A&A, 259, 549

Hoflich P., 1991, Asphericity effects in scatterring dominated photospheres., A&A, 246, 481

Holcomb C., Guillochon J., De Colle F., Ramirez-Ruiz E., 2013, Conditions for Successful Helium Detonations in Astrophysical Environments, ApJ, 771, 14

Holoien T. W. S., et al., 2016, Six months of multiwavelength follow-up of the tidal disruption candidate ASASSN-14li and implied TDE rates from ASAS-SN, MNRAS, 455, 2918

Hubbell J. H., 1969, Photon cross sections, attenuation coefficients, and energy absorption coefficients from 10 keV to 100 GeV. NSRDS, `https://cds.cern.ch/record/104383`

Ioka K., Hotokezaka K., Piran T., 2016, Are Ultra-long Gamma-Ray Bursts Caused by Blue Supergiant Collapsars, Newborn Magnetars, or White Dwarf Tidal Disruption Events?, ApJ, 833, 110

Irwin J. A., et al., 2016, Ultraluminous X-ray bursts in two ultracompact companions to nearby elliptical galaxies, Nature, 538, 356

Itoh N., Hayashi H., Nishikawa A., Kohyama Y., 1996, Neutrino Energy Loss in Stellar Interiors. VII. Pair, Photo-, Plasma, Bremsstrahlung, and Recombination Neutrino Processes, ApJS, 102, 411

Ivezić Ž., et al., 2019, LSST: From Science Drivers to Reference Design and Anticipated Data Products, ApJ, 873, 111

Iwasawa M., Tanikawa A., Hosono N., Nitadori K., Muranushi T., Makino J., 2016a, FDPS: Framework for Developing Particle Simulators (ascl:1604.011)

Iwasawa M., Tanikawa A., Hosono N., Nitadori K., Muranushi T., Makino J., 2016b, Implementation and performance of FDPS: a framework for developing parallel particle simulation codes, PASJ, 68, 54

Jha S. W., 2017, Type Iax Supernovae. p. 375, doi:10.1007/978-3-319-21846-5_42

Jiang N., Dou L., Wang T., Yang C., Lyu J., Zhou H., 2016a, The WISE Detection of an Infrared Echo in Tidal Disruption Event ASASSN-14li, ApJ, 828, L14

Jiang Y.-F., Guillochon J., Loeb A., 2016b, Prompt Radiation and Mass Outflows from the Stream-Stream Collisions of Tidal Disruption Events, ApJ, 830, 125

Jiang N., et al., 2017, Mid-infrared Flare of TDE Candidate PS16dtm: Dust Echo and Implications for the Spectral Evolution, ApJ, 850, 63

Jiang N., Wang T., Mou G., Liu H., Dou L., Sheng Z., Wang Y., 2019, Infrared Echo and Late-stage Rebrightening of Nuclear Transient Ps1-10adi: Exploring the Torus with Tidal Disruption Events in Active Galactic Nuclei, ApJ, 871, 15

Jonker P. G., et al., 2013, Discovery of a New Kind of Explosive X-Ray Transient near M86, ApJ, 779, 14

Kara E., Miller J. M., Reynolds C., Dai L., 2016, Relativistic reverberation in the accretion flow of a tidal disruption event, Nature, 535, 388

Karp A. H., Lasher G., Chan K. L., Salpeter E. E., 1977, The opacity of expanding media: the effect of spectral lines., ApJ, 214, 161

Kasen D., 2006, Secondary Maximum in the Near-Infrared Light Curves of Type Ia Supernovae, ApJ, 649, 939

Kasen D., Thomas R. C., Nugent P., 2006, Time-dependent Monte Carlo Radiative Transfer Calculations for Three-dimensional Supernova Spectra, Light Curves, and Polarization, ApJ, 651, 366

Kasliwal M. M., 2012, Systematically Bridging the Gap Between Novae and Supernovae, Publ. Astron. Soc. Australia, 29, 482

Kasliwal M. M., et al., 2010, Rapidly Decaying Supernova 2010X: A Candidate ".Ia" Explosion, ApJ, 723, L98

Kasliwal M. M., et al., 2012, Calcium-rich Gap Transients in the Remote Outskirts of Galaxies, ApJ, 755, 161

Kawana K., Tanikawa A., Yoshida N., 2018, Tidal disruption of a white dwarf by a black hole: the diversity of nucleosynthesis, explosion energy, and the fate of debris streams, MNRAS, 477, 3449

Kelley L. Z., Tchekhovskoy A., Narayan R., 2014, Tidal disruption and magnetic flux capture: powering a jet from a quiescent black hole, MNRAS, 445, 3919

Khabibullin I., Sazonov S., Sunyaev R., 2014, SRG/eROSITA prospects for the detection of stellar tidal disruption flares, MNRAS, 437, 327

Kobayashi S., Laguna P., Phinney E. S., Mészáros P., 2004, Gravitational Waves and X-Ray Signals from Stellar Disruption by a Massive Black Hole, ApJ, 615, 855

Kochanek C. S., 2016, Tidal disruption event demographics, MNRAS, 461, 371

Komossa S., 2015, Tidal disruption of stars by supermassive black holes: Status of observations, Journal of High Energy Astrophysics, 7, 148

Komossa S., Bade N., 1999, The giant X-ray outbursts in NGC 5905 and IC 3599:() hfill Follow-up observations and outburst scenarios, A&A, 343, 775

Kool E. C., et al., 2020, AT 2017gbl: a dust obscured TDE candidate in a luminous infrared galaxy, MNRAS, 498, 2167

Kormendy J., Ho L. C., 2013, Coevolution (Or Not) of Supermassive Black Holes and Host Galaxies, ARA&A, 51, 511

Kormendy J., Richstone D., 1995, Inward Bound—The Search For Supermassive Black Holes In Galactic Nuclei, ARA&A, 33, 581

Koushiappas S. M., Bullock J. S., Dekel A., 2004, Massive black hole seeds from low angular momentum material, MNRAS, 354, 292

Krolik J. H., Piran T., 2011, Swift J1644+57: A White Dwarf Tidally Disrupted by a 10^4 $M_\odot$ Black Hole?, ApJ, 743, 134

Kromer M., Sim S. A., 2009, Time-dependent three-dimensional spectrum synthesis for Type Ia supernovae, MNRAS, 398, 1809

Kromer M., et al., 2013, 3D deflagration simulations leaving bound remnants: a model for 2002cx-like Type Ia supernovae, MNRAS, 429, 2287

Kuin N. P. M., et al., 2019, Swift spectra of AT2018cow: a white dwarf tidal disruption event?, MNRAS, 487, 2505

Kurucz R. L., Bell B., 1995, Atomic line list

LSST Science Collaboration et al., 2009, LSST Science Book, Version 2.0, preprint, (`arXiv:0912.0201`)

Law-Smith J., MacLeod M., Guillochon J., Macias P., Ramirez-Ruiz E., 2017, Low-mass White Dwarfs with Hydrogen Envelopes as a Missing Link in the Tidal Disruption Menu, ApJ, 841, 132

Lee M. H., 1993, N-Body Evolution of Dense Clusters of Compact Stars, ApJ, 418, 147

Leloudas G., et al., 2016, The superluminous transient ASASSN-15lh as a tidal disruption event from a Kerr black hole, Nature Astronomy, 1, 0002

Levan A. J., et al., 2011, An Extremely Luminous Panchromatic Outburst from the Nucleus of a Distant Galaxy, Science, 333, 199

Levan A. J., et al., 2014, A New Population of Ultra-long Duration Gamma-Ray Bursts, ApJ, 781, 13

Lightman A. P., Shapiro S. L., 1977, The distribution and consumption rate of stars around a massive, collapsed object, ApJ, 211, 244

Lin D., Carrasco E. R., Grupe D., Webb N. A., Barret D., Farrell S. A., 2011, Discovery of an Ultrasoft X-Ray Transient Source in the 2XMM Catalog: A Tidal Disruption Event Candidate, ApJ, 738, 52

Lin D., et al., 2018, A luminous X-ray outburst from an intermediate-mass black hole in an off-centre star cluster, Nature Astronomy, 2, 656

Lin D., et al., 2020, Multiwavelength Follow-up of the Hyperluminous Intermediate-mass Black Hole Candidate 3XMM J215022.4-055108, ApJ, 892, L25

Liu R.-Y., Xi S.-Q., Wang X.-Y., 2020a, Neutrino emission from an off-axis jet driven by the tidal disruption event AT2019dsg, Phys. Rev. D, 102, 083028

Liu Z., Li D., Liu H.-Y., Lu Y., Yuan W., Dou L., Shen R.-F., 2020b, A Tidal Disruption Event Candidate Discovered in the Active Galactic Nucleus SDSS J022700.77-042020.6, ApJ, 894, 93

Lodato G., Rossi E. M., 2011, Multiband light curves of tidal disruption events, MNRAS, 410, 359

Loeb A., Rasio F. A., 1994, Collapse of Primordial Gas Clouds and the Formation of Quasar Black Holes, ApJ, 432, 52

Loeb A., Ulmer A., 1997, Optical Appearance of the Debris of a Star Disrupted by a Massive Black Hole, ApJ, 489, 573

Lu W., Bonnerot C., 2020, Self-intersection of the fallback stream in tidal disruption events, MNRAS, 492, 686

Lu W., Kumar P., Evans N. J., 2016, Infrared emission from tidal disruption events - probing the pc-scale dust content around galactic nuclei, MNRAS, 458, 575

Lucy L. B., 1977, A numerical approach to the testing of the fission hypothesis., AJ, 82, 1013

Lucy L. B., 1991, Nonthermal Excitation of Helium in Type Ib Supernovae, ApJ, 383, 308

Lucy L. B., 2005, Monte Carlo techniques for time-dependent radiative transfer in 3-D supernovae, A&A, 429, 19

Luminet J.-P., Pichon B., 1989a, Tidally-detonated nuclear reactions in main sequence stars passing near a large black hole, A&A, 209, 85

Luminet J.-P., Pichon B., 1989b, Tidal pinching of white dwarfs, A&A, 209, 103

Lunnan R., et al., 2017, Two New Calcium-rich Gap Transients in Group and Cluster Environments, ApJ, 836, 60

MacLeod M., Goldstein J., Ramirez-Ruiz E., Guillochon J., Samsing J., 2014, Illuminating Massive Black Holes with White Dwarfs: Orbital Dynamics and High-energy Transients from Tidal Interactions, ApJ, 794, 9

MacLeod M., Guillochon J., Ramirez-Ruiz E., Kasen D., Rosswog S., 2016, Optical Thermonuclear Transients from Tidal Compression of White Dwarfs as Tracers of the Low End of the Massive Black Hole Mass Function, ApJ, 819, 3

Madau P., Rees M. J., 2001, Massive Black Holes as Population III Remnants, ApJ, 551, L27

Maeda K., 2006, Three-dimensional Simulation of Gamma-Ray Emission from Asymmetric Supernovae and Hypernovae, ApJ, 644, 385

Maeda K., Kutsuna M., Shigeyama T., 2014, Signatures of a Companion Star in Type Ia Supernovae, ApJ, 794, 37

Magorrian J., Tremaine S., 1999, Rates of tidal disruption of stars by massive central black holes, MNRAS, 309, 447

Maguire K., Eracleous M., Jonker P. G., MacLeod M., Rosswog S., 2020, Tidal Disruptions of White Dwarfs: Theoretical Models and Observational Prospects, Space Sci. Rev., 216, 39

Mainetti D., Lupi A., Campana S., Colpi M., Coughlin E. R., Guillochon J., Ramirez-Ruiz E., 2017, The fine line between total and partial tidal disruption events, A&A, 600, A124

Malyali A., Rau A., Nandra K., 2019, eROSITA detection rates for tidal disruptions of white dwarfs by intermediate mass black holes, MNRAS, 489, 5413

Maoz D., Mannucci F., Nelemans G., 2014, Observational Clues to the Progenitors of Type Ia Supernovae, ARA&A, 52, 107

Margutti R., et al., 2019, An Embedded X-Ray Source Shines through the Aspherical AT 2018cow: Revealing the Inner Workings of the Most Luminous Fast-evolving Optical Transients, ApJ, 872, 18

Mattila S., et al., 2018, A dust-enshrouded tidal disruption event with a resolved radio jet in a galaxy merger, Science, 361, 482

McLaughlin D. E., 1999, The Efficiency of Globular Cluster Formation, AJ, 117, 2398

Merritt D., 2013, Loss-cone dynamics, Classical and Quantum Gravity, 30, 244005

Metzger B. D., Stone N. C., 2016, A bright year for tidal disruptions, MNRAS, 461, 948

Metzger B. D., Giannios D., Mimica P., 2012, Afterglow model for the radio emission from the jetted tidal disruption candidate Swift J1644+57, MNRAS, 420, 3528

Mezcua M., 2017, Observational evidence for intermediate-mass black holes, International Journal of Modern Physics D, 26, 1730021

Milisavljevic D., et al., 2017, iPTF15eqv: Multiwavelength Exposé of a Peculiar Calcium-rich Transient, ApJ, 846, 50

Miller M. C., 2015, Disk Winds as an Explanation for Slowly Evolving Temperatures in Tidal Disruption Events, ApJ, 805, 83

Miller J. M., et al., 2015, Flows of X-ray gas reveal the disruption of a star by a massive black hole, Nature, 526, 542

Mimica P., Giannios D., Metzger B. D., Aloy M. A., 2015, The radio afterglow of Swift J1644+57 reveals a powerful jet with fast core and slow sheath, MNRAS, 450, 2824

Monaghan J. J., 1997, SPH and Riemann Solvers, Journal of Computational Physics, 136, 298

Moriya T. J., Sorokina E. I., Chevalier R. A., 2018, Superluminous Supernovae, Space Sci. Rev., 214, 59

Morris J. P., Monaghan J. J., 1997, A Switch to Reduce SPH Viscosity, Journal of Computational Physics, 136, 41

Murase K., Kimura S. S., Zhang B. T., Oikonomou F., Petropoulou M., 2020, High-energy Neutrino and Gamma-Ray Emission from Tidal Disruption Events, ApJ, 902, 108

Nakar E., 2015, A Unified Picture for Low-luminosity and Long Gamma-Ray Bursts Based on the Extended Progenitor of llGRB 060218/SN 2006aj, ApJ, 807, 172

Özel F., Psaltis D., Narayan R., McClintock J. E., 2010, The Black Hole Mass Distribution in the Galaxy, ApJ, 725, 1918

Pasham D. R., et al., 2019, A loud quasi-periodic oscillation after a star is disrupted by a massive black hole, Science, 363, 531

Peng Z.-K., Yang Y.-S., Shen R.-F., Wang L.-J., Zou J.-H., Zhang B.-B., 2019, CDF-S XT1 and XT2: White Dwarf Tidal Disruption Events by Intermediate-mass Black Holes?, ApJ, 884, L34

Perets H. B., et al., 2010, A faint type of supernova from a white dwarf with a helium-rich companion, Nature, 465, 322

Phillips M. M., 1993, The Absolute Magnitudes of Type IA Supernovae, ApJ, 413, L105

Phillips M. M., Lira P., Suntzeff N. B., Schommer R. A., Hamuy M., Maza J., 1999, The Reddening-Free Decline Rate Versus Luminosity Relationship for Type IA Supernovae, AJ, 118, 1766

Piran T., Svirski G., Krolik J., Cheng R. M., Shiokawa H., 2015, 'Disk Formation Versus Disk Accretion—What Powers Tidal Disruption Events?, ApJ, 806, 164

Poznanski D., et al., 2010, An Unusually Fast-Evolving Supernova, Science, 327, 58

Prentice S. J., et al., 2020, The rise and fall of an extraordinary Ca-rich transient. The discovery of ATLAS19dqr/SN 2019bkc, A&A, 635, A186

Press W., Teukolsky S., Vetterling W., Flannery B., Metcalf M., 1996, Numerical Recipes in Fortran 90, Volume 2

Pursiainen M., 2020, private communication

Pursiainen M., et al., 2018, Rapidly evolving transients in the Dark Energy Survey, MNRAS, 481, 894

Quinlan G. D., Shapiro S. L., 1990, The Dynamical Evolution of Dense Star Clusters in Galactic Nuclei, ApJ, 356, 483

Ramirez-Ruiz E., Rosswog S., 2009, The Star Ingesting Luminosity of Intermediate-Mass Black Holes in Globular Clusters, ApJ, 697, L77

Raskin C., Scannapieco E., Rockefeller G., Fryer C., Diehl S., Timmes F. X., 2010, ^{56}Ni Production in Double-degenerate White Dwarf Collisions, ApJ, 724, 111

Rauch K. P., Tremaine S., 1996, Resonant relaxation in stellar systems, New Astron., 1, 149

Rees M. J., 1978, Quasars, The Observatory, 98, 210

Rees M. J., 1984, Black Hole Models for Active Galactic Nuclei, ARA&A, 22, 471

Rees M. J., 1988, Tidal disruption of stars by black holes of 10^6-10^8 solar masses in nearby galaxies, Nature, 333, 523

Rees M. J., 1990, “Dead Quasars” in Nearby Galaxies?, Science, 247, 817

Rossi E. M., Stone N. C., Law-Smith J. A. P., MacLeod M., Lodato G., Dai J. L., Mand el I., 2020, The Process of Stellar Tidal Disruption by Supermassive Black Holes. The first pericenter passage, arXiv e-prints, p. arXiv:2005.12528

Rosswog S., 2015, SPH Methods in the Modelling of Compact Objects, Living Reviews in Computational Astrophysics, 1, 1

Rosswog S., Ramirez-Ruiz E., Hix W. R., 2008, Atypical Thermonuclear Supernovae from Tidally Crushed White Dwarfs, ApJ, 679, 1385

Rosswog S., Ramirez-Ruiz E., Hix W. R., 2009, Tidal Disruption and Ignition of White Dwarfs by Moderately Massive Black Holes, ApJ, 695, 404

Roth N., Kasen D., 2018, What Sets the Line Profiles in Tidal Disruption Events?, ApJ, 855, 54

Roth N., Kasen D., Guillochon J., Ramirez-Ruiz E., 2016, The X-Ray through Optical Fluxes and Line Strengths of Tidal Disruption Events, ApJ, 827, 3

Roth N., Rossi E. M., Krolik J., Piran T., Mockler B., Kasen D., 2020, Radiative Emission Mechanisms, Space Sci. Rev., 216, 114

Röttgers B., Arth A., 2018, SPH to Grid: a new integral conserving method, arXiv e-prints, p. arXiv:1803.03652

Sari R., Piran T., Narayan R., 1998, Spectra and Light Curves of Gamma-Ray Burst Afterglows, ApJ, 497, L17

Sari R., Kobayashi S., Rossi E. M., 2010, Hypervelocity Stars and the Restricted Parabolic Three-Body Problem, ApJ, 708, 605

Sato Y., Nakasato N., Tanikawa A., Nomoto K., Maeda K., Hachisu I., 2015, A Systematic Study of Carbon-Oxygen White Dwarf Mergers: Mass Combinations for Type Ia Supernovae, ApJ, 807, 105

Sato Y., Nakasato N., Tanikawa A., Nomoto K., Maeda K., Hachisu I., 2016, The Critical Mass Ratio of Double White Dwarf Binaries for Violent Merger-induced Type Ia Supernova Explosions, ApJ, 821, 67

Saxton R. D., Read A. M., Esquej P., Komossa S., Dougherty S., Rodriguez-Pascual P., Barrado D., 2012, A tidal disruption-like X-ray flare from the quiescent galaxy SDSS J120136.02+300305.5, A&A, 541, A106

Saxton R., Komossa S., Auchettl K., Jonker P. G., 2020, X-Ray Properties of TDEs, Space Sci. Rev., 216, 85

Schlafly E. F., Finkbeiner D. P., 2011, Measuring Reddening with Sloan Digital Sky Survey Stellar Spectra and Recalibrating SFD, ApJ, 737, 103

Sell P. H., Maccarone T. J., Kotak R., Knigge C., Sand D. J., 2015, Calcium-rich gap transients: tidal detonations of white dwarfs?, MNRAS, 450, 4198

Sell P. H., Arur K., Maccarone T. J., Kotak R., Knigge C., Sand D. J., Valenti S., 2018, Chandra X-ray constraints on the candidate Ca-rich gap transient SN 2016hnk, MNRAS, 475, L111

Shakura N. I., Sunyaev R. A., 1973, Reprint of 1973A&A....24..337S. Black holes in binary systems. Observational appearance., A&A, 500, 33

Shapiro P. R., Sutherland P. G., 1982, The polarization of supernova light - A measure of deviation from spherical symmetry, ApJ, 263, 902

Shapiro S. L., Teukolsky S. A., 1983, Black holes, white dwarfs, and neutron stars : the physics of compact objects

Shcherbakov R. V., Pe'er A., Reynolds C. S., Haas R., Bode T., Laguna P., 2013, GRB060218 as a Tidal Disruption of a White Dwarf by an Intermediate-mass Black Hole, ApJ, 769, 85

Shen R.-F., 2019, Fast, Ultraluminous X-Ray Bursts from Tidal Stripping of White Dwarfs by Intermediate-mass Black Holes, ApJ, 871, L17

Shen K. J., Kasen D., Weinberg N. N., Bildsten L., Scannapieco E., 2010, Thermonuclear .Ia Supernovae from Helium Shell Detonations: Explosion Models and Observables, ApJ, 715, 767

Shiokawa H., Krolik J. H., Cheng R. M., Piran T., Noble S. C., 2015, General Relativistic Hydrodynamic Simulation of Accretion Flow from a Stellar Tidal Disruption, ApJ, 804, 85

Stein R., et al., 2020, A high-energy neutrino coincident with a tidal disruption event, arXiv e-prints, p. arXiv:2005.05340

Steinberg E., Coughlin E. R., Stone N. C., Metzger B. D., 2019, Thawing the frozen-in approximation: implications for self-gravity in deeply plunging tidal disruption events, MNRAS, 485, L146

Stone N. C., Metzger B. D., 2016, Rates of stellar tidal disruption as probes of the supermassive black hole mass function, MNRAS, 455, 859

Stone N., Sari R., Loeb A., 2013, Consequences of strong compression in tidal disruption events, MNRAS, 435, 1809

Stone N. C., Kesden M., Cheng R. M., van Velzen S., 2019, Stellar tidal disruption events in general relativity, General Relativity and Gravitation, 51, 30

Stone N. C., Vasiliev E., Kesden M., Rossi E. M., Perets H. B., Amaro-Seoane P., 2020, Rates of Stellar Tidal Disruption, Space Sci. Rev., 216, 35

Stritzinger M. D., et al., 2014, Optical and near-IR observations of the faint and fast 2008ha-like supernova 2010ae, A&A, 561, A146

Stritzinger M. D., et al., 2015, Comprehensive observations of the bright and energetic Type Iax SN 2012Z: Interpretation as a Chandrasekhar mass white dwarf explosion, A&A, 573, A2

Strubbe L. E., Quataert E., 2009, Optical flares from the tidal disruption of stars by massive black holes, MNRAS, 400, 2070

Swartz D. A., 1991, Ionization by High-Energy Particles and the Electron Scattering Opacity in Supernovae, ApJ, 373, 604

Syer D., Ulmer A., 1999, Tidal disruption rates of stars in observed galaxies, MNRAS, 306, 35

Tadhunter C., Spence R., Rose M., Mullaney J., Crowther P., 2017, A tidal disruption event in the nearby ultra-luminous infrared galaxy F01004-2237, Nature Astronomy, 1, 0061

Tampo Y., et al., 2020, Rapidly Evolving Transients from the Hyper Suprime-Cam SSP Transient Survey, ApJ, 894, 27

Tanikawa A., 2018a, Tidal double detonation: a new mechanism for the thermonuclear explosion of a white dwarf induced by a tidal disruption event, MNRAS, 475, L67

Tanikawa A., 2018b, High-resolution Hydrodynamic Simulation of Tidal Detonation of a Helium White Dwarf by an Intermediate Mass Black Hole, ApJ, 858, 26

Tanikawa A., Yoshikawa K., Okamoto T., Nitadori K., 2012, N-body simulation for self-gravitating collisional systems with a new SIMD instruction set extension to the x86 architecture, Advanced Vector eXtensions, New Astron., 17, 82

Tanikawa A., Yoshikawa K., Nitadori K., Okamoto T., 2013, Phantom-GRAPE: Numerical software library to accelerate collisionless N-body simulation with SIMD instruction set on x86 architecture, New Astron., 19, 74

Tanikawa A., Nakasato N., Sato Y., Nomoto K., Maeda K., Hachisu I., 2015, Hydrodynamical Evolution of Merging Carbon-Oxygen White Dwarfs: Their Pre-supernova Structure and Observational Counterparts, ApJ, 807, 40

Tanikawa A., Sato Y., Nomoto K., Maeda K., Nakasato N., Hachisu I., 2017, Does Explosive Nuclear Burning Occur in Tidal Disruption Events of White Dwarfs by Intermediate-mass Black Holes?, ApJ, 839, 81

Taubenberger S., 2017, The Extremes of Thermonuclear Supernovae. p. 317, doi:10.1007/978-3-319-21846-5_37

Tchekhovskoy A., Metzger B. D., Giannios D., Kelley L. Z., 2014, Swift J1644+57 gone MAD: the case for dynamically important magnetic flux threading the black hole in a jetted tidal disruption event, MNRAS, 437, 2744

Tejeda E., Rosswog S., 2013, An accurate Newtonian description of particle motion around a Schwarzschild black hole, MNRAS, 433, 1930

Timmes F. X., 1999, Integration of Nuclear Reaction Networks for Stellar Hydrodynamics, ApJS, 124, 241

Timmes F. X., Swesty F. D., 2000, The Accuracy, Consistency, and Speed of an Electron-Positron Equation of State Based on Table Interpolation of the Helmholtz Free Energy, ApJS, 126, 501

Timmes F. X., Hoffman R. D., Woosley S. E., 2000, An Inexpensive Nuclear Energy Generation Network for Stellar Hydrodynamics, ApJS, 129, 377

Toscani M., Rossi E. M., Lodato G., 2020, The gravitational wave background signal from tidal disruption events, MNRAS, 498, 507

Tully R. B., Courtois H. M., Sorce J. G., 2016, Cosmicflows-3, AJ, 152, 50

Valenti S., et al., 2014, PESSTO monitoring of SN 2012hn: further heterogeneity among faint Type I supernovae, MNRAS, 437, 1519

Veigele W. J., 1973, Photon Cross Sections from 0.1 KeV to 1 MeV for Elements Z = 1 to Z = 94, Atomic Data, 5, 51

Verner D. A., Yakovlev D. G., 1995, Analytic FITS for partial photoionization cross sections., A&AS, 109, 125

Verner D. A., Ferland G. J., Korista K. T., Yakovlev D. G., 1996, Atomic Data for Astrophysics. II. New Analytic FITS for Photoionization Cross Sections of Atoms and Ions, ApJ, 465, 487

Wang J., Merritt D., 2004, Revised Rates of Stellar Disruption in Galactic Nuclei, ApJ, 600, 149

Wang T., Yan L., Dou L., Jiang N., Sheng Z., Yang C., 2018, Long-term decline of the mid-infrared emission of normal galaxies: dust echo of tidal disruption flare?, MNRAS, 477, 2943

Wendland H., 1995, Piecewise polynomial, positive definite and compactly supported radial functions of minimal degree, Advances in computational Mathematics, 4, 389

Wilson J. R., Mathews G. J., 2004, White Dwarfs near Black Holes: A New Paradigm for Type I Supernovae, ApJ, 610, 368

Winter W., Lunardini C., 2020, A concordance scenario for the observation of a neutrino from the Tidal Disruption Event AT2019dsg, arXiv e-prints, p. arXiv:2005.06097

Woosley S. E., Hoffman R. D., 1992, The alpha -Process and the r-Process, ApJ, 395, 202

Woosley S. E., Weaver T. A., 1995, The Evolution and Explosion of Massive Stars. II. Explosive Hydrodynamics and Nucleosynthesis, ApJS, 101, 181

Yalinewich A., Steinberg E., Piran T., Krolik J. H., 2019, Radio emission from the unbound debris of tidal disruption events, MNRAS, 487, 4083

Yamanaka M., et al., 2015, OISTER Optical and Near-Infrared Observations of Type Iax Supernova 2012Z, ApJ, 806, 191

Yang Q., Shen Y., Liu X., Wu X.-B., Jiang L., Shangguan J., Graham M. J., Yao S., 2019, An Unusual Mid-infrared Flare in a Type 2 AGN: An Obscured Turning-on AGN or Tidal Disruption Event?, ApJ, 885, 110

Zauderer B. A., et al., 2011, Birth of a relativistic outflow in the unusual γ-ray transient Swift J164449.3+573451, Nature, 476, 425

Zhang B. T., Murase K., Oikonomou F., Li Z., 2017, High-energy cosmic ray nuclei from tidal disruption events: Origin, survival, and implications, Phys. Rev. D, 96, 063007

van Velzen S., 2018, On the Mass and Luminosity Functions of Tidal Disruption Flares: Rate Suppression due to Black Hole Event Horizons, ApJ, 852, 72

van Velzen S., et al., 2016a, A radio jet from the optical and x-ray bright stellar tidal disruption flare ASASSN-14li, Science, 351, 62

van Velzen S., Mendez A. J., Krolik J. H., Gorjian V., 2016b, Discovery of Transient Infrared Emission from Dust Heated by Stellar Tidal Disruption Flares, ApJ, 829, 19

van Velzen S., et al., 2020a, Seventeen Tidal Disruption Events from the First Half of ZTF Survey Observations: Entering a New Era of Population Studies, arXiv e-prints, p. arXiv:2001.01409

van Velzen S., Holoien T. W. S., Onori F., Hung T., Arcavi I., 2020b, Optical-Ultraviolet Tidal Disruption Events, Space Sci. Rev., 216, 124